

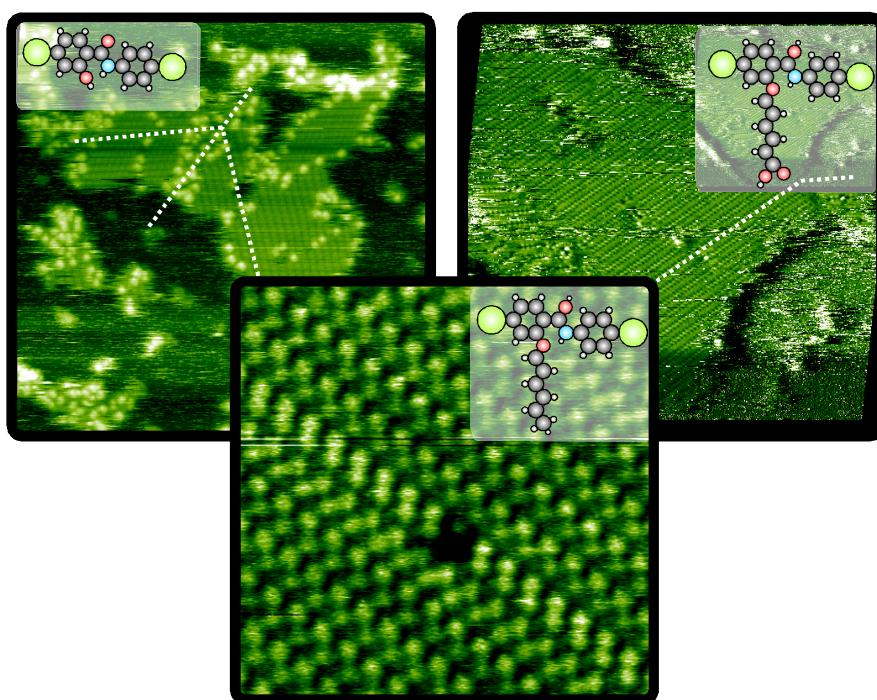
Systematic Functionalization of Molecules for Molecular Self-Assembly

Dissertation
zur Erlangung des Grades
“Doktor der Naturwissenschaften”
im Promotionsfach Physikalische Chemie

am Fachbereich Chemie, Pharmazie und Geowissenschaften
der Johannes Gutenberg-Universität Mainz

Christopher Moritz Hauke

geboren in Mainz



Mainz, den 02. Mai 2013

This dissertation was supervised by [REDACTED]
and was carried out at the Johannes Gutenberg-Universität Mainz
from April 2010 to April 2013.

D77 (dissertation Johannes Gutenberg-Universität Mainz)

Dean of the faculty	[REDACTED]
1st report	[REDACTED] Johannes Gutenberg-Universität Mainz
2nd report	[REDACTED] Max Planck Institute for Polymer Research Mainz
Submitted:	02.05.2013
Oral examination:	03.06.2013

Für meine Familie

Contents

1	Introduction	1
2	Molecular Self-Assembly on Insulators	5
3	Introduction to AFM	13
3.1	Scanning Probe Techniques	14
3.2	Forces in AFM	15
3.3	AFM Operating Modes	22
3.4	Deflection Detection Methods	30
3.5	Feedback Loops in NC-AFM	34
4	Setup of the UHV AFM System	37
4.1	UHV System	38
4.2	Scanhead	39
4.3	Sensor and Sample Preparation	41
4.4	Data Processing and Analysis	45
5	The Bulk Insulator Calcite	47
6	Shape-Persistent Oligo(<i>p</i>-benzamide)s	51
6.1	Introduction	52
6.2	OIB	56
6.3	OIB <i>al</i>	61
6.4	OIB <i>ca</i>	64
6.5	Further Iodobenzene Systems	67
6.6	Conclusions	71
7	Terephthalic Acids	73
7.1	Introduction	74
7.2	2-ATPA	76
7.3	2-BrTPA	83
7.4	2-Br-5-PATPA	88
7.5	Conclusions	92

8	Heptahelicene-2-carboxylic Acid	93
8.1	Introduction	94
8.2	Morphology at Room Temperature	96
8.3	Elevated Temperatures	101
8.4	Conclusions	102
9	Summary	105
	Bibliography	109
	Acknowledgements	129
	Publications and Presentations	131
	Curriculum vitae	135

1 Introduction

Science is organized knowledge.

Herbert Spencer
(1820-1903)

MATERIALS science as an interdisciplinary field of research has always dealt with the creation of new structures and materials, combining methods from chemistry and physics as well as biology. Not only are the applied methods manifold, but so are the created systems that cover several orders of magnitude, ranging from macroscopic creations such as alloys and compound materials to microscopic structures and beyond. Especially the increasing miniaturization has attracted great attention in recent years, *e.g.* in the field of electronics, where the ultimate goal of this miniaturization would be integrated circuits that are based on single atoms and molecules, with circuit paths being no wider than a few nanometers. This, of course, raises the question of how to make these (sub)-nanometer structures accessible for manufacture.

Approaches to produce structures in the sub-100 nm regime nowadays include techniques such as electron beam and X-ray lithography¹ or even the manipulation and arrangement of single atoms using scanning probe techniques.² They can be classified into two kinds of processes, namely *top-down* and *bottom-up* approaches. In the bottom-up approach, single building blocks are used as starting point to create the desired structures, similar to an engineer that assembles different machine parts into a working engine. Top-down processes, in contrast, start from an already existing bigger object and work their way down to the desired structure. The aforementioned lithographic methods are

classical examples for a top-down approach, while the atom-by-atom arrangement is a typical bottom-up process.

While an impressive degree of structural control, even over single atoms, can be achieved in that way, another important aspect has to be considered as well. The construction of application-relevant structures renders *serial* techniques that only address single atoms and molecules useless in terms of efficiency for mass production. Instead, a *parallel* approach is needed, such as *molecular self-assembly*, where conformational instructions are conveyed to the ensemble of molecules that are intended as building blocks as a whole. These instructions can be encoded in the structure of the molecules themselves, be imposed on the molecules via carefully chosen and prepared substrates or be induced by changing environmental parameters such as temperature or pressure. The challenge herein lies in drafting these conformational instructions precisely enough to achieve the desired results in an efficient way, but at the same time maintaining enough flexibility for these instructions to be applicable to a large ensemble of building blocks.

In this thesis, molecular self-assembly will be used as a parallel bottom-up approach for the creation of molecular structures on an insulating substrate, namely the calcite(10.4) surface. While great progress has been made in the field of self-assembled structures on metallic surfaces in recent years,³ working on insulating substrates remains challenging due to the much lower surface and interaction energies. The use of insulating substrates, however, is compulsory for the creation of molecular electronic devices, as circuits and substrate have to be electronically decoupled. In chapter 2, I will illustrate the concept of molecular self-assembly and give an overview over the challenges that arise from anchoring organic molecules to insulating surfaces.

The technique used here to investigate the self-assembled structures is non-contact atomic force microscopy operated under ultrahigh vacuum conditions. Using this technique, it is possible to image insulating substrates and self-assembled structures with atomic precision. In chapters 3 and 4 I will elaborate on the principles of atomic force microscopy and introduce the setup used in this thesis.

Chapter 5 will deal with the properties of the bulk insulator calcite. The focus will lie on the description of the calcite (10.4) cleavage plane upon which the experiments in this thesis were conducted.

In chapters 6-8, I will present my results on the systematic functionalization of organic molecules and the influence of these variations on the self-assembled structures. Chapter 6 will describe the investigation of molecules from the class of shape-persistent oligo(*p*-benzamide)s whose molecular core is specifically designed for electrostatic anchoring to the substrate surface. I will, amongst others, demonstrate how the addition of single moieties, such as an alkyl chain, decisively alters the molecular adsorption geometry while the basic adsorption mechanism stays the same for all molecules.

I will then continue with the investigation of the self-assembly of different derivatives of terephthalic acid in chapter 7. Here, in contrast to the previous chapter, the adhesion to the surface is altered by introducing different functional groups that serve as anchor functionalities, thus influencing the stability of the molecular structures on the surface. Similar as for unfunctionalized terephthalic acid, a strong substrate templating effect on the structure formation is expected.

Chapter 8 will describe how an intrinsic molecular property, namely the molecule's chirality, influences the self-assembly process. I will, for that purpose, compare the results of a racemic mixture of heptahelicene-2-carboxylic acid with those of the enantiopure molecules and show, that distinctively different structures arise from chiral recognition.

The results of this thesis, thus, constitute an important step towards controlling the formation of self-assembled structures on insulating surfaces. It is demonstrated how the molecule-surface and molecule-molecule interactions are influenced by providing molecules with different moieties and anchor functionalities and how the interplay of these two interactions affects the self-assembly process. My results can, therefore, act as a guideline for the rational design of molecules for use in self-assembly processes.

2 Molecular Self-Assembly on Insulators

Contents

Choice of Substrate	6
Rational Molecule Design	9

MOLECULAR self-assembly, as a bottom-up process, describes the autonomous ordering of molecular building blocks into organized structures. It represents a powerful route for creating functional molecular structures in a spontaneous and parallel fashion, *i.e.*, without the need of manipulating individual molecules,⁴ giving it decisive advantage over serial processes such as atom-by-atom arrangement using scanning probe techniques.

Confusion is often caused by the various loose definitions that exist for the term self-assembly. In this thesis, I will follow the commonly used definition given by Whitesides and Grzybowski:⁵

"Here, we limit the term to processes that involve pre-existing components [. . .], are reversible, and can be controlled by proper design of the components."

The condition of pre-existing compounds is certainly fulfilled for the deposition of molecules on a substrate surface. In order to be reversible, the self-assembly process has to lead to a thermodynamic equilibrium state. The term of self-assembly should,

therefore, not be applied to, *e.g.*, diffusion-limited structures that are kinetically trapped in a non-equilibrium state.

Molecular self-assembly on surfaces is controlled by the delicate balance between intermolecular and molecule-surface interactions. The combination of molecules and substrate, therefore, is of crucial importance and proper design of these components provides a highly effective key for tuning the structure formation.

Choice of Substrate

In the last decades, an impressive range of structures has been created using molecular self-assembly,⁶ including, *e.g.*, perfect two-dimensional overlayers,⁷ uni-directional rows,^{8–10} clusters^{9,11} and porous networks.^{12,13} Three examples for the richness of the created structures are shown in Fig. 2.1. These studies have, however, been limited to metallic substrates as many classical surface-sensitive tools such as scanning tunneling microscopy or photoelectron spectroscopy are limited to conducting substrates.

Yet, for the creation of application-relevant devices, these concepts have to be extended to insulating substrates. While high-resolution imaging can be achieved using atomic force microscopy (Chap. 3), dielectric substrates pose another, more fundamental challenge for molecular self-assembly. Most dielectric surfaces studied so far exhibit only very weak and unspecific binding towards the molecular building blocks. On metal surfaces, the strong binding of molecules is mainly determined by the overlap and energetic separation of molecular and surface orbitals.^{14,15} In contrast to metal surfaces, insulating substrates exhibit a fairly large band gap, largely restraining this possibility and, therefore, leading to overall weaker interactions. This weak interaction severely hampers the formation of self-assembled structures on prototypical insulating surfaces held at room temperature. Instead, high molecular mobility,¹⁶ clustering at step edges¹⁷ and molecular bulk crystal formation¹⁸ has been observed frequently.

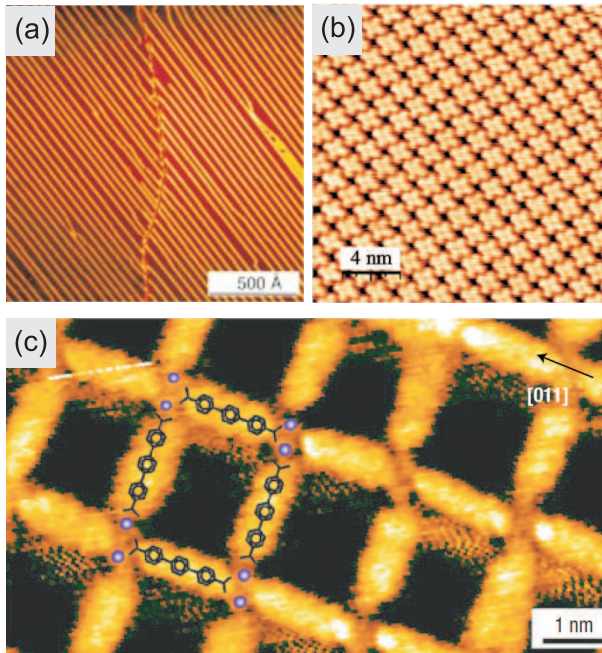


Figure 2.1: Examples for molecular self-assembly on metals. (a) Unidirectional rows of PVBA on Ag(111), demonstrating long-range ordering (reproduced from¹⁰). (b) Two-dimensional overlayer of ZnPcF₈ on Ag(111). Each star-shaped structure represents a single molecule (reproduced from⁷). (c) TPA-Fe coordination network on Cu(100) (reproduced from¹³).

In thermodynamic equilibrium, the wetting properties of molecules deposited onto a surface can be classified into three growth modes:¹⁹

- Frank-van-der-Merve (layer-by-layer growth),
- Stranski-Krastanov (layer-plus-bulk growth) and
- Volmer-Weber (bulk growth).

The observation of bulk growth indicates, that no or only weak interaction between molecules and sample surface exists. The surface, thus, does not influence the self-assembly process. How-

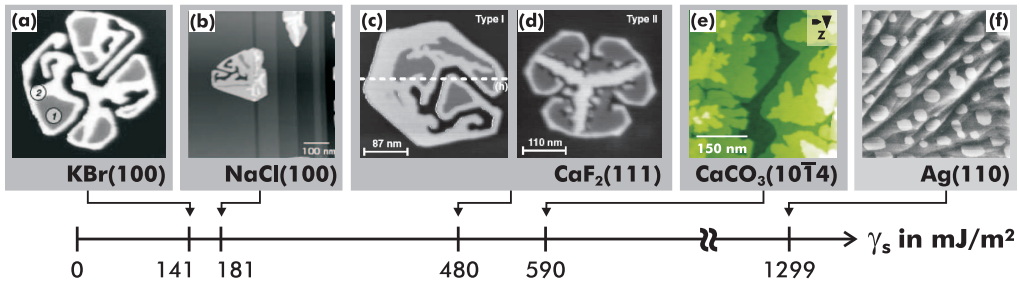


Figure 2.2: Wetting properties of C_{60} molecules on different surfaces as a function of surface energy γ_s . Only for $CaCO_3$ and $Ag(110)$, stable wetting layers are observed (reproduced from²⁵).

ever, this influence of the surface on the self-assembly process is highly desirable in order to access the structural richness that is provided by the *templating effect* of the underlying substrate.²⁰ Therefore, layer-by-layer growth is the favored growth mode for molecular self-assembly. The templating effect relies on guiding the self-assembly process by locally influencing the molecular adsorption geometry. This is achieved by either taking advantage of natural patterning such as defects or surface reconstructions, or by artificially inducing a surface patterning, *e.g.* by electron beam irradiation.²¹ The choice of substrate and its preparation, therefore, is the first important parameter to ensure structural diversity of the self-assembled systems.

All mentioned growth modes can be related by considering the *surface energy* γ of sample and molecules.¹⁹ Following this model, it can be shown that the likelihood of layer-by-layer growth increases for substrates with high surface energies. This readily explains why stable wetting layers are easily obtained on metallic surfaces, where surface energies are in the range of several 1000 mJ m^{-2} , while prototypical insulating surfaces feature surface energies that are about one order of magnitude lower than that.^{22–24} As an example, Fig. 2.2 shows how the wetting properties of C_{60} molecules change on substrates with differing surface energies. A substrate appropriate for molecular self-assembly should, thus, exhibit a large surface energy. While the relation between substrate surface energy γ_s and growth modes has been known for quite some time,¹⁹ it is intriguing to see how this simple macroscopic parameter can be used to classify the eligibility of substrates for use in molecular self-assembly.²⁵

Rational Molecule Design

The second big step is choosing molecules that are appropriate for a particular substrate. The interaction mechanisms for molecules with insulating surfaces are manifold, ranging from weak van-der-Waals interactions²⁶ and hydrogen bond formation²⁷ to electrostatic interactions in the case of ionic crystals. In terms of energies, the binding energy to the surface E_b has to be stronger than the thermal energy E_{th} of the molecules. Otherwise, they would desorb from the surface. On the other hand, self-assembly requires the molecules to be mobile enough to assemble into a thermodynamically stable state. Thus, their thermal energy has to be larger than the diffusion barrier E_d .

Apart from the molecule surface interaction, the intermolecular interaction, characterized by the energy E_{inter} , has to be considered as well. Here, additional interactions arise from mechanism such as $\pi - \pi$ -interaction between aromatic systems. It is important to note that the strength of E_{inter} cannot be arbitrarily high. If, *e.g.*, strong covalent bonds between the molecular building blocks are already formed upon deposition, making E_{inter} larger than E_{th} , self-assembly is not possible any more as the strong bonds immobilize the molecules and, thus, conflict with the condition of reversibility.

In order to enhance the stability of the self-assembled structures it may, however, be desired to create these strong covalent bonds once the system has settled into a thermodynamic minimum and the process of self-assembly itself is completed. This *on-surface chemistry* has just recently been impressively demonstrated by Kittelmann *et al.*, who, for the first time, presented the covalent linking of organic molecules on an insulating substrate.²⁸

Combining the energetic considerations made above leads to a simple condition for the success of molecular self-assembly processes:³

$$E_b > E_{inter} \geq E_{th} \geq E_d \quad (2.1)$$

While the thermal energy of the molecules can easily be influenced by changing the temperature of the system, E_{inter} and

E_b depend on the molecular structure itself. They can, thus, be accessed and tuned by a *rational design* of the molecular building blocks. As described above, anchoring the molecules to the surfaces, *i.e.* increasing E_b usually is the major challenge when working on insulating substrates. Secondly, the molecules should be able to interact with the surface in order to make use of the aforementioned templating effect. If this interaction is too weak, the substrate will not noticeably influence the self-assembly process.²⁹ Therefore, it is highly desirable to design molecules with specific anchor groups that provide a linker towards the surface.

Organic molecules offer a highly flexible chemistry, making them ideal candidates for that purpose. Besides an abundance of already existing molecules, the field of organic chemistry provides the possibility to specifically design new molecules for use in self-assembly processes. These molecular cores can, in turn, easily be equipped with different functional groups that change the intermolecular interaction or serve as an anchor functionality.

Several attempts have been made in this direction, most of them based on the *electrostatic anchoring* of molecules bearing a high dipole moment with an ionic crystal surface.^{16,21,30–34} Two examples of this electrostatic anchoring are shown in Fig. 2.3.

Apart from electrostatic interactions, other anchoring mechanisms can be exploited as well. This will, amongst others, be demonstrated later on in this thesis. One example is the formation of hydrogen bonds between molecules and sample. For molecules functionalized with, *e.g.*, a carboxylic acid end group, theoretical studies predict hydrogen bonding of the OH groups to the calcium ions of the calcite (10.4) surface.²⁷ This predicted binding behavior agrees well with the experimentally determined binding of several -COOH functionalized molecules on this surface.^{28,35}

Other approaches include matching the dimensions of molecular building block and substrate in order to enhance the substrate templating effect or changing the number and/or positions of the functional groups.³⁶

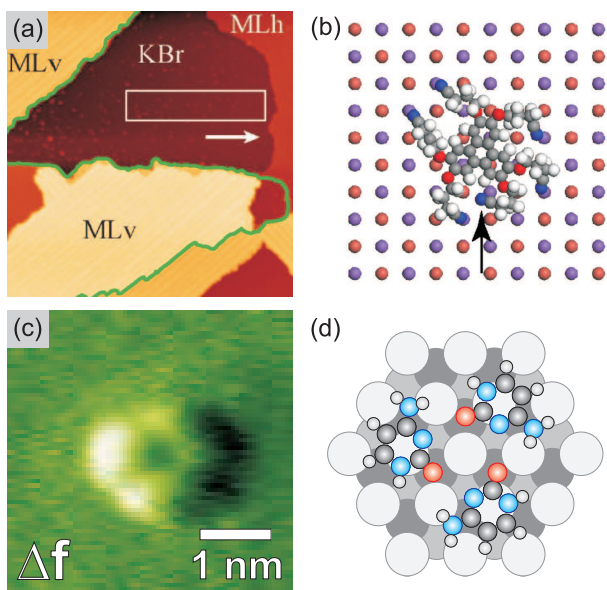


Figure 2.3: Different methods for anchoring organic molecules to insulating surfaces. (a,b) Triphenylene derivative bound to KBr (001) by electrostatic interaction. The CN-groups are binding to the K^+ ions as shown in the adsorption model (reproduced from³⁴). (c,d) Cytosine on CaF_2 (111). The formation of trimers (see model) in combination with the large molecular dipole moment stabilizes the molecules on the surface (reproduced from³³).

Molecular interactions are, of course, not determined by the functional groups alone. Apart from mechanism like the aforementioned $\pi - \pi$ -stacking between aromatic systems, molecular chirality can play a decisive role in the adsorption geometry.³⁷⁻⁴¹ Additionally, molecules that are achiral in the gas phase can become chiral when confined to two dimensions, *e.g.* upon adsorption to a surface (*prochirality*).^{33,42} The influence of chirality on structure formation will also be discussed in this thesis.

However, when designing specific molecules and anchor groups, an important aspect needs to be considered. While strong binding towards the surface is desired for creating a stable wetting layer, the subtle balance between intermolecular and molecule-surface interactions is mandatory for maintaining structural flex-

ibility. This fact can create conflicting interests as a strong binding and a well-defined adsorption position is usually incompatible with fine-tuning the molecular arrangement via the intermolecular interactions.

To grasp the full potential of molecular self-assembly, therefore, requires strategies for anchoring the molecular building blocks towards the surface in a way that maintains flexibility in terms of intermolecular interaction and relative molecule orientation. This will, amongst others, be demonstrated in this thesis by comparing the adhesion and cohesion properties of different, rationally designed molecules.

3 Introduction to AFM

Contents

3.1 Scanning Probe Techniques	14
3.2 Forces in AFM	15
Long-Range Forces	17
Short-Range Forces	18
Contrast Formation in AFM	20
3.3 AFM Operating Modes	22
Static Force Microscopy	22
Dynamic Force Microscopy	24
3.4 Deflection Detection Methods	30
Laser Beam Deflection	30
Self-Sensing Devices	32
3.5 Feedback Loops in NC-AFM	34

ALL investigations described in this thesis were performed using non-contact atomic force microscopy (NC-AFM) under ultra-high vacuum conditions. In this chapter, I will, therefore, first give an introduction into the basic aspects of atomic force microscopy, including a short overview of related scanning probe techniques. The focus will lie on describing the forces relevant in AFM as well as different AFM operating modes.

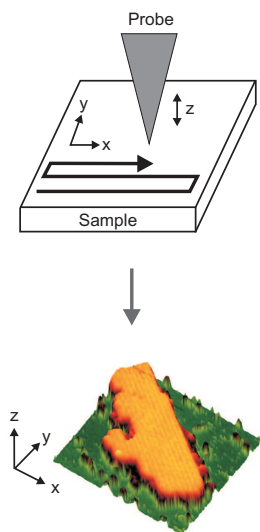


Figure 3.1: Principle of scanning probe measurements. Information is recorded at every point of the grid and can finally be displayed as a three-dimensional image.

3.1 Scanning Probe Techniques

The atomic force microscope (AFM) has been introduced by Binnig *et al.* in 1986,⁴³ following up the invention of the scanning tunneling microscope (STM) in 1982.⁴⁴ In STM, a tunneling current between a metallic tip and a conducting sample is measured, probing the electronic surface states of the sample. AFM, in contrast, is sensitive to the intermolecular forces, being able to resolve forces in the order of 10^{-12} N.⁴⁵ Both methods belong to the class of the so-called scanning probe techniques. Here, a physical probe is scanned in a defined way over the sample in question and the interaction between probe and sample is recorded as a function of the spatial coordinates. This information can then be displayed in the form of an image giving the interaction strength at each point of the grid.

All scanning probe techniques have in common that they result in **real-space information** about the desired sample as opposed to scattering or diffraction techniques which access the reciprocal space. Being able to visualize the atomic corrugation of a surface in real space for the very first time, the STM laid the foundation for the development of modern SPM methods and its inventors were awarded the Nobel prize only four years after the first report of their discovery.

The decision, which technique to use, depends heavily on the properties of the sample and the questions that are to be addressed. The focus of this thesis lies on researching the interaction of large organic molecules with insulating surfaces for their use in future organic molecular electronics. This requires high-resolution, real-space information about the sample surface as well as the morphology of the deposited molecular structures. In surface science, among the most common techniques to achieve this are the STM and the AFM. As STM measurements are restricted to conducting surfaces, the AFM, which is capable of imaging insulating samples with highest precision, is the technique of choice.

In the following sections, I will therefore first discuss the relevant forces acting on an AFM probe, usually a sharp tip at the

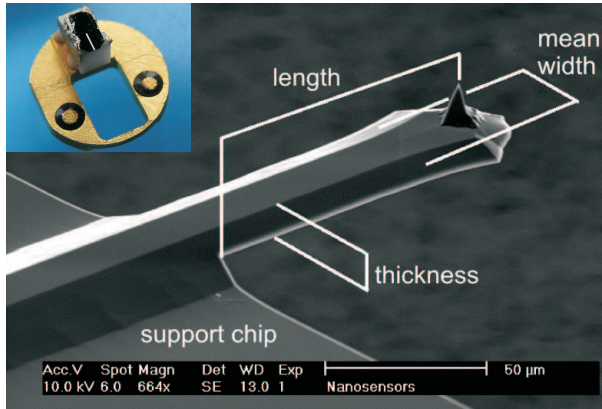


Figure 3.2: Scanning electron microscopy (SEM) image of a silicon cantilever as typically used in AFM measurements. The inset shows the cantilever support chip mounted on a sample holder for use in an Omicron VT AFM. Images are reproduced from Ref. ⁴⁶ courtesy of [REDACTED]

end of a cantilever as depicted in Fig. 3.2, followed by a discussion of different AFM operating modes including their individual advantages and drawbacks. Special attention will be given to the question of contrast formation in AFM which is crucial for the correct interpretation of the measurement data.

The discussion of different deflection detection methods and the role of feedback loops in AFM operation will conclude this chapter.

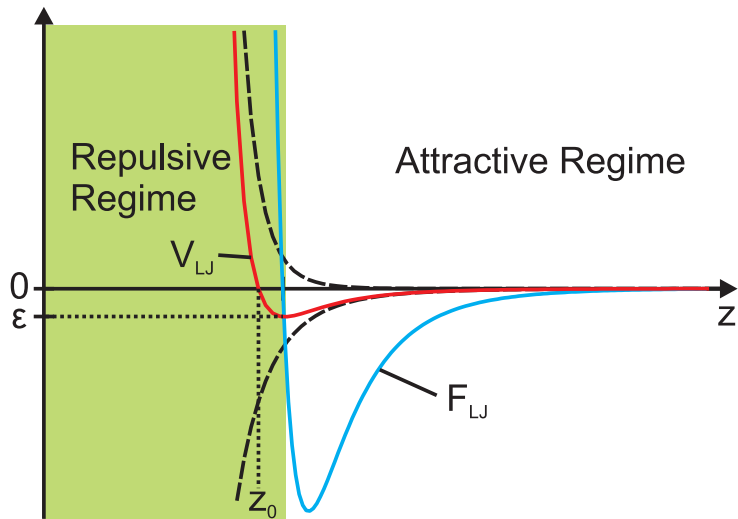
3.2 Forces in AFM

Under ultra-high vacuum conditions, the force acting on an AFM probe can in a first approximation be described using the semi-empirical Lennard-Jones potential,⁴⁷ a special case of the more general Mie potential,⁴⁸ given by

$$V_{LJ}(z) = 4\epsilon \left[\left(\frac{z_0}{z} \right)^{12} - \left(\frac{z_0}{z} \right)^6 \right] \quad (3.1)$$

with the potential depth ϵ and zero-crossing at $z = z_0$.

Figure 3.3: Lennard-Jones potential and corresponding force as function of tip-sample distance z . The dashed lines give the repulsive and attractive parts of the potential.



It is intuitively clear that the forces described by this potential have to be dependent on the distance z between probe and sample. It is hence sensible to differentiate between *long-range forces* and *short-range forces*. When approaching the sample, the tip will first sense the attractive long-ranged force contributions, which are given by the z^{-6} part in the potential. Getting closer to the sample surface, the contribution of the short-ranged repulsive interactions will increase proportional to z^{-12} until reaching the equilibrium distance z_0 from where on the repulsive interactions dominate. The most important long- and short-range forces relevant to AFM will be discussed in the following section.

While the Lennard-Jones potential describes the qualitative force behavior very well, it is strictly speaking only applicable for the interaction between two single uncharged atoms. Influences from factors like tip geometry or environmental effects are neglected in this model. Therefore, more complicated models have to be applied for quantitative statements. This is of importance if not only structural information, but absolute force values are of interest.^{49,50} A prominent example for an empirical potential is the Stillinger-Weber potential, which describes the interaction of a Si-tip with a Si-surface.⁵¹

Long-Range Forces

Main contributions to the long-range forces are usually *van-der-Waals* and *electrostatic* interactions. These long-range forces do not contribute to the atomic contrast as they are mainly resulting from interactions between macroscopic parts of the tip and the sample. It is for that reason desirable to compensate them as good as possible, for example by applying a bias voltage in the case of electrostatic forces.

Electrostatic Forces

Electrostatic interactions arise from potential differences between probe and sample and can be described by the Coulomb potential. In the simple case of two point charges that are placed at distance z in ultra-high vacuum (UHV), calculation of the the interaction force yields

$$F_C(z) = \frac{1}{4\pi\epsilon_0} \frac{q_1 \cdot q_2}{z^2} \quad (3.2)$$

with q_i being the respective charge value. Under UHV conditions, insulating substrates tend to accumulate charges as these cannot be dissipated in the sample itself. This charge accumulation usually takes place after cleaving a fresh sample and in turn leads to additional coulombic interaction between tip and sample.

This electrostatic interaction can also be expressed in terms of the potential difference U between tip and sample:

$$F_{El}(z) = -\frac{1}{2} \frac{dC(z)}{dz} U^2 \quad (3.3)$$

where C is the capacitance of the tip-sample system as depicted in Fig. 3.4. In order to account for the effect of charge accumulation, the electrostatic interaction can be compensated by applying a counter voltage U_{gap} between tip and sample. If the information about the needed counter voltage is recorded at every imaging point, a map of the local contact potential difference

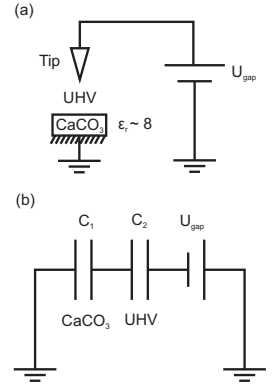


Figure 3.4: (a) Simple scheme for description of the electrostatic interaction between tip and a calcite sample. (b) Equivalent circuit diagram. C_1 and C_2 combined give the capacitance in Eqn. 3.3.

is obtained. This is used in the technique of Kelvin probe force microscopy (KPFM).⁵²

Van-der-Waals Forces

Van-der-Waals (vdW) interactions are long-range forces that arise from the interaction between permanent or induced dipoles. They are usually separated into three different contributions.

Forces acting between two permanent dipoles are described by the **Keesom interaction**.⁵³

Debye interactions describe how a permanent dipole induces a temporary dipole in a neighboring polarizable molecule.⁵⁴

The **London dispersion force** finally describes a quantum-mechanical phenomenon where spatial fluctuations in electron cloud induce temporary dipoles that are interacting with each other.⁵⁵

For the latter two interactions, the polarizability of the neighboring molecules plays a significant role in determining the interaction strength. VdW-forces have interaction ranges of up to 100 nm⁵⁶ and thus effect large parts of the tip. For macroscopic objects, these forces are also highly dependent on the objects shape and have to be calculated by integrating over the whole body. As a simple AFM model, the vdW interaction between a sphere of radius r and an infinite plane at distance z can be expressed as⁵⁷

$$F_{\text{vdW}}(z) = -\frac{A_H r}{6z^2} \quad (3.4)$$

using the Hamaker-constant A_H to describe the material properties. Unlike electrostatic forces, vdW-interactions cannot be compensated during measurements and have to be considered a constant offset to the measurement signal. They can only be minimized by using cantilevers with sharp tips.

Short-Range Forces

The short-range chemical forces include contributions such as chemical bonds or Pauli repulsion. Their range is typically in the

order of 100 - 200 pm,⁵⁷ so that they will ideally only be sensed by the tip apex atom. At the same time, these short-range interactions make it possible to discriminate the contribution of single sample atoms to the force acting on the tip. They are, therefore, responsible for the formation of the desired atomic contrast. The two most important contributions will shortly be discussed now.

Pauli Repulsion

Known from atomic physics, the Pauli exclusion principle states that two fermions, occupying the same physical space, cannot share an identical set of quantum numbers. For AFM measurements, this is relevant as soon as cantilever and sample are close enough to each other for their respective orbitals to overlap. Electrons occupying the same orbital can only differ in one quantum number, namely their spin state. An overlap of two fully occupied orbitals will thus result in a repulsive interaction as electrons are forced to move into higher energetic states. This repulsion effect is therefore also called Pauli exclusion force.

Chemical Bonds

If, on the other hand, the overlapping orbitals of tip and sample are not fully occupied, covalent bonds can be formed. These bonds are of course very short-lived as they are immediately broken again due to the scanning movement. Overall, this will result in a net attractive interaction, whose strength mainly depends on the distance and occupation state of the involved orbitals.

The forces described before are the main contributions when using AFM under UHV-conditions. When working under ambient conditions additional forces, such as capillary and meniscus forces, have to be considered as well.

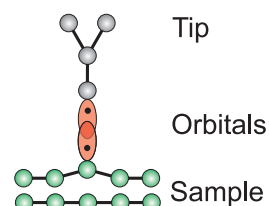


Figure 3.5: Orbital overlap for tip and sample. Depending on the occupation of the orbitals, Pauli repulsion or chemical bonding occurs.

Contrast Formation in AFM

The interplay of all forces acting on a cantilever tip can result in a rather complex contrast formation in the acquired AFM data, making a detailed interpretation of these images not always straightforward. The contrast formation is further influenced by factors that arise from the technical setup itself, as will be described now.

AFM images, as well as images obtained with other scanning probe methods, are always tip-sample convolutions. Surface features might, therefore, be imaged distortedly as shown in Fig. 3.6. Depending on the opening angle of the tip, either the shape of the surface feature or that of the tip is recorded in the topography channel. The image contrast, therefore, greatly depends on the microscopic geometry of the tip, especially its aspect ratio.

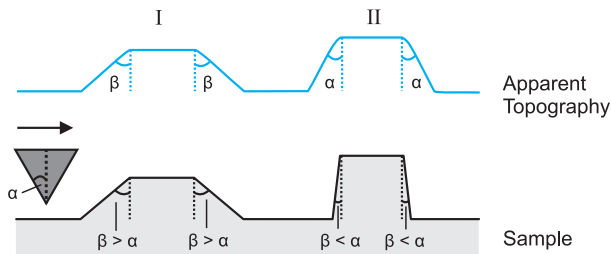


Figure 3.6: Principle of tip-sample convolution. The tip has an opening angle of 2α while the surface features have an angle β with respect to the surface normal. In I, the feature is imaged correctly, in II the tip shape is imaged. The arrow gives the scan direction.

In reality, AFM tips are usually not symmetric as in the simple model shown here, but exhibit asymmetries that influence the contrast formation. Surface features might, therefore, be displayed with additional kinks or steps as shown in Fig. 3.7. A related effect is the so-called multiple tip: If the tip apex consists not only of a single atom, but of several atoms at similar height, sample structures might misleadingly be duplicated in the resulting image.

It is, however, important to note that the topography signal that is recorded by an asymmetric tip does not depend on the scan

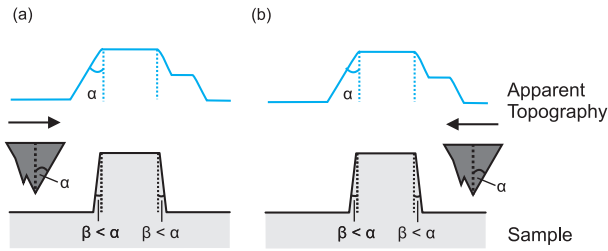


Figure 3.7: Effect of an asymmetric tip on contrast formation. Additional features such as kinks are displayed independent of the scan direction.

direction. Images acquired in, *e.g.*, forward and backward moving scans will display the same topography as the tip itself is not turned when changing the scan direction.

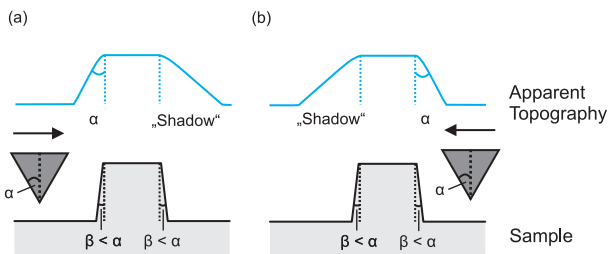


Figure 3.8: Effect of finite feedback loop response time on contrast formation. The position of the shadow depends on the scan direction.

Feedback loops that are used to control the tip movement only operate with a finite response time, leading to "shadow" structures in the resulting image (Fig. 3.8). The magnitude of this shadow effect depends on the feedback loop settings as well as the height of the imaged surface feature. In contrast to effects induced by an asymmetric tip, the orientation of these shadows depends on the scan direction.

The analysis of AFM data is further complicated by imaging effects like contrast inversion, that can be observed depending on the chosen imaging parameters. As an example, this effect can be reproducibly achieved when imaging C_{60} layers with AFM.⁵⁸

Modeling different tip geometries and imaging conditions has

also become an important branch of research among theorists, who investigate the effects those parameters have on contrast formation in AFM (see e.g. Pérez *et al.*⁵⁹).

3.3 AFM Operating Modes

The probe used in AFM usually is a micro-machined cantilever with an atomically sharp tip at its end. Interaction between this tip and the sample leads to bending of the cantilever which is measured and used to calculate the interaction strength.

Two basic operating modes exist for AFM, namely static and dynamic force microscopy, both of which will be described in the following sections.

Static Force Microscopy

The static force or contact mode AFM is one of the most commonly used and simplest modes. Here, the cantilever is brought in direct contact with the sample and scanned over the surface, similar to the movement of a needle in a record player. The forces acting between the tip and the sample then cause the cantilever to bend. This bending or *deflection* is usually very small compared to the dimensions of the cantilever. It can, in that case, be described using Hooke's law

$$F_{ts} = -k \cdot q, \quad (3.5)$$

where F_{ts} is the force acting between tip and sample, k the cantilever's stiffness and q its deflection in regard to the unperturbed state. For a sample with homogeneous surface properties, this scanning results in an image displaying the sample topography. Measurements in the contact mode are usually taking place in the repulsive force regime. It is obvious that in this imaging mode soft cantilevers with a small k are preferred in order to be sensitive to small forces.

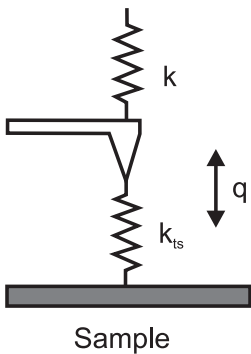


Figure 3.9: One-dimensional model for the coupling of cantilever and tip-sample interaction.

Though being simple in implementation, this AFM mode has some severe drawbacks. The data gathered in this mode do not necessarily display the real topography¹ of the investigated sample. Areas of same height but different softness for example will result in different deflection signals, which will then be misleadingly displayed as different heights in the resulting image (Fig. 3.10).

Additionally, the direct contact between probe and sample can easily damage the sample, for example when investigating soft biological samples.

More importantly, however, the resolution of this imaging mode is inherently limited by the size of the used tip. Images taken in this mode at the best display *lattice resolution*, only reproducing the periodicity of the underlying sample. Objects that are smaller than the probe used for imaging cannot be resolved. Hence, the sharpness of the tip is of critical importance. This means that in order to achieve real atomic resolution, *i.e.* to image single atoms or defects, the tip apex should ideally only consist of a single atom. This configuration may be present for a pristine tip, but is certainly lost once the tip comes into contact with the sample. Hence, real atomic resolution of the sample is usually not possible in the contact mode. The only exception known to me is the work of Ohnesorge *et al.*, who claim to have achieved real atomic resolution of the calcite(10.4) surface using the contact mode under liquid conditions.⁶⁰ However, only kinked monatomic step edges were presented as proof of real atomic resolution and the AFM was, in fact, operated in the *attractive* instead of the repulsive regime.

For contact mode AFM, two basic scanning modes have to be distinguished between. In the constant-height (CH) mode, the cantilever is held at a fixed distance to the sample and its deflection is measured. Using Hooke's law as described above, this results in a force map of the investigated sample. While this scanning mode is simple to realize and allows for high scanning

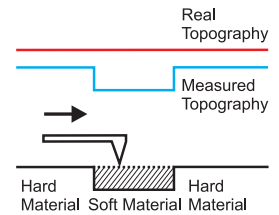


Figure 3.10: Real and measured topography signal for an inhomogeneous sample scanned in contact mode AFM.

¹The question of what can be considered real topography is in fact valid for all AFM operating modes.

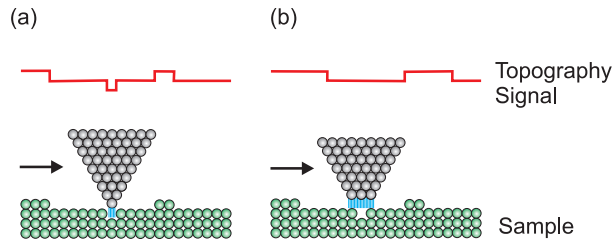


Figure 3.11: (a) Atomsically sharp tip. Single defects can be imaged. (b) Blunt tip. Single defects cannot be resolved. Additionally, terraces are imaged broader than they are.

speeds, the tip might either loose contact to the sample or can be destroyed by heavy collisions. Alternatively, the AFM can be operated in the constant-force (CF) mode, where the cantilever height is constantly adjusted to measure the same deflection. This requires the use of a feedback loop to regulate the distance of cantilever and sample. Its feedback signal is then used to generate a topography map of the sample. Due to the finite response time of the feedback loop, this mode leads to slower image acquisition compared to the CH-mode and the loop settings have to be individually adjusted for each sample. In return, samples of unknown height distribution can be imaged without risking the destruction of the tip or the sample.

The scanning mode always has to be chosen depending on the sample conditions. Whereas first scans on an unknown sample are often conducted in the CF mode, environmental variables such as high thermal drift might require higher scanning speeds, thus favoring the CH mode. Even more importantly, the CH mode allows for straight-forward interpretation the acquired data as the use of feedback loops always alters the original information.⁶¹

Dynamic Force Microscopy

In dynamic force microscopy, the cantilever is oscillated at or close to its eigenfrequency by an external actuator and brought

into close proximity of the sample. Interaction between the sample and the tip then leads to a change in the cantilever's oscillation properties. Fig. 3.12 illustrates how a change in the cantilever oscillation amplitude affects the measured frequency and vice versa.

Two important operating modes have to be distinguished between - amplitude modulation (AM-AFM) and frequency modulation (FM-AFM). The measurements presented in this thesis were performed using FM-AFM, operated in the non-contact regime (FM NC-AFM). In the NC-AFM mode, the tip ideally never comes into direct physical contact² with the surface. In contrast to static force microscopy, it is thus possible to maintain an atomically sharp tip, allowing for real atomic resolution in this operating mode.

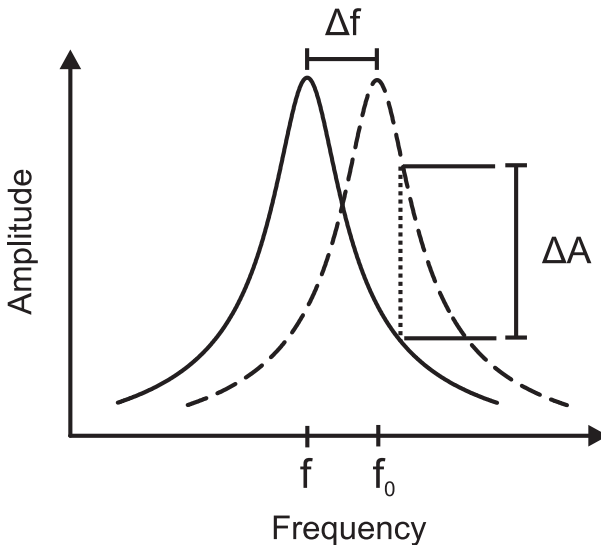


Figure 3.12: Typical cantilever resonance curves. A change in the cantilever resonance frequency results in an amplitude difference.

As already mentioned above, the cantilever stiffness k is of utmost importance concerning the sensitivity of the force measure-

²It should be noted, that no official definition for *contact* in dynamic force microscopy exists. Coming closest to this would be the static deflection of the cantilever upon approaching the sample.

ment. In contact mode AFM, k has to be very small to be sensitive to small forces. In the dynamic mode, however, other conditions apply. When approaching the tip towards the sample, the attractive forces might overcome the cantilever's restoring force as given by Hooke's law and result in a sudden contact of tip and sample. This undesired effect is called *snap into contact* and usually renders the tip useless for real atomic resolution. This can be avoided by choosing cantilevers with a higher stiffness that, for a given tip-sample force F_{ts} , fulfill the condition

$$k > \frac{\partial F_{ts}}{\partial z} = k_{ts} \quad (3.6)$$

In case of a cantilever oscillating with an amplitude A , this condition can be rewritten as⁶²

$$k \cdot A > F_{ts} \quad (3.7)$$

If this condition is fulfilled, the cantilever motion can be described as a weakly disturbed harmonic oscillator. Snap into contact is a major disturbance for dynamic mode AFM measurements conducted under ambient conditions, as every sample is inevitably coated with a thin water layer. As the tip comes into proximity of the sample, a meniscus is formed that draws the tip onto the sample surface. One possibility to avoid this is immersing tip and sample into a liquid during the measurement.⁶³

Amplitude Modulation

In amplitude modulation AFM (AM-AFM) as described by Martin *et al.*⁶⁴ the cantilever excitation frequency is kept constant and the change in amplitude and phase relative to the excitation signal is measured. AM-AFM can be operated in the non-contact as well as the repulsive regime. The latter is also called intermittent contact (IC) or Tapping[®] mode.⁶⁵ In that mode the tip touches the sample surface at the lower turning point of its oscillation cycle. In contrast to the static contact mode, the intermittent contact between tip and sample reduces the energy that is dissipated into the sample, minimizing the danger of destroying or re-arranging softer sample species. However, it is obviously not possible to maintain an atomically sharp tip in this imaging mode and the achievable resolution is, therefore, limited.

The system's response time in AM-AFM, after which the cantilever vibrational amplitude will settle into a new steady-state, is given by⁶⁶

$$\tau_{AM} \propto \frac{2Q}{f_0} \quad (3.8)$$

where Q is the quality factor of the excited oscillation and f_0 the cantilever eigenfrequency. For scanning under liquid or ambient conditions, quality factors are typically in the order of 10-100. Together with typical cantilever eigenfrequencies in the range of $10^4 - 10^5$ Hz, this results in reasonable response times. Under UHV conditions, however, quality factors go up several orders of magnitude as energy is dissipated only very slowly during the oscillation. Response times will, hence, increase heavily, thus restricting the measurement bandwidth and making the AM-AFM technique unfeasible for UHV applications. To give an example, for typical cantilever properties used in UHV ($f_0 = 300$ kHz, $Q = 30000$), this would result in a maximum available bandwidth of only 0.2 Hz. Artificially reducing the quality factor for UHV applications is not desirable either, as the minimum detectable force is proportional to $1/\sqrt{Q}$.⁶⁴

Frequency Modulation

As a solution for this problem, Albrecht *et al.* introduced the frequency modulation mode (FM-AFM),⁶⁶ where the cantilever is driven at its current resonance frequency f . In contrast to AM-AFM, the oscillation amplitude is kept constant here, using an amplitude feedback loop. Forces acting on the cantilever tip cause a deviation of the current resonance frequency from the cantilever eigenfrequency f_0 . This frequency shift Δf is defined as $\Delta f = f - f_0$ and can be expressed as follows:^{62,67}

$$\Delta f(z) = \frac{f_0}{\pi k A^2} \int_{-A}^A F_{ts}(z + A - q) \frac{q}{\sqrt{A^2 - q^2}} dq \quad (3.9)$$

Again, F_{ts} is the force acting between tip and sample, A the oscillation amplitude and k the cantilever stiffness. This frequency deviation, sometimes also called *detuning* is the primary imag-

ing signal in FM-AFM. The response time in FM-AFM⁶⁶

$$\tau_{FM} \propto \frac{1}{f_0} \quad (3.10)$$

is independent of the quality factor, making this technique suitable for measurements using high-Q cantilevers under UHV conditions. It can easily be seen from this equation that cantilevers with higher eigenfrequencies should allow for higher scanning speeds. The capability of FM-AFM to achieve real atomic resolution under UHV conditions has first been demonstrated by Giessibl *et al.* in 1995 by resolving the Si(111)-(7x7) surface.⁶⁸

FM-AFM measurements involve several important parameters, such as cantilever eigenfrequency and stiffness, the scanning speed and the oscillation amplitude. Finding a parameter set for optimal high-resolution imaging is, therefore, not trivial. Furthermore, the measurement process is of course influenced by the tip-sample potential. Among the most debated parameters, however, is the oscillation amplitude A . Calculating the noise for different conservative potentials shows, that vertical noise is minimal for small amplitudes ($A < 1$ nm).^{66,69} However, taking into account non-conservative potentials to account for dissipative processes, which are certainly present in FM-AFM, directly connects the choice of oscillation amplitude with the cantilever stiffness k . Considering this relation, optimal amplitudes in the order of 10 nm were determined for soft cantilevers with a stiffness around 10 - 20 N/m.⁶⁹ The cantilevers used in this thesis have stiffnesses in the same order of magnitude ($k \approx 30$ N/m), therefore, oscillation amplitudes around 10 nm were chosen for performing the measurements.

The dependance of the the acquired images on the shape of the tip as described before makes a straightforward quantitative comparison of FM-AFM data from different experimental sessions challenging. However, for cantilever oscillation amplitudes that are large compared to the tip-sample distance d at the lower turning point, the normalized frequency shift

$$\gamma(z, A) = \frac{kA^{3/2}}{f_0} \Delta f(z) \quad (3.11)$$

as introduced by Giessibl^{62,70} allows to compare data such as $\Delta f(z)$ spectroscopy curves taken at different amplitudes and with different cantilevers, as all cantilever parameters are eliminated.

Similar to the contact mode, dynamic force microscopy can be performed using two different scanning modes, namely performing measurements at constant height or constant interaction. For AM-AFM, constant interaction means keeping a constant amplitude, whereas in FM-AFM, the frequency shift Δf is kept constant. A visualization of the CH mode for AM-AFM and FM-AFM is given in Fig. 3.13.

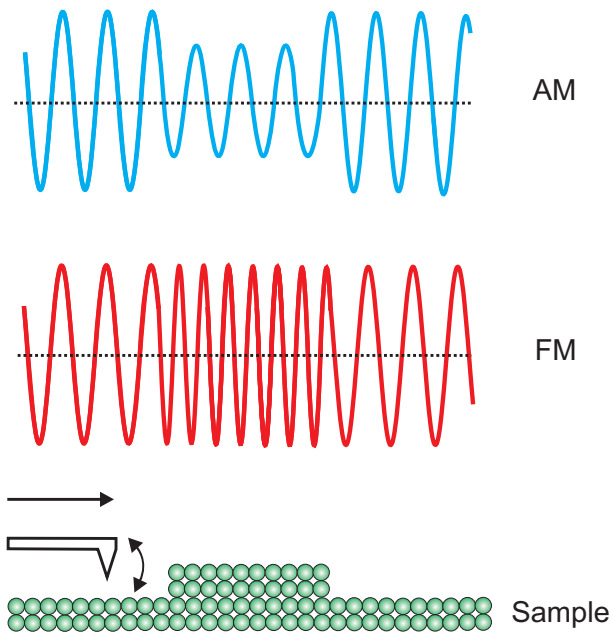


Figure 3.13: Visualization of amplitude modulation (AM) and frequency modulation (FM) mode when scanning over a surface feature. Note that both cases are drawn for the case of a repulsive interaction. Attractive interactions would cause an amplitude magnification in the AM mode and a decrease in frequency in the FM mode.

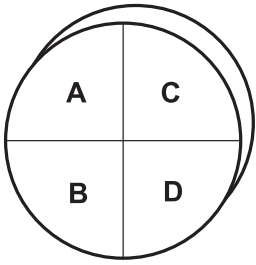


Figure 3.14: Four-quadrant photodiode as used in typical beam-deflection AFMs. The quadrants are named as in the VT AFM XA setup used in this thesis.

3.4 Deflection Detection Methods

Independent of the chosen operating mode, the key to high-resolution AFM measurements is the precise and low-noise detection of the cantilever deflection. In the original setup by Binnig and Rohrer, an STM has been used to measure the deflection of a gold-coated cantilever.⁴³ Whereas the exponential distance-dependence of the tunneling current has yielded very good vertical resolution, this setup has been very complex in operation and has soon been replaced by more efficient methods. Methods nowadays range from interferometers⁷¹ over capacitive sensors⁷² to piezoresistive cantilevers.⁷³ Among the most commonly used techniques today are laser beam deflection and the use of self-sensing devices which will be described in the following.

Laser Beam Deflection

In the most simple case, the backside of a cantilever is irradiated by a laser beam that is in turn reflected onto a position sensitive device (PSD). A deflection of the cantilever then leads to a movement of the laser spot on the PSD with the same frequency. This movement is converted to a voltage signal and processed by the signal electronics. In most beam-deflection AFMs, a four-quadrant photodiode as shown in Fig. 3.14 is used. The difference between signal intensity in the upper and the lower half yields the deflection that is caused by the cantilever motion along the surface normal, often called the F_N -signal. In NC-AFM, this usually is a sinusoidal signal. Lateral forces leading to torsion movements of the cantilever can be detected accordingly by subtracting the signals of the left and right half of the PSD (F_L -signal).

It is important to note how the measured F_N -signal is related to the physical oscillation of the cantilever. Analysis of the sinusoidal signal coming from the PSD yields an oscillation amplitude that is not measured in nanometers but in Volts. Using an amplitude calibration process as described e.g. by Simon *et al.*,⁷⁴

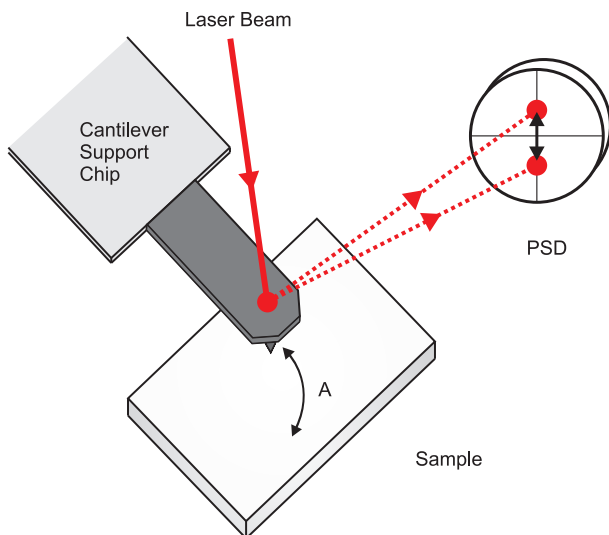
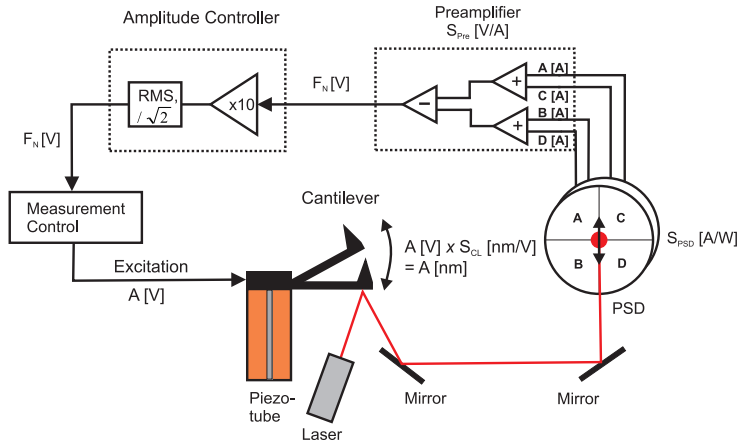


Figure 3.15: Principle of beam deflection technique. Oscillation of the cantilever leads to a movement of the laser spot on the PSD.

the electronic amplitude can be related to the physical amplitude of the cantilever *via* a sensitivity factor S_{CL} in the units [nm/V]. This sensitivity already contains the amplification factors of the electronics involved in the readout process. It has, thus, to be re-determined when parts of the electronics, *e.g.* the preamplifier, are changed. Additionally, its absolute value depends on the cantilever properties such as stiffness and position relative to the PSD. Due to the gluing process, every cantilever support chip has a slightly different position on its supporting holder, so that the alignment of the laser beam on the cantilever back has to be readjusted every time the cantilever is changed. This also affects the calculation of the cantilever sensitivity which has to be repeated for every new cantilever. While this sensitivity factor is around the same value for cantilevers of similar dimensions, knowledge of the exact value and the resulting physical oscillation amplitude is of importance when calculating absolute interaction force values.

Beam deflection is a versatile technique that can be implemented under UHV- as well as ambient and liquid conditions. It has,

Figure 3.16: Sketch of the beam deflection setup for the VT AFM XA used in this thesis. The sensitivities S_i are needed to determine the physical oscillation amplitude of the cantilever.



therefore, become one of the most commonly used deflection detection methods in commercial AFMs today. Atomic resolution on various substrates can be achieved on a daily basis using this technique. If not stated otherwise, the images displayed in this thesis were obtained using the beam deflection technique.

Self-Sensing Devices

By replacing the cantilever with a piezoelectric probe, it is possible to measure the deflection by the charges that are induced in the device upon mechanical stress, utilizing the piezo electrical effect. That way, no laser beam setup is needed here and the procedure of optical alignment becomes obsolete. A prominent example for a piezo-electric probe is the quartz tuning fork sensor. First SPM measurements with quartz tuning forks were performed by Günther *et al.* in 1989,⁷⁵ who were using them as force sensors in a scanning near-field acoustic microscope. Fig. 3.17 shows a schematic drawing of such a tuning fork. A special form of tuning forks for use in NC-AFM applications was introduced by Giessibl in 2000 under the name of qPlus sensor.⁷⁶

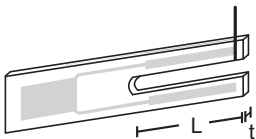


Figure 3.17: Schematic drawing of a tuning fork of length L and width t for use as force sensor. It is equipped with a tip at the end of one prong. Electrodes for signal read-out are indicated by the shaded areas.

Fig. 3.18 shows a typical qPlus sensor as manufactured by Omicron Nanotechnology. The centerpiece is a piezoelectrical quartz tuning fork as can also be found in common wrist watches. Both

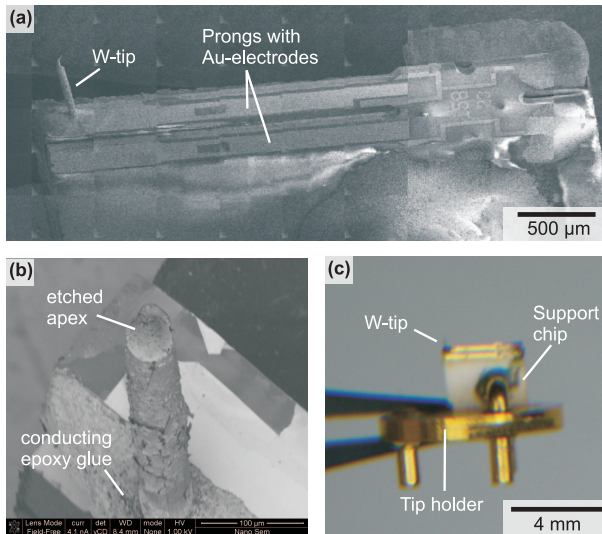


Figure 3.18: (a,b) SEM images of a tuning fork sensor. The apex of the tungsten tip is bent due to a contact of tip and sample during scanning (SEM images courtesy of [redacted]). (c) Tuning fork sensor mounted on tip holder for use in an Omicron VT AFM.

prongs are equipped with horizontal and vertical gold electrodes which are used for the read-out mechanism. By gluing one of the prongs to a supporting chip, the tuning fork is turned into a cantilever and the system's eigenfrequency is reduced from initially $f_0 = 2^{15}$ Hz to typical values of $f_0 \approx 20 - 30$ kHz. The quartz cantilever can then be equipped with different probes, ranging from fine tungsten wires to single-crystal tips, depending on the desired application. Using conducting tip materials also enables simultaneous STM and qPlus-AFM measurements on conducting surfaces. The sensitivity needed for the calculation of the physical oscillation amplitude only depends on material parameters and can, thus, be considered constant for a given tuning fork type.

Tuning fork cantilevers have two important key features. The first one is their high temperature stability that is achieved by etching the tuning forks from specially oriented quartz crystals. Compared to silicon, this so called quartz-crystal X + 5° cut dis-

plays a very low temperature variation, resulting in a high frequency stability. This temperature variation is especially low for temperatures around 5 K and 300 K respectively, temperature regimes that are both common for scanning probe measurements.⁷⁷ The second is their high stiffness of typically $k_{\text{qPlus}} = 1800 \text{ N/m}$ which allows to fulfill the condition $k \cdot A > F_{ts}$ even for oscillation amplitudes below 1 nm. This small amplitude operation should make the qPlus sensor more sensitive to the short-range chemical forces which are of primary interest for the contrast formation in AFM. At the same time, the high stiffness accounts for amplitude instabilities that would otherwise limit small amplitude measurements.⁷⁷

Although having the advantage of the simpler *in-situ* setup as compared to beam deflection, working with amplitudes that small poses different challenges. Most importantly, the small cantilever deflections will result in very small signals that are generated in this setup. For a tuning fork prong of length L and thickness t , the charge q that is collected upon a deflection z of the cantilever is given by⁷⁶

$$q(z) = 12 \cdot d_{21} k L_e (L_e/2 - L) / t^2 \cdot z \quad (3.12)$$

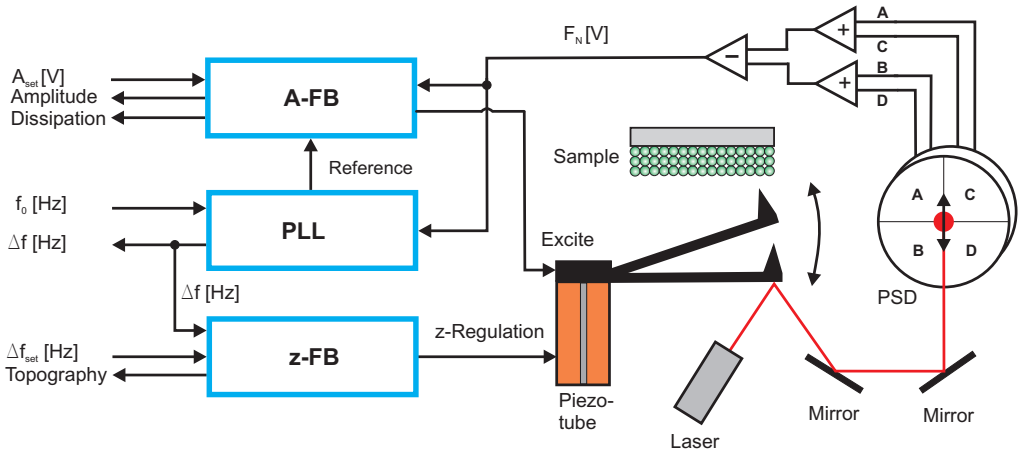
with L_e being the length of the gold electrodes, d_{21} the corresponding part of the piezoelectrical tensor and k the prong's stiffness. For typical quartz tuning forks, this results in a sensitivity of $q/z < 10 \mu\text{C m}^{-1}$.⁷⁶ This makes high demands on the detection amplifiers and requires the use of sophisticated low-noise electronics.

Atomic resolution using the qPlus setup has been achieved on several insulating substrates under UHV conditions,^{76,78,79} some even claiming sub-atomic resolution.⁸⁰ Under ambient and liquid conditions, however, monatomic steps could be resolved but no lateral atomic resolution has been achieved so far.⁸¹

3.5 Feedback Loops in NC-AFM

For FM-AFM operation as performed for the measurements presented in this thesis, the oscillation signal F_N is processed by

three interconnected feedback loops (FB) as depicted in Fig. 3.19.



The **amplitude feedback loop** determines the current oscillation amplitude from the F_N -signal and adjusts it to a given setpoint A_{set} by applying a voltage to the cantilever excitation piezo. The energy needed to sustain the oscillation at a constant amplitude is proportional to the energy that is dissipated during the scanning process. Thus, dissipation energy and current amplitude can be mapped during the scanning process.

The **phase-locked loop** determines the frequency f of the F_N -signal and compares it to the cantilever's eigenfrequency f_0 . The resulting detuning signal $\Delta f = f - f_0$ is the main imaging signal.

The **z-distance feedback loop** adjusts the distance between tip and sample by applying a voltage to the z-piezo until the detuning signal from the PLL matches the setpoint Δf_{set} . This voltage signal can then be converted into a topography signal.

The interplay of these three feedback loops makes the technique of NC-AFM quite elaborate when compared to other SPM methods. In STM for example, only a z-distance feedback loop is needed for operation. Yet, the achievable high resolution combined with the possibility to image insulating substrates more than justifies these efforts.

Figure 3.19: Schematic setup of VT AFM XA. Left side: Amplitude feedback loop (A-FB), phase-locked loop (PLL) and z-distance feedback loop (z-FB). Right side: Scanhead including cantilever, sample and beam-deflection setup.

4 Setup of the UHV AFM System

Contents

4.1 UHV System	38
4.2 Scanhead	39
4.3 Sensor and Sample Preparation	41
AFM Tip Preparation	41
Preparation of Calcite Crystals	42
Molecule Deposition	43
4.4 Data Processing and Analysis	45
Error Analysis	45

AT the beginning of this thesis, a new UHV system equipped with a commercial VT AFM XA scanhead from Omicron Nanotechnology (Taunusstein, Germany) was set up. The basic set-up is similar to the already existing VT AFM 25 system in our group. I will, therefore, only summarize the basic aspects of the new system, and describe some of the more important changes in greater detail.

4.1 UHV System

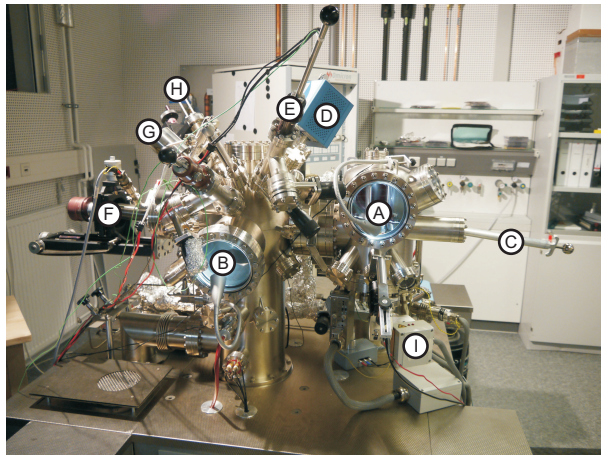


Figure 4.1: UHV system. A: AFM chamber, B: Preparation chamber, C: Wobble stick manipulator, D: Quadrupole mass spectrometer, E: Molecule sublimator, F: Sample manipulator, G: Sputter gun, H: Quartz crystal microbalance, I: Laser source

The UHV system consists of two stainless steel chambers with a base pressure of $p < 1 \cdot 10^{-10}$ mbar. One chamber is used for sample and tip preparation, whereas the other one houses the scanhead. Both chambers are equipped with individual ion getter and titan sublimation pumps to achieve the low pressure necessary. The chambers can be separated by an additional valve in order to avoid contamination of the scanhead during sample preparation. Pressure is constantly monitored using ion gauge heads in both chambers. Additionally, a quadrupole mass spectrometer (eVision⁺, MKS Instruments) in the preparation chamber can be used to analyze gas residues from contaminants in the system or to check the UHV system for possible leaks.

The entire setup is mounted on pneumatic damping legs (S-2000 series, Newport) that isolate the system from external vibrational noise sources such as building vibrations.

Samples and tips are locked in to the preparation chamber by using a separately pumped load-lock that enables quick sample

exchanges without having to vent the entire system. Additionally, up to twelve samples and tips can be stored under UHV conditions in a carousel in the scanhead chamber. Transfer of tips and samples between the chambers is realized with a wobblestick manipulator.

Samples can be prepared by annealing or cooling using an integrated sample manipulator (VG Scienta, Uppsala, Sweden) equipped with a separate heating and cooling stage. Two heating options are realized in the heating stage: Resistive heating (RH), where a pyrolytic boron nitride (PBN) heater is brought into contact with the sample plate and direct heating (DH), where a current is applied to the sample itself. With the PBN heater, temperatures of up to 1200 K can be achieved, while DH reaches temperatures of up to 1500 K. The latter method is used for the preparation of samples like Si(111), where the (7×7) reconstruction is induced by repeatedly applying high current pulses to the sample ('flashing'). This method of course requires conducting samples. Insulating samples such as the calcite crystals used in this work are, therefore, degassed and annealed using the RH-option. For preparing samples at low temperatures, the manipulator can be cooled using liquid nitrogen, bringing the cooling stage to temperatures around 110 K.

4.2 Scanhead

The VT AFM XA scanhead is equipped for beam-deflection AFM, STM and qPlus AFM/STM operation. To avoid unwanted vibrations, the scanhead is suspended on four spiral springs and held in place by an eddy-current damping stage as shown in Fig. 4.2 (a).

The sample is mounted overhead in the sample stage while the sensor is approached using a piezoceramic tube (Fig. 4.2 (b)). Excitation of the tip is realized using a separate excitation piezo element on top of the tube. The laserlight necessary for beam-deflection detection is coupled into the system using an optical fiber and led through the hollow core of the piezo tube. It is deflected from the backside of the cantilever onto a small mirror,

also set on top of the piezo tube, and focused onto the PSD by a second mirror (not shown). Both mirrors can be readjusted individually. The deflection signal from the PSD is amplified by a preamplifier setup and fed into the Omicron MATRIX scan controller for further processing and data acquisition.

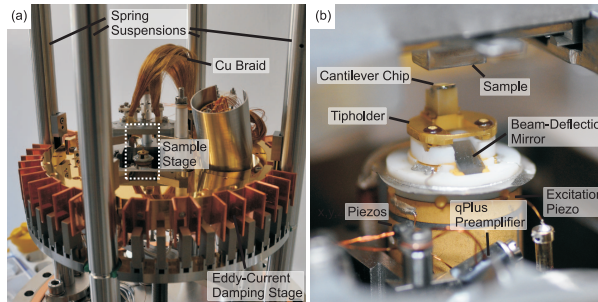


Figure 4.2: (a) VT AFM XA scanhead suspended on springs for vibration isolation. (b) Zoom on the sample stage.

Different preamplifier setups are used for beam-deflection and qPlus operation. As the charges induced in the tuning fork setup are very small the first amplifier stage has to be close to the sensor in order to avoid parasitic capacitances caused by the wiring, thus minimizing unwanted electric noise. In this setup, the I/V-converter is attached to the scanner piezo tube as shown in Fig. 4.2 (b). With charges induced in the sensor being in the order of 10^{-6} C, the amplifier has to be very sensitive, which at the same time makes it prone to damages by stray charges. This also limits the bias voltage that can be applied to compensate electrostatic forces. Whereas for a scanhead without qPlus preamplifier, bias voltages of up to 100 V can be applied without damaging the instrument, the limit is 25 V with the qPlus setup.

Using an external liquid He flow cryostat and a PBN heater integrated in the scanhead's sample stage, variable temperature measurements in the range from 50 K to 500 K are possible. Thermal contact to the sample stage is realized by a braid of thin Cu-wires while the temperature is monitored using an Si diode at the cryostat and a Pt100 sensor at the stage. The flow cryostat can also be operated using liquid nitrogen instead of helium, increasing the lower temperature limit to 110 K. In

contrast to low-temperature scanners, only the sample temperature is changed while the scanner itself remains at room temperature. This enables the investigation of samples at variable temperatures (VT) which is of importance for the determination of sample properties such as diffusion energy barriers or activation energies. In regular operation, the heating element is used to keep the sample stage at a defined temperature slightly above room temperature. That way the effects of thermal drift as are induced by daytime temperature variations are minimized.

4.3 Sensor and Sample Preparation

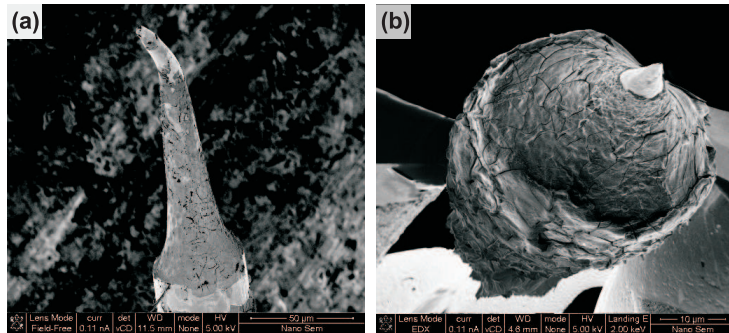
In order to insure that no contamination of the investigated samples occurs, a thorough preparation of the involved materials is of utmost importance. Especially components that were stored *ex-situ* under ambient conditions are usually coated with an oxide layer and have to be cleaned before using them.

AFM Tip Preparation

Beam-deflection cantilevers (Type PPP-NCH, Nanosensors, Neuchâtel, Switzerland) are sputtered with Ar ions at 2 keV for 5 min prior to use to remove the oxide layer. For that purpose the preparation chamber is flushed with Ar gas which is, in turn, ionized by an ISE5 sputter gun (Omicron Nanotechnology). The sputtering removes the oxide layer and can also improve the cantilever's oscillation properties.⁸² Using lower energies, the same procedure can in theory also be applied to prepare qPlus sensors.

However, experiments performed in our group showed that STM as well as AFM measurements using qPlus sensors at room temperature suffer from severe instabilities during the scanning process, regardless of whether they were ion bombarded or not. Additional SEM investigations of several qPlus sensors, carried out by R. Branscheid, showed that the tip appears to be coated with a thick layer of unknown adsorbates (Fig. 4.3). These adsorbates

Figure 4.3: SEM images of two qPlus tungsten tips. In both images, the adsorbate layer is clearly visible. (a) Tip already used for scanning. The bending results from contact of tip and sample. (b) Top view of pristine W-tip. Images courtesy of [REDACTED].



are most likely dropped from the tip during the scanning process, thus leading to the observed instabilities. An energy dispersive X-ray spectroscopy (EDX) analysis of these adsorbates identified, amongst others, residues of silver and sodium, most probably resulting from the conductive epoxy glue and the etching solution. The SEM and EDX results clearly demonstrate, that the fabrication process of the qPlus sensors has to be refined.

The majority of high-resolution qPlus experiments known to me are conducted at low temperatures where the mentioned instabilities can largely be neglected.^{79,83–85} However, the aim of this thesis involves the stable imaging of molecular self-assembly processes at room temperature. I, therefore, decided to perform my measurements using the beam deflection technique as described before.

Preparation of Calcite Crystals

All experiments described in this work were conducted on insulating calcite crystals.¹ The crystals are purchased from Korth Kristalle GmbH (Altenholz, Germany). They are cut into rectangular bars with a cross section of $2 \times 4 \text{ mm}^2$ displaying the calcite (10.4) surface and mounted into a specially designed clamp holder which was optimized for cleaving crystals (Fig. 4.4 (a)).⁸⁶

¹The crystal's properties as well as the relevant (10.4) surface are described in detail in Chap. 5.

After locking in into the UHV preparation chamber, the crystals are degassed for at least one hour at typically 525 K to remove contaminants. They are then cleaved *in-situ* by running a scalpel parallel to the (10.4) plane. Depending on the crystal's length, this cleaving process can be repeated several times, yielding a fresh surface every time.

Ionic crystal are known to accumulate charges when cleaved under UHV conditions.^{87,88} These long-range electrostatic forces can cause a major hindrance for the acquisition of NC-AFM data. For that reason, the crystals are subsequentially annealed at 475 K for one hour to remove these charges. The so-prepared sample is then transferred into the AFM chamber and first scans are performed to confirm the purity of the sample surface.

After use, the sample holders are locked out of the UHV system and thoroughly cleaned in a supersonic bath before re-using them. Otherwise molecular material that still adheres to the sample holder might contaminate the new sample.

Molecule Deposition

Molecules are deposited onto the sample surface by using a home-built Knudsen-cell as shown in Fig. 4.4 (b). Tantalum wire acting as a heating coil is wound around a small glass crucible of typically 4 mm diameter and a type K thermocouple (chromel/alumel) for temperature measurements is molten into one end of the crucible. The crucible is then filled with the desired molecules, most of which are available as a fine powder. As the sublimator cell is mounted overhead in the UHV chamber, glass wool is used to prevent the molecular material from falling out of the crucible.

The completed cell is then mounted on a UHV feedthrough and attached to a test chamber equipped with a quartz crystal microbalance (Inficon, Bad Ragaz, Switzerland) to determine the deposition rate. That way, substances of unknown purity can be tested without risking contamination of the AFM system.

The molecular sublimation rate r at a given temperature T fol-

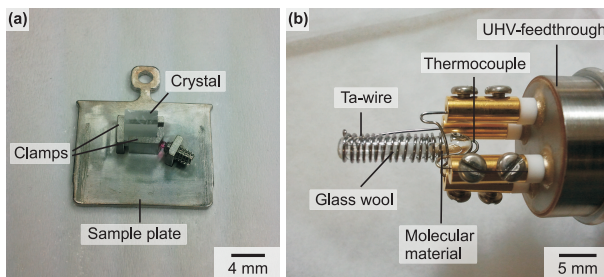


Figure 4.4: (a) Sample holder with calcite crystal. Cleaving is performed by running the scalpel along the clamp edge. (b) Typical sublimation cell mounted on a UHV feedthrough.

lows an Arrhenius law

$$r = r_0 \exp\left(\frac{\Delta H_{sub}}{k_B T}\right) \quad (4.1)$$

where k_B is the Boltzmann constant and ΔH_{sub} is the sublimation enthalpy of the molecule in question. Using this relation, the molecular sublimation enthalpy can easily be obtained.

This sublimator setup allows for a precise control over the molecular deposition parameters and different coverages can reproducibly be achieved.

For molecules whose vapor pressure does not allow sublimation under UHV conditions, the UHV chamber can be equipped with a pulse valve system (Parker-Hannifin, Cleveland, Ohio) that allows molecular deposition from liquid solutions. To avoid contamination of the UHV system with the solvent the pulse valve is attached to the separately pumped load lock. After deposition, the sample has to be annealed to remove the remaining solvent. Whereas first tests demonstrated the successful deposition of salicylic acid from solution, the quantitative control of molecular coverage on the sample remains challenging.⁸⁹

4.4 Data Processing and Analysis

The acquired images were processed using the open-source software Gwyddion, which was developed for SPM data visualization.⁹⁰ For data representation, a color scale as shown in Fig. 4.5 is used. The images are displayed such that bright colors correspond to high attractive interaction while dark colors correspond to less attractive or even repulsive interaction. For frequency shift images (Δf) this is achieved by inverting the color scale. Apart from that, all frequency shift images presented are raw data if not stated otherwise. For the topography data (z) a plane subtraction is applied to account for misalignment of sample and scanner plane.

Figure 4.5:
Color-scale
used for data
representation.



Error Analysis

All SPM measurements are subject to thermal drift which is about the most important error source. Due to different thermal expansion coefficients, scanner and sample will react differently to temperature changes. Even though these effects may be negligible on a macroscopic scale, small temperature changes can amount to a significant effect on the nanometer scale, leading to distorted images and errors in lateral distance measurements. In addition to this, vertical drift can cause the tip to collide with the sample, damaging both tip and sample. Several techniques can be applied to account for this effect.

During the measurement itself, the temperature of AFM sample stage can be actively controlled to minimize temperature gradients (Fig. 4.6). Additionally, an active drift compensation can be applied, for example by using the so-called atom-tracking technique.^{91,92} In that case, the tip is circulated around a single surface atom and the drift in x-,y- and z-direction is extrapolated over time. The drift vectors obtained in that way can then be

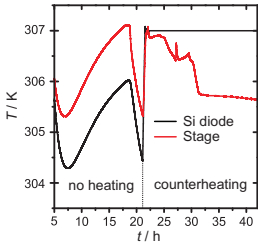


Figure 4.6: Sample stage temperature with and without counterheating. Fluctuations in sample stage temperature after the start of counterheating originate from sample handling during the day.

used to readjust tip position and height while scanning and thus largely compensate the effects of thermal drift. One of the most important features of this technique is the possibility to cope with thermal drift effects even at high temperature gradients. Ref. ⁹³ describes in detail the implementation of such an atom-tracking system for the UHV AFMs used in our group.

During post processing, images can be corrected for thermal drift by selecting a distinct feature such as an atomic defect and tracking its position over a series of consecutive images. Applying the algorithm described in Ref. ⁹⁴, the images can then be manually distorted to account for the drift. However, it should be noted that this post-processing method is only applicable for *linear* drift effects. Alternatively, known structures such as the substrate's periodicity can be used as an inherent reference length scale.

While thermal drift affects lateral as well as vertical distance measurements, an additional effect has to be taken into account when interpreting height measurements. The measured heights in NC-AFM represent a plane of equal interaction and might, for that reason, also be influenced by electrostatic forces. ^{95,96} This effect is especially pronounced when comparing heights of different materials. One possibility to account for the effect of electrostatic forces on height measurements would be to use a KPFM-controlled feedback loop. ⁹⁷ However, while electrostatic interactions can be compensated that way, chemical and van der Waals interactions will still contribute to the measurement signal. The interpretation of height measurements in NC-AFM, therefore, always has to be treated with great caution.

5 The Bulk Insulator Calcite

CALCITE (CaCO_3) belongs to the class of carbonate materials and is the most stable polymorph of calcium carbonate. Two other modifications are found in nature, namely aragonite and vaterite ($\mu\text{-CaCO}_3$). Both are thermodynamically unstable under standard conditions and, over time, transform into calcite. In addition to these natural modifications, several artificial modifications, named calcite I - V, have been synthesized under high-pressure and/or high-temperature conditions.⁹⁸

The application of calcium carbonates are manifold. Calcite plays an important role in biomineralization where the motivation is to understand and control its formation process and to fine-tune the resulting materials' properties by interaction with organic molecules.⁹⁹ Calcium carbonate is also used in many industrial products such as paints, paper chemicals, cosmetics and pharmaceuticals.¹⁰⁰ Due to its strong birefringence it is a preferable material for use in optics, *e.g.* as polarizing prisms.^{101,102} Research involving calcium carbonates is even of great interest for the oil-producing industry as more than 40 % of the world's oil reserves are located in calcareous rocks.¹⁰³ Furthermore, adsorption of organic molecules onto calcite has been discussed as a possible origin for the homochirality of life.^{104,105}

For the research conducted in this thesis, the interaction of calcite with organic molecules and its properties as a solid state ionic crystal are of interest. Being a bulk insulator with a band gap of $E_{\text{gap}} = 6.0 \text{ eV}$,¹⁰⁶ calcite makes an ideal candidate for the

decoupling of substrate and circuits in future molecular electronics applications.

In this thesis, I will use the hexagonal representation of the calcite bulk unit cell. Using the abbreviated four-symbol Miller Bravais indices $[hkil]$, the most stable cleavage plane is then denoted as the (10.4) surface. The dot herein represents the index $i = -h - k$. A detailed description of the calcite bulk properties can be found in the dissertation of P. Rahe.¹⁰⁷ Here, I will only discuss the most important properties of the (10.4) cleavage plane relevant to this work.

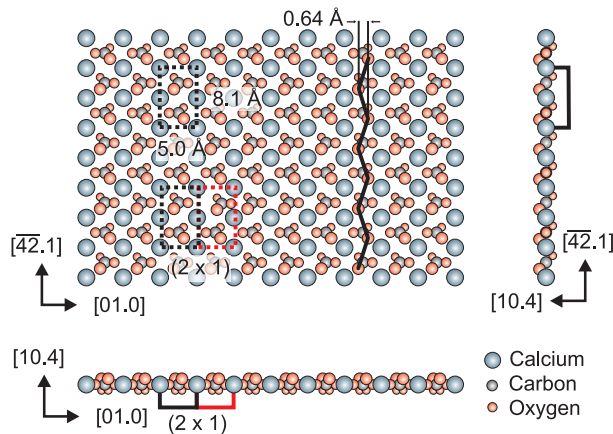


Figure 5.1: Sketch of the calcite (10.4) surface together with projections along the $[01.0]$ and $[\bar{4}2.1]$ direction. The reconstructed (2×1) surface unit cell and the zigzag of the topmost oxygen atoms are indicated in addition to the unreconstructed unit cell.

The calcite (10.4) surface has been proven to exhibit a significant templating effect on the adsorption of a considerable amount of organic molecules.¹⁰⁸ Additionally, its surface energy of $\gamma_S = 590 \text{ mJ m}^{-2}$ is among the highest for the prototypical insulating substrates such as KBr, NaCl or CaF_2 , making this surface an ideal candidate for the study of molecular self-assembly.²⁵

The surface unit cell of the studied (10.4) calcite cleavage plane is rectangular with dimensions of $a \times b = 8.1 \text{ \AA} \times 5.0 \text{ \AA}$ as shown in Fig. 5.1. It contains two carbonate groups, which are ro-

tated with respect to the surface normal and with respect to each other. This leads to a characteristic zigzag structure of the topmost oxygen atoms along the $[\overline{42}.1]$ direction. Observation of this zigzag in AFM images, therefore, hints at the carbonate groups being responsible for the contrast formation on this cleavage plane. Additionally, two important surface reconstructions exist, which are shown in Fig. 5.2.

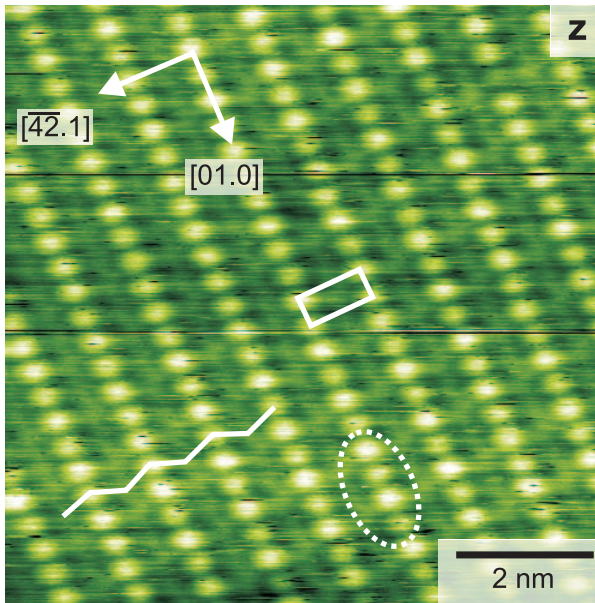


Figure 5.2: AFM topography image of a pristine calcite(10.4) surface. The unreconstructed surface unit cell is given by the white rectangle. Especially in the lower part of the image, the (2×1) reconstruction is clearly visible as spots of alternating brightness along $[01.0]$ (dashed ellipse). Along $[\overline{42}.1]$, the row-pairing reconstruction is very pronounced - clear corrugation is only seen on every second row. The carbonate group zigzag is slightly visible as well.

Atomic force microscopy and low-energy electron diffraction (LEED) studies have revealed clear signs of a (2×1) reconstruction of the (10.4) surface.^{109,110} The visibility of this surface reconstruction is highly dependent on the distance between tip and sample and its existence has, therefore, long been disputed.

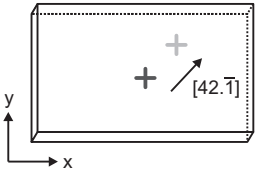


Figure 5.3: Birefringence will cause a displacement of the cross along the $[42.\bar{1}]$ direction. x and y match the (x,y) coordinates in the AFM image.

The so-called row-pairing reconstruction,¹¹¹ where every second row along the $[42.1]$ direction is imaged brighter than the one before has only been observed in AFM studies so far. It is therefore not unambiguously clear whether it is a real surface feature or an imaging artifact inherent to the AFM technique. A solid proof of its existence, however, would resolve the still open question of whether the calcite(10.4) surface is chiral or not.^{107,112}

It is important to note that, in contrast to surfaces such as NaCl(100), the calcite(10.4) surface is not highly symmetric due to these surface reconstructions. Altogether, this leads to a variety of contrasts that can be observed on the calcite(10.4) surface using NC-AFM in UHV.¹¹³

For the correct interpretation of measurement data, it is sometimes important to determine the absolute orientation of the sample, *e.g.* when investigating surface relaxation processes.¹¹⁴ From NC-AFM measurements alone, however, the orientation of the carbonate groups cannot be obtained. Measuring the atomic distances will, therefore, only yield a relative orientation, but the opposing surface directions $[\bar{4}2.1]$ and $[42.\bar{1}]$ cannot be distinguished. However, the crystal's birefringence can be used to determine the absolute orientation of a calcite sample surface as has been presented by P. Rahe.¹⁰⁷ In the case of light passing perpendicular to the (10.4) surface, calculation of the Poynting vectors for ordinary and extraordinary ray reveals a displacement of the extraordinary ray along the $[42.\bar{1}]$ direction.¹⁰⁷ Placing the crystal on a defined structure as illustrated in Fig. 5.3 and observing the direction of the split will, therefore, allow for an unambiguous identification of the crystal orientation. This orientational information can, later on, be transferred to the measurement data by relating the coordinate systems of sample holder and scanner.

6 Shape-Persistent Oligo(*p*-benzamide)s

Contents

6.1 Introduction	52
6.2 OIB	56
6.3 OIBal	61
6.4 OIBca	64
6.5 Further Iodobenzene Systems	67
6.6 Conclusions	71

IN this chapter, I will present a linking strategy based on the development of a versatile molecule from the class of shape-persistent oligo(*p*-benzamide)s that provides stable and site-specific anchoring of the molecular building block towards calcite(10.4).¹¹⁵ The strong anchoring towards the surface achieved in that way results in a well-defined adsorption position. At the same time, the anchor does not interfere with the intermolecular interaction, ensuring structural flexibility.

All molecules used in this study were kindly provided by [REDACTED] through a collaboration with the group of [REDACTED] at the University of Fribourg.

6.1 Introduction

Due to their inherently extended chain structure¹¹⁶ and their ability to form hydrogen bonds between chains,^{117–119} shape-persistent oligo(*p*-benzamide)s are promising candidates for use as supramolecular building blocks and the creation of molecular rods.^{119–122} The molecular building block investigated here is specially designed to allow for electrostatic interaction of iodine atoms with the surface calcium ions, thus ensuring a strong and site-specific anchoring. At the same time, the iodine atoms do not interfere with the intermolecular interaction that is encoded in the functional groups attached to the molecular core.

The molecules presented in the next sections are variations of 2-hydroxy-4-iodo-*N*-(4-iodophenyl)benzamide. Their structural models are shown in Fig. 6.1 (a-c). The different molecules are named according to their functionalization. Due to the aromatic backbone of two iodobenzene units connected *via* an amide bond, the building block molecule (Fig. 6.1 a) is referred to as *oligo iodo benzamide* (OIB). The other two molecules are OIBal with an added hexyloxy group (Fig. 6.1 b) and OIBca equipped with an additional carboxylic acid group at the end of the hexyloxy chain (Fig. 6.1 c).

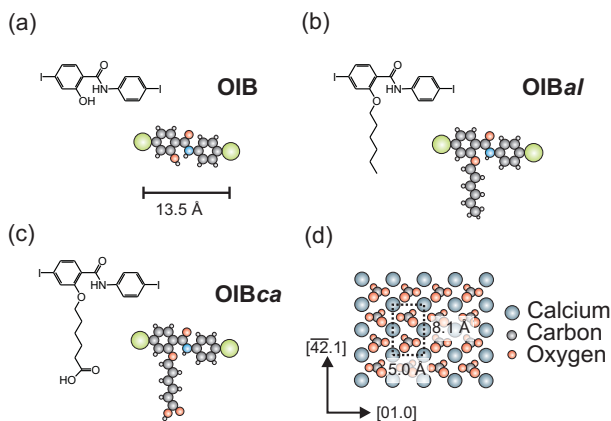


Figure 6.1: (a-c) Skeleton formulas and ball models of the oligo(*p*-benzamide) molecules used in this study. (d) Model of the calcite(10.4) surface drawn to scale.

Using a quartz crystal microbalance setup it was verified that all molecules are suitable for sublimation, while at the same time determining their respective sublimation enthalpies ΔH_{sub} (Fig. 6.2). The obtained values are $\Delta H_{\text{sub}} = (1.48 \pm 0.08) \text{ eV}$ for OIB, $\Delta H_{\text{sub}} = (1.21 \pm 0.1) \text{ eV}$ for OIBca and $\Delta H_{\text{sub}} = (1.68 \pm 0.08) \text{ eV}$ for OIBal. All values are very close, which can easily be explained by their common aromatic backbone. The deviations are caused by the different molecular functionalizations, demonstrating the different interaction strength in the bulk phase.

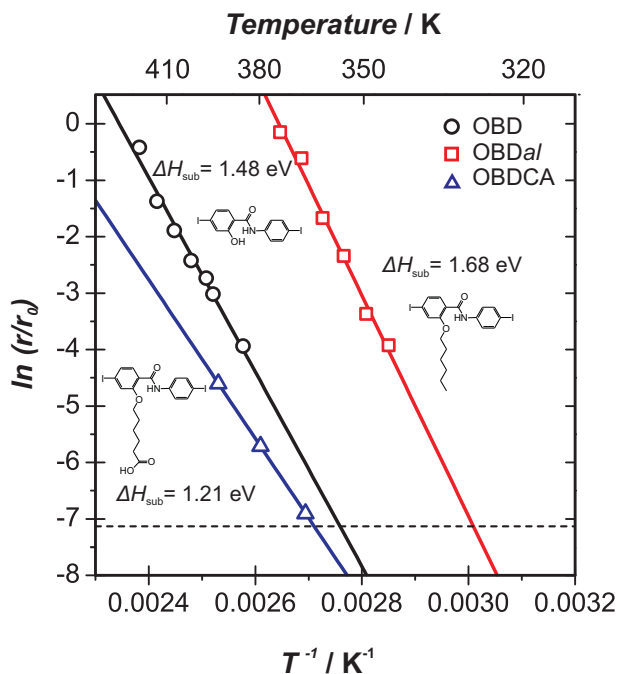


Figure 6.2: Arrhenius plots including sublimation enthalpies (ΔH_{sub}) for the oligo(*p*-benzamide) molecules used in this study. The dashed line indicates the resolution limit of the setup.

Before presenting the observed structures of the three different molecules, I will discuss the expected interaction of the core building block with the calcite substrate. Based on the previous success of electrostatic anchoring,^{16,21,30–34} I make use of electronegative atoms that can provide electrostatic attraction towards the surface calcium cations. The common core constituted

by OIB is equipped with two iodine atoms at a center-to-center distance of 13.5 Å. It can be expected that the adsorption position is governed by a common motif, namely that both iodine atoms are preferred to be centered directly above surface calcium ions, thereby maximizing the attractive molecule-substrate interaction.

When positioning one of the iodine atoms on top of a surface calcium cation, possible adsorption positions for the second iodine atom lie on a circle with a radius of 13.5 Å. The three Ca ions that lie closest to the circle representing the three best molecular adsorption configurations in terms of iodine-calcium match are presented in Fig. 6.3. Tab. 6.1 summarizes the Ca-Ca distances, angles and deviations from the I-I distance for these three best adsorption geometries. In the best two configurations (position **1** and **2**) the I-I distance fits excellently to the distance of the underlying calcium ions with deviations smaller than 5% (0.4 Å and 0.6 Å) while the third best choice (position **3**) is already significantly less favorable with a deviation of ~10% (1.3 Å). Note that for each adsorption configuration there is an equivalent mirrored configuration with the mirror axis along $[\overline{42}.1]$.

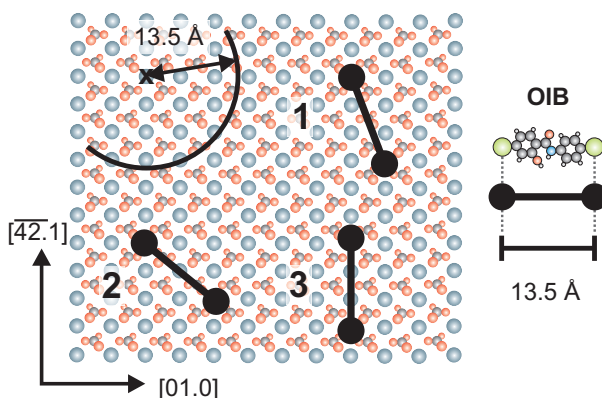


Figure 6.3: Determination of preferable adsorption positions for OIB on calcite(10.4). The black discs represent the iodine atoms with their covalent diameter. The three configurations that provide the best match of the distances between the molecule's iodine and the substrate's calcium atoms are drawn. For angles and distances see Tab. 6.1.

Pos.	Angle towards $[\overline{42.1}]$	Ca-Ca distance	Dev. from I-I distance
1	22.4°	13.1 Å	-0.4 Å
2	51.0°	12.9 Å	-0.6 Å
3	0°	12.2 Å	-1.3 Å

Table 6.1: Structural fit of the OIB adsorption positions from Fig. 6.3

This purely electrostatic picture clearly favors two adsorption configurations (positions **1** and **2** in Fig. 6.3) and I will demonstrate that indeed only these adsorption positions are adopted by the molecules in this study, justifying the simple electrostatic approach taken here.

As OIB, OIBal and OIBca incorporate the same iodobenzene backbone, the molecular *adhesion* to the surface is expected to be very similar for all investigated molecules. The different functional groups contribute only marginally here, as will be confirmed later by the NC-AFM data. The functional groups will, however, influence the *cohesion* of the molecules on the surface as will be discussed individually for each molecule in the following sections.

6.2 OIB

Fig. 6.5 (a) shows the situation after the deposition of OIB on the calcite surface at room temperature (RT). I observe the formation of ordered single-layered island structures with an apparent height of about 3 Å. Considering the molecular dimensions, this height indicates that the molecules adsorb in a flat-lying manner on the surface.

Apart from islands, I also observe mobile molecular species which are only visible as streaks in the island-free areas on the surface. Apparently, well-ordered islands and mobile molecules that attach at and detach from island edges co-exist at RT. However, apart from cluster decorations on the island edges as shown in Fig. 6.5 (b), I never observe any second-layer growth. The absence of a second layer indicates the formation of a stable molecular wetting layer on the surface and sufficiently strong adhesion energy.

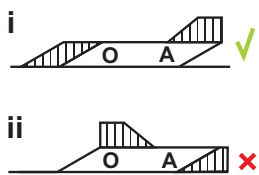


Figure 6.4: Adsorption behavior of OIB at the calcite step edges. **O** indicates the obtuse step edge, **A** is the acute step edge. The shaded areas indicate the OIB molecules.

As an interesting side effect, the islands are not distributed uniformly on the surface but show a preferred nucleation at certain calcite step edges. On the calcite(10.4) surface, two type of step edges exist, namely the obtuse and the acute step edges. Both have a monatomic height of about 3 Å, the same as the observed islands. Interestingly, there seems to be some sort of discrimination between these two edges. Molecular OIB islands only nucleate at the top of acute step edges or at the bottom of obtuse step edges (see Fig. 6.4). The inverse case, however, was never observed.

High-resolution NC-AFM imaging of single islands as depicted in Fig. 6.5 (b) reveals that the islands consist of bright rows that are arranged in two domains **I** and **II**. Upon closer investigation, it is found that the two domains constitute mirror-images of each other, each enclosing an angle of 50° with the substrate [42.1] direction, which acts as the mirror axis. The orientation of the bright rows in **I** is nearly parallel to the fast scanning direction of the AFM, making them hard to distinguish with the naked eye. However, when rotating the scan angle by 45° as shown in Fig. 6.6, the bright rows in **I** can unambiguously be identified.

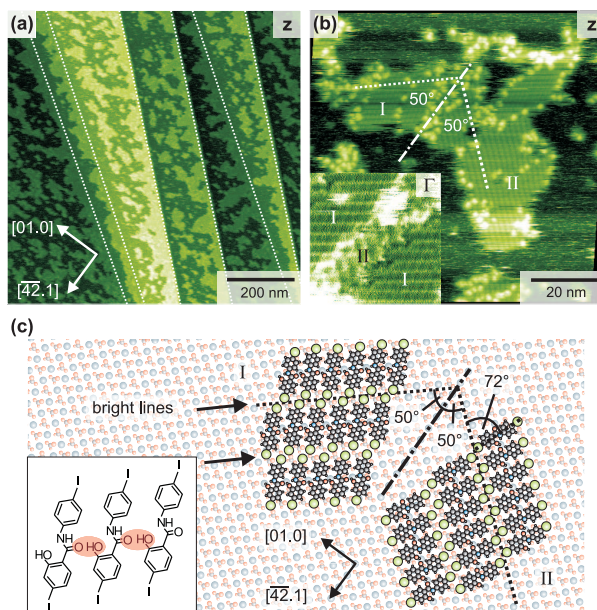


Figure 6.5: (a-b) NC-AFM topography (z) data of OIB on calcite(10.4) at RT. The dashed lines in (a) indicate step edges of the underlying calcite substrate. Mirrored domains in (b) are labeled **I** and **II**. Their main orientations are indicated by dashed lines, the mirror axis is given by the dash-dotted line. The image is corrected for linear drift. Inset of (b): Dissipation image revealing the row structure of domain **I**. The inset is magnified by a factor of two compared to (b). (c) Proposed molecular adsorption model. The hydrogen bond between two molecules is indicated by the shaded region in the inset.

Considering the fact that the molecules lie flat on the surface, I expect intermolecular hydrogen bond formation between the hydroxyl group and the carbonyl oxygen atom being the driving force for the molecular arrangement on the surface. This interaction results in the formation of rows of molecules aligned side-by-side. The bright rows in the two domains have a repeat distance of approx. 16 \AA , which is considerably smaller than the length of the molecule's main axis of 17.5 \AA . This finding indicates that the molecules' main axis forms an angle smaller than 90° with respect to the row direction. An excellent side-by-side alignment of the molecules at an angle of about 72° with respect

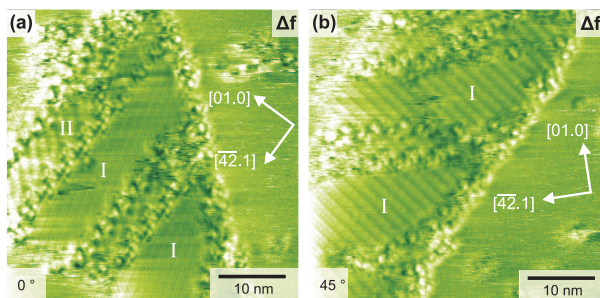


Figure 6.6: Influence of scan direction on the imaging of OIB islands. (a) Scanning parallel to the rows in **I**. Only the bright rows in **II** are clearly visible. (b) Rotation of the scan direction by 45°. The rows in **I** can clearly be seen now.

to the row direction is found as depicted in Fig. 6.5 (c). From this molecular alignment and the known directions of the underlying calcite crystal, I determine the angle of the molecule with respect to the $[\bar{4}2.1]$ direction to about 22°, which is in excellent agreement with the angle of 22.4° that is expected for the optimum adsorption position **1**. Thus, I conclude that the simple picture of electrostatic interaction between the iodine atoms and the surface calcium cations is, indeed, correct for the OIB backbone.

The existence of two distinct domains is readily explained by mirror-symmetric adsorption position. However, another property of the OIB molecule, namely its prochirality has to be considered as well. While OIB is achiral in the gas-phase, it becomes chiral upon its two-dimensional confinement to the sample surface. Fig. 6.7 shows several possibilities of arranging the OIB enantiomers into the two domains, based on the adsorption position as elaborated on above. Comparing different combinations and spatial arrangements of the enantiomers, it turns out that only for a homochiral domain the distance between the oxygen atoms involved in the hydrogen bond can be minimized to $d_{O-O} = 2.5 \text{ \AA}$ (upper left part of Fig. 6.7). Purely heterochiral arrangements result in conformations where the molecules have only one bonding partner at 2.5 Å distance, while the next neighboring molecule is farther away (lower left of Fig. 6.7). Analogously, it can be shown that one enantiomer only fits to one of

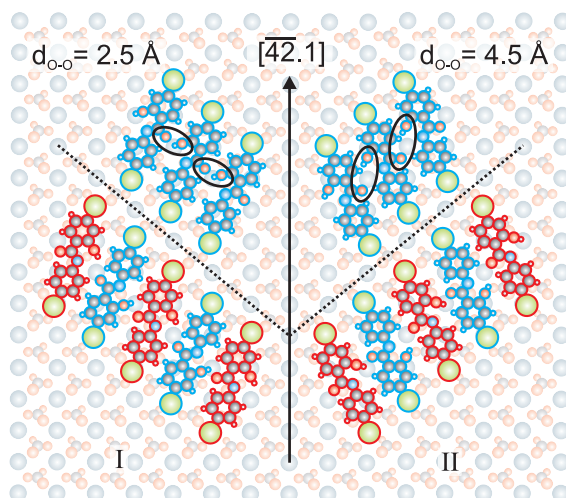


Figure 6.7: Influence of prochirality on the domain formation. OIB enantiomers are colored red and blue respectively. The oxygen-oxygen distance d_{O-O} applies to the hydrogen bonds between the blue colored molecules in the upper part of the image. The black ellipses mark the relevant hydrogen bonds.

the domains **I** or **II**. An example is shown in the upper right part of Fig. 6.7, where the enantiomer used for the construction of **I** is rotated to fit the orientation of **II**. This leads to an oxygen-oxygen distance of $d_{O-O} = 4.5 \text{ \AA}$ as opposed to 2.5 \AA when using the other enantiomer. Based on these considerations, I, therefore, assume that the domains **I** and **II** result from chiral separation of the OIB molecules.

Interestingly, the molecular islands can easily be destroyed during the scanning process. Depending on the interaction strength between tip and sample, islands are either removed during the acquisition of a single image or can be traced over a series of images before they are completely dissolved. The dissolution process always starts at the edges of the molecular islands where the molecules only have a single bonding partner as opposed to two partners inside the island. The energy needed to separate one molecule from the island edge is, thus, reduced at least by a factor of two compared to the binding strength inside the island.

Figure 6.8: (a-f) Consecutive AFM dissipation images of OIB on calcite(10.4) taken at RT. Acquisition time for each image is 500 s.

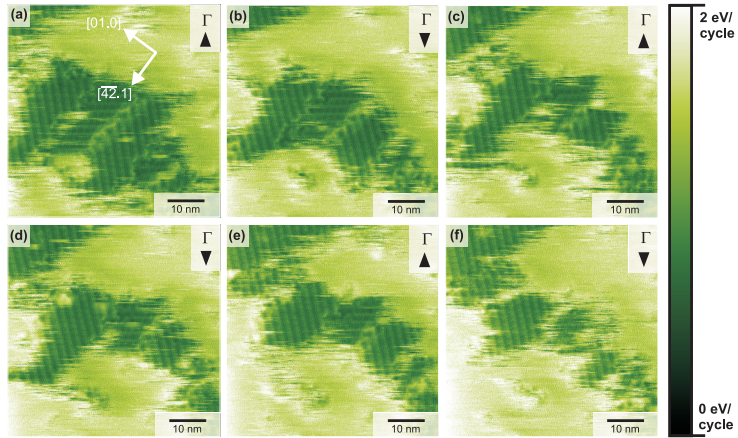


Fig. 6.8 shows a series of dissipation images, illustrating how a group of islands is slowly changing shape and dissolving during the scanning process. Dissipation images in AFM contain information about the energy that is needed to keep the cantilever oscillation stable. It is hence possible to calculate the energy dissipated in the sample during each scan cycle using the relation¹²³

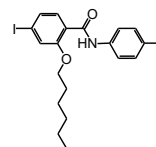
$$E_{ts} = \left(\frac{\Gamma}{\Gamma_0} - 1 \right) \cdot \frac{\pi k A^2}{Q} \quad (6.1)$$

where Γ is the dissipation energy at the point of interest and Γ_0 the energy dissipated in the unperturbed state. k , A and Q are the cantilever stiffness, oscillation amplitude and quality factor. For the sample shown here, the difference in dissipation energy between substrate and molecules is about 0.9 eV/cycle whereas the calculated binding energy for an oxygen-oxygen hydrogen bond is around 0.3 eV.¹²⁴ OIB molecules can, thus, be easily removed from the islands by scanning.

The relatively low cohesion of the molecules especially at the island edges is, of course, highly undesirable when considering application-relevant conditions. While a successful anchoring of the molecules via the iodine atoms could be achieved, *i.e.*, the molecular *adhesion* is sufficiently strong, the intermolecular *cohesion* appears to be too weak. I, therefore, vary the intermolecular interaction by using functionalized OIB derivatives.

6.3 OIBal

I will now discuss how the structure formation is influenced by adding an alkyl chain to the OIB backbone, resulting in OIBal. Fig. 6.9 (a) gives an overview image after depositing OIBal molecules onto the calcite(10.4) surface at RT. Very similar to OIB, islands of a height of 3 Å are formed, again indicating a flat-lying adsorption position. The island distribution on the sample surface is not even, but follows the same step edge nucleation scheme as described for OIB. In contrast to the structures formed by OIB however, I neither observe strike-artifacts due to mobile molecular species in addition to island structures, nor are the self-assembled islands decorated by clusters. This already indicates a stronger molecule-molecule interaction between OIBal on the surface.



A detailed analysis of images of the OIBal islands reveals the existence of two distinct domains **I** and **II** with a common orientation along the [01.0] direction of the underlying substrate (Fig. 6.9 b), while high-resolution images reveal an internal network structure of these domains (Fig. 6.9 c). The repeat distance along the common [01.0] orientation is (15 ± 1) Å in both domains, which is exactly three times the repeat distance of the underlying calcite surface in this direction. This clearly emphasizes the template effect of the calcite substrate due to the anchoring of the iodine to the surface calcium cations.

From the high-resolution image in Fig. 6.9 (c) a model can be extracted that confirms the favorable adsorption position **1** of the molecular backbone (Fig. 6.9 d) exactly as in the case of OIB (see Fig. 6.5 c). Due to the additional alkyl chain, however, the OIBal molecules are forced to arrange in a less dense packing compared to OIB.

As a result OIBal molecules form dimers connected *via* overlapping alkyl chains due to van-der-Waals interaction. Due to their very high flexibility, the interdigitated alkyl chains do not necessarily have to lie completely parallel to the surface, but could protrude from the surface. The dimers arrange along the calcite [01.0] direction as shown in the model in Fig. 6.9 (d). The back-to-back arrangement of the molecules is stabilized by the forma-

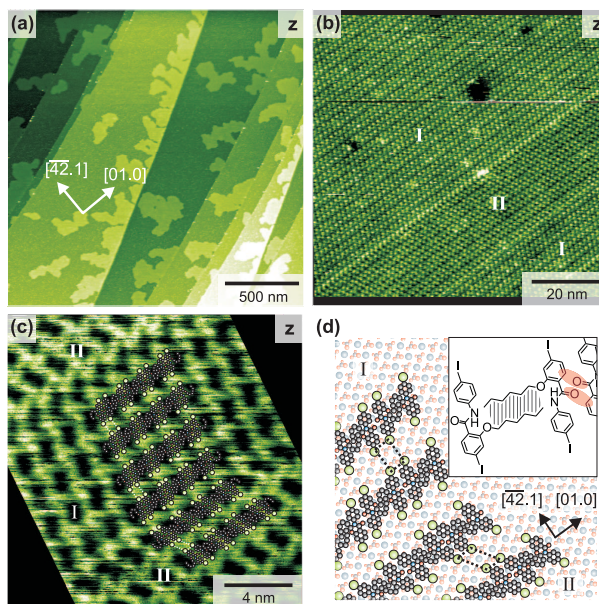


Figure 6.9: (a-c) NC-AFM topography (*z*) images of OIBal on calcite(10.4) at RT. Domains are labeled **I** and **II**. Images (b) and (c) are corrected for linear drift. (d) Proposed adsorption model. Hydrogen atoms are omitted for clarity. Translation of dimer rows along [01.0] causes two different arrangements of the row with respect to each other as indicated by the dashed connections of four iodine atoms in each domain. Inset: The hydrogen bonds between two OIBal dimers are indicated by the shaded regions, the van-der-Waals interaction between the alkyl chains is indicated by the dashed area.

tion of two hydrogen bonds between the carbonyl oxygen atoms and adjacent hydrogen atoms in the neighboring molecule. Note that this is different from OIB, where the side-by-side alignment was stabilized by only one hydrogen bond. For geometric reasons, OIB molecules cannot be in a back-to-back configuration that allows for two hydrogen bonds between each pair of molecules because void regions would be created. OIBal molecules, in contrast, can arrange at a distance that allows for the formation of two hydrogen bonds in the back-to-back configuration since the alkyl chains serve as the necessary spacers that bridge these voids (see inset of Fig. 6.9 d). The required area per OIBal molecule is 152 \AA^2 compared to 101 \AA^2 for OIB.

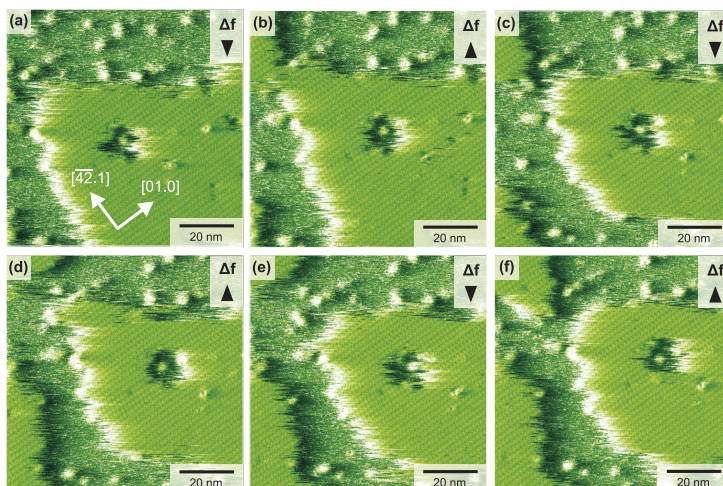


Figure 6.10: (a-f) Series of frequency shift images obtained for OIBal. Apart from slowly changing borders, the islands remain intact upon scanning. Acquisition time for each image is 500 s.

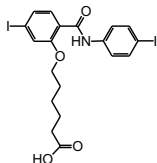
The dimer rows in both OIBal domains have a common orientation along $[01.0]$ and a row distance of $(20 \pm 1)\text{\AA}$. The adsorption position is mirror symmetric to the substrate $[\overline{42}.1]$ direction which readily explains the existence of the two domains. Additionally, two neighboring rows can be shifted with respect to each other, resulting in two possible arrangements as shown in Fig. 6.9 (d). In domain **I**, the dimer rows along $[01.0]$ are oriented with four neighboring iodine lying on the corner of a rectangle. However, it is also possible to translate the dimer rows along the substrate $[01.0]$ direction to the next calcium ion as shown for domain **II** in the model. Now, the neighboring iodine atoms form a sheared rectangle, which leads to an overall different orientation towards the $[\overline{42}.1]$ direction as compared to **I**. As this translation is possible for every new dimer row along $[01.0]$, frequent domain transitions and varying domain orientations are observed.

The OIBal islands appear more stable than those formed by OIB molecules, as only slight rearrangements of the island edges are observed. This finding corroborates the above made statement of a stronger molecule-molecule interaction on the surface in the case of OIBal as compared to OIB. Even at tip-sample interactions larger than typical imaging conditions, it was not possible to deliberately destroy the OIBal islands by scanning (Fig. 6.10).

This is in sharp contrast to what was observed for OIB, where the low intermolecular cohesion is heavily interfering with the acquisition of high-resolution images. This higher cohesion can be explained by the aforementioned interdigitation of the alkyl chains. It has been shown that the van der Waals interaction between two alkyl chains is in the order of 0.08 eV per pair of interacting CH₂ units, resulting in a total binding energy of about 0.5 eV in the case of two interacting hexyl chains in an OIBal dimer.^{125,126} The interaction due to overlapping hexyl chains is considerably larger than the single hydrogen (~0.3 eV) bond between two OIB molecules, which is in excellent agreement with the experimental observation of less stable islands in the case of OIB. Thus, by comparing these results of OIBal with those of OIB, it can be concluded that while *adhesion* to the surface is very similar for both molecules, their *cohesion* differs significantly.

Functionalization of OIB with an alkyl chain of sufficient length changed the type and strength of the molecular interaction, switching from a single hydrogen bond connecting two OIB molecules to van-der-Waals interaction and double hydrogen bonding for OIBal. The adjustment of the molecule design has a significant influence on the molecular structure formation, resulting in a distinct change in island morphology, density and relative orientation of the molecules within the islands, despite the fact that the molecular adsorption position with respect to the underlying calcite substrate remained unchanged.

6.4 OIBca



Introducing a carboxylic acid group at the end of the OIBal alkyl chain yields the molecule OIBca, again changing the interaction between two molecules on the surface. For this molecule, dimerization *via* the formation of hydrogen bonds between two carboxylic acid groups should be favorable. Since both C=O...H-O hydrogen bonds have a binding strength of about 0.3 eV,¹²⁴ this dimer connection should be even stronger than the overlapping alkyl chains within an OIBal dimer.

Fig. 6.11 (a) shows the molecular structures that are formed af-

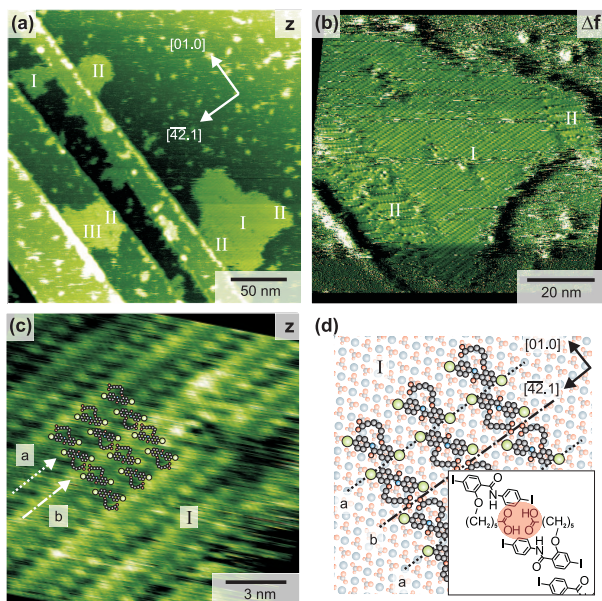


Figure 6.11: (a-c) NC-AFM topography (z) and frequency shift (Δf) images of OIBca on calcite(10.4) at RT. Three different domains are labeled **I-III**. (b) Detailed image revealing the internal structure of domains **I** and **II**. (c) Detailed image showing a domain **I** area. Images (b) to (c) are corrected for linear drift. The corrugated rows are marked with a dashed arrow, the blurry rows with a dash-dotted arrow. (d) Adsorption model for OIBca in position **2**. Inset: The carboxylic acid dimer is indicated by a shaded ellipse.

ter deposition of OIBca on the calcite(10.4) surface held at RT. Ordered island structures with a height of about 3 \AA form and co-exist with mobile molecular species similar to the situation found after OIB deposition. In contrast to OIB however, no decoration of the islands is observed. While the molecular islands are again nucleating at the calcite step edges, no step edge discrimination as was found for OIB and OIBal is observed here. High-resolution images reveal the existence of at least three different domains **I - III** on the surface (Fig. 6.11 a and b). The molecular rows in **I** are oriented parallel to the substrate $[\bar{4}2.1]$ direction, whereas the rows in domains **II** and **III** enclose an angle of $\pm 29^\circ$ and $\pm 34^\circ$ with that direction, respectively. In contrast to OIB, the different domains are not mirror images of each

other. The co-existence of different domain structures indicates competing intermolecular interaction types of similar interaction strength. This is different from the well-defined configurations revealed for OIB and OIBal. However, despite the fact that different structures are obtained, the OIBca structures are revealed to follow the crystallographic directions of the substrate, indicating the strong substrate templating effect.

In contrast to OIB and OIBal, OIBca presumably forms stable dimers that are connected at the end of two flexible alkyl chains, altogether resulting in much more flexible and space-consuming dimer units. This readily explains the structural complexity in the case of OIBca, but at the same time precludes me from drawing a simple adsorption model for all configurations that are observed. I will, therefore, only exemplarily discuss a possible structural arrangement of OIBca molecules in domain **I**.

Fig. 6.11 (c) shows a high-resolution image of domain **I**, revealing its inner structure. Two alternating row types, running parallel to the $[\overline{4}2.1]$ direction are observed within the domain. Every second row has a clearly discernible corrugation with a periodicity of $(7.8 \pm 0.5) \text{ \AA}$ along $[\overline{4}2.1]$, precisely matching the calcite repeat distance in that direction (**a**-type row). In contrast, every other row appears somewhat blurry (**b**-type row). A model for domain **I** is given in Fig. 6.11 (d). The corrugation in the type **a** rows is readily reproduced by OIBca dimers and the equidistant spots can be assigned to the molecule's iodine atoms occupying adsorption sites above calcium cations. While the molecular backbone is firmly anchored to the surface, the alkyl chains connecting the dimers are still flexible enough likely leading to the blurry **b**-type rows. The molecular orientation on the substrate matches that of the favorable adsorption position **2** presented in Fig. 6.3. Thus, domain **I** confirms the favorable adsorption motif that was found for OIB and OIBal.

The images obtained for OIBca demonstrate that adding a flexible intermolecular linker results in yet another molecular arrangement. In good agreement with the flexibility of the linker, coexisting equivalent structures are revealed that are governed by the intermolecular cohesion, while the adhesion mechanism to the surface is unaffected by the change in functionalization.

6.5 Further Iodobenzene Systems

The observations made for the OIB-based molecules clearly demonstrate a significant electrostatic anchoring of the molecules towards the surface, while at the same time the flexibility to fine-tune the resulting structure by adjusting the intermolecular cohesion is maintained. These findings are, of course, not limited to the molecules discussed above, but can be used to rationally design new molecules for use in self-assembly processes. To demonstrate this as a short, yet straight-forward example, a third benzene unit is added to the OIB backbone, resulting in a molecular structure as shown in Fig. 6.12 (a).

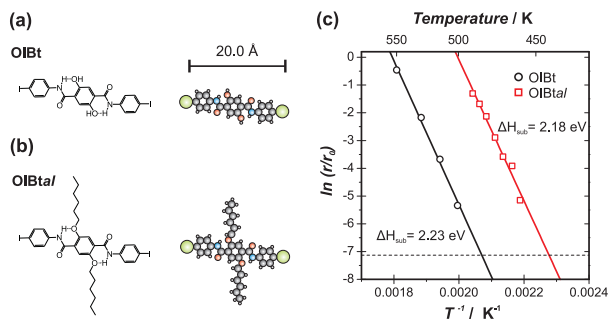


Figure 6.12: (a) Skeleton and ball models for OIBt and OIBtal. (b) Arrhenius plots for OIBt and OIBtal including sublimation enthalpies. The dashed line indicates the resolution limit of the setup.

In comparison to OIB, the center-to-center distance between the opposing iodine atoms is increased to 20.0 Å. To indicate this third benzene unit the new backbone will be called *oligo iodo benzamide trimer* (OIBt). This new, expanded structure does not alter the iodine anchoring mechanism to the surface, but allows, e.g., for the addition of two alkyl chains, yielding OIBtal (Fig. 6.12 b), which offers interdigitation possibilities on both sides of the molecule.

Sublimation experiments yield a sublimation enthalpy of $\Delta H_{sub} \approx (2.2 \pm 0.1) \text{ eV}$ for both molecules (Fig. 6.12 c). I, therefore, assume that their interaction in the bulk is of similar strength. This is also in good agreement with the intermolecular interaction

mechanisms as will be described below.

Possible adsorption positions on calcite(10.4) are determined analogously to OIB by drawing a circle of 20 Å radius (*i.e.* the I-I distance in the OIBt molecule) around a surface calcium cation. The three best matches of Ca-Ca and I-I distance are drawn in Fig. 6.13 while Tab. 6.2 summarizes distances and orientations for those three adsorption positions.

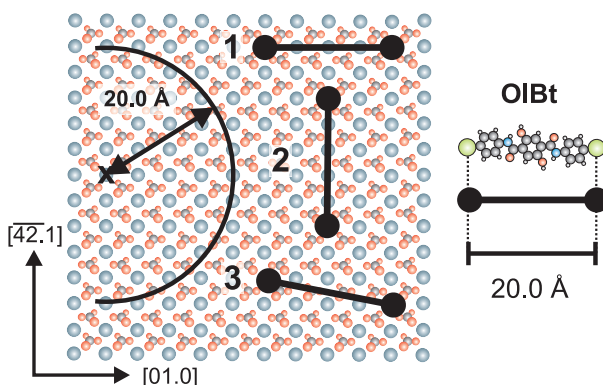


Figure 6.13: Determination of preferable adsorption positions for OIBt on calcite(10.4) analogously to OIB. The black discs represent the iodine atoms with their covalent diameter. The three configurations that provide the best match of the distances between the molecule's iodine and the substrate's calcium atoms are drawn. For angles and distances see Tab. 6.2.

Pos.	Orientation towards $[\overline{42}.1]$	Ca-Ca distance	Dev. from I-I distance
1	90.0°	20.0 Å	0 Å
2	0°	20.3 Å	0.3 Å
3	78.6°	20.4 Å	0.4 Å

Table 6.2: Orientations and calcium-calcium distances for OIBt on calcite(10.4) as drawn in Fig. 6.13

Based on the observations made for the oligo iodo benzamides as discussed in sections 6.2-6.4, I expect the formation of two

hydrogen bonds between the molecules in the case of the backbone OIBt (Fig. 6.14 a). The strength of these hydrogen bonds is about 0.3 eV each,¹²⁴ resulting in a net bonding strength of about 0.6 eV between two OIBt molecules. At the same time, this rather rigid molecular formation severely limits the possibility of adopting one of the favorable adsorption positions depicted in Fig. 6.13 that would enable electrostatic interaction between iodine and calcium. Assuming a typical distance of about 2.5 Å for the atoms involved in the hydrogen bond,¹²⁴ it can be shown that, using the model described above, it is not possible to position two bound OIBt molecules on the calcite surface such as that all four iodine atoms are placed on top of surface calcium cations. I, therefore, expect the formation of molecular clusters instead of wire-like structures for OIBt. In the case of OIBtal, the interaction strength between two interdigitated alkyl chains is about 0.5 eV (see section 6.3), close to the 0.6 eV for two bound OIBt molecules. However, the flexibility of the alkyl chains allows for easily positioning bound OIBtal molecules in one of the favorable adsorption positions and I expect the formation of extended, wire-like structure for OIBtal (Fig. 6.14 b).

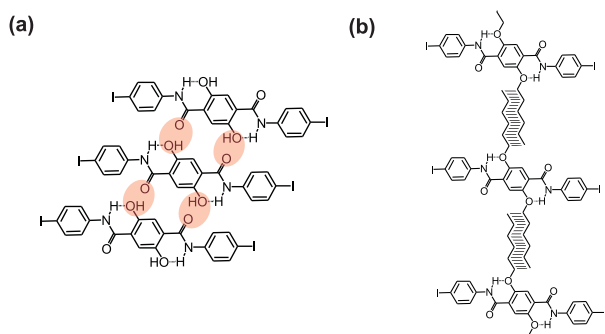


Figure 6.14: Proposed interaction mechanisms for OIBt and OIBtal. (a) The hydrogen bonds between two OIBt molecules are indicated by the shaded regions. (b) The van-der-Waals interaction between the alkyl chains is indicated by the dashed area.

Fig. 6.15 shows the situation after deposition of OIBt and OIBtal on pristine calcite(10.4) samples. Deposition of OIBt (Fig. 6.15 a) leads to the formation of molecular clusters. This was expected from the interaction considerations made above, so I omit drawing a detailed adsorption model for OIBt.

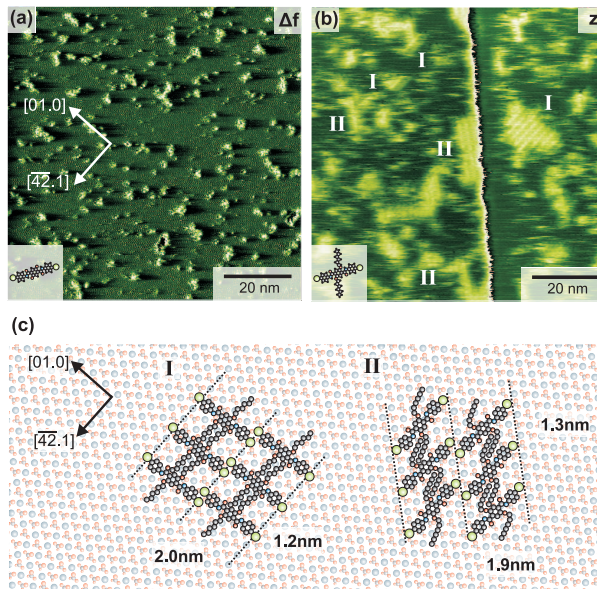


Figure 6.15: (a) Frequency shift image of molecular clusters formed by OIBt upon deposition on calcite(10.4). (b) Topography image of typical structures formed upon deposition of OIBtal. A double color scale is used here for better visualization. (c) Suggested adsorption models for the observed molecular orientations I and II of OIBtal. Hydrogen atoms are omitted for clarity. Alkyl chains are interdigitated, similar to OIBal.

For OIBtal, the formation of molecular islands and clusters is observed (Fig. 6.15 b). At smaller scales, however, two kinds of row structures are identified. The first one has an orientation of $\pm 50^\circ$ to the calcite [42.1] direction with a row separation of $(20 \pm 1) \text{ \AA}$ (Structure I). Additionally, I observe a second orientation that is aligned along the [42.1] direction (structure II), with a row separation of $(19 \pm 1) \text{ \AA}$.

In contrast to OIBal as described in section 6.3, OIBtal offers two possibilities for the alkyl chains to interdigitate, thus favoring the formation of extended rows. Structures identified as islands here are, thus, most probably agglomerated molecular rows. This row-formation also explains why the formation of extended molecular islands that was, even at low coverages, favored for OIBal, is not observed here. From analyzing several

high-resolution images, models for both structures can be drawn as shown in 6.15 (c) that are based on the two best matches **1** and **2** as obtained from Fig. 6.13.

For orientation **I**, the molecule's main axis is oriented perpendicular to the calcite $[\bar{4}2.1]$ direction, matching the calculated angle of 90° for adsorption position **1**. Analogously, adsorption position **2** matches well the observations made for orientation **II**. The alkyl chains on both sides of OIB tal can interdigitate with those of neighboring molecules, resulting in the extended row structures that are observed. Due to their high flexibility, this is possible in both orientations **I** and **II**. The mechanism of interdigitation is similar to what was observed for the formation of OIB al dimers. Though some of the molecules are still mobile on the surface, as indicated by streaks in the acquired images, it was not possible to deliberately destroy the molecular structures as in the case of OIB, indicating a high molecular cohesion. Altogether, this short example demonstrates, that the insights gained from the investigation of the OIB-based molecules discussed before can be transferred to other systems as well.

6.6 Conclusions

I demonstrate the systematic variation of molecular cohesion for a set of molecules with identical adhesion to an insulating substrate. To achieve this, the functionalization of shape-persistent oligo(*p*-benzamide)s was engineered by introducing different functional groups and investigating their effect on the structural formation on the insulating calcite(10.4) surface. The molecular core was designed to provide significant electrostatic anchoring towards the surface, while at the same time maintaining the flexibility to fine-tune the resulting structure by adjusting the intermolecular cohesion energy.

The success of this strategy is based on a clear separation of the molecule-substrate interaction from the molecule-molecule interaction. I compare a total of five rationally designed molecules based on closely related molecular building blocks. Four of these molecules adopt a well-defined adsorption position that

is governed by the same iodine-calcium interaction motif, indicating the strength of the iodine anchor. Despite the identical adsorption mechanism, distinctly different molecular structures could be achieved by changing the molecule functionalization. The different functionalizations encode a change in the orientation of the molecules with respect to each other and, thus, result in entirely different self-assembled structures.

My results show that sufficient molecule-surface anchoring can be achieved without restricting the structural flexibility that is needed for the design of complex molecular systems.

7 Terephthalic Acids

Contents

7.1 Introduction	74
7.2 2-ATPA	76
7.3 2-BrTPA	83
7.4 2-Br-5-PATPA	88
7.5 Conclusions	92

MOLECULAR functionalization proves to be a valuable tool to control the structure formation in molecular self-assembly as was shown in the last chapter. Here, I will present the investigation of several derivatives of terephthalic acid. In contrast to the oligo iodo benzamides, the structural changes made here resulted in a different anchoring of the molecular building blocks to the surface, decisively influencing the structure and stability of the self-assembled arrangements.

Automated electron diffraction tomography investigations for two of the molecules were kindly performed by [REDACTED] through a collaboration with the group of [REDACTED]¹²⁷ Parts of the measurements presented for the 2-BrTPA molecule were conducted by my colleague [REDACTED]

7.1 Introduction

Terephthalic acid (TPA, benzene-1,4-dicarboxylic acid) and its derivatives are of broad interest for a range of applications. They are especially valued for their suitability as linkers in the preparation of coordination polymers and metal-organic frameworks (MOFs).¹²⁸ Applications range from MOFs whose porosity allows for efficient gas adsorption^{129,130} to the use of TPA derivatives in the dye industry.¹³¹ It is, therefore, of great interest to investigate their properties as building blocks in molecular self-assembly.

Previous experiments involving TPA adsorption on the calcite(10.4) surface have shown that the TPA molecules are very mobile on the surface at room temperature.³⁶ This has hindered the high-resolution imaging with AFM which could only be achieved by performing the measurements at coverages that were at least one monolayer. That way, the TPA molecules in the first monolayer are stabilized and high-resolution AFM measurements can be performed. For many application-relevant structures, however, it is desirable to create stable structures at sub-monolayer coverages.

I, therefore, chose various derivatives of TPA and investigated the influence of the additional functional groups on the structure formation and stability upon deposition on calcite(10.4). As the structure formation of the TPA backbone on the calcite surface is already known, the observed differences can directly be related to those functional groups.

The molecules investigated in this chapter are shown in Fig. 7.1 a - c. By adding an amino group to TPA at position 2 the molecule 2-aminoterephthalic acid (2-ATPA) is obtained. The hydrogen atoms of the amino group should enable hydrogen bonding to the substrate carbonate groups, thus stabilizing the 2-ATPA molecules on the calcite surface. In the case of 2-bromoterephthalic acid (2-BrTPA), the amino group in 2-ATPA is replaced by a bromine atom, thus changing the interaction mechanism with the calcite surface. In analogy to the successful anchoring of oligo iodo benzamides as presented in chapter 6, the electronegative bromine

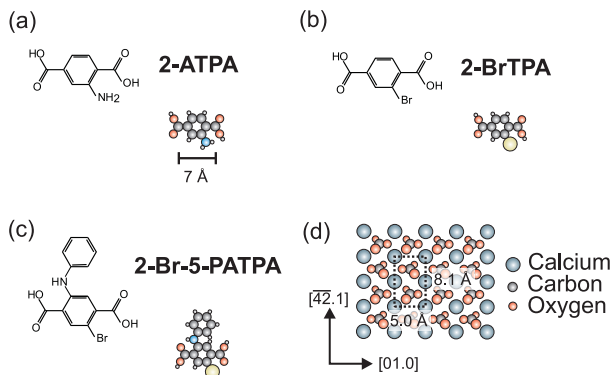


Figure 7.1: (a-c) Skeleton formulas and ball models of the TPA derivatives investigated in this study. (d) Model of the calcite(10.4) surface drawn to scale.

Molecule	Purity	pK_a	ΔH_{sub} [eV]
2-ATPA	99%	3.58 ¹³²	(1.67 ± 0.09)
2-BrTPA	95%	2.21 ¹³³	(1.67 ± 0.16)
2-Br-5-PATPA	n.a.	n.a.	(0.88 ± 0.24)

Table 7.1: Purity, acid dissociation constant (pK_a) and sublimation enthalpy (ΔH_{sub}) of the TPA derivatives investigated here. The latter were obtained from sublimation experiments using a QCM setup. 2-Br-5-PATPA was purchased from the Sigma-Aldrich rare chemical library CPR. Therefore, no further analytical data were available for this molecule.

should act as an electrostatic anchor by interacting with a positively charged surface calcium cation. The third investigated molecule is 2-bromo-5-(phenylamino)terephthalic acid (2-Br-5-PATPA), which is obtained by adding a phenylamine to 2-BrTPA at position 5. Similar as for 2-BrTPA, the bromine is expected to interact with the surface calcium cation while, at the same time, the formation of a N-H...O hydrogen bond between molecule and surface should be possible. In addition, it is of interest to investigate how the comparatively large phenylamine affects the structure formation of 2-Br-5-PATPA in comparison to the smaller 2-ATPA and 2-BrTPA molecules.

7.2 2-ATPA

Fig. 7.2 a shows the situation after the deposition of 2-ATPA on the substrate at RT. The coverage here is < 0.1 monolayer (ML). Straight lines are observed, that run strictly parallel to the substrate $[01.0]$ direction. Their apparent height was determined to about 1.4 \AA with respect to the substrate. For a flat-lying molecule, however, a height of about 3 \AA would be expected as has also been reported for TPA on calcite(10.4).^{107,134} This height difference is probably the result of additional electrostatic interactions between tip and sample that arise during the measurement.⁹⁵ While the height measurements here are obviously biased, a flat-lying adsorption geometry is assumed for 2-ATPA as will be further corroborated by the following analysis.

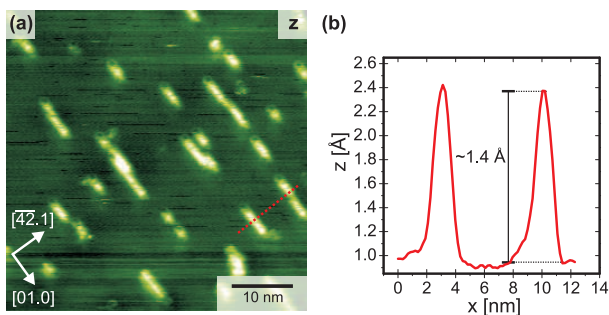


Figure 7.2: (a) Topography image of 2-ATPA on calcite(10.4) at coverage < 0.1 ML. (b) Height profile along the dashed line drawn in (a). The apparent height is about 1.4 \AA .

The molecular rows are distributed evenly over the sample surface and do not nucleate at the calcite step edges. The same adsorption behavior is observed when preparing samples with higher coverage as shown in Fig. 7.3. At that coverage, the molecular rows assemble into narrow, elongated islands, still keeping the strict $[01.0]$ orientation. High-resolution images (Fig. 7.3 c) reveal the inner structure of these islands. Careful analysis of several drift-corrected images yields an inner corrugation of the rows of $(10 \pm 1) \text{ \AA}$ along the $[01.0]$ direction, exactly matching the double repeat distance of the substrate in

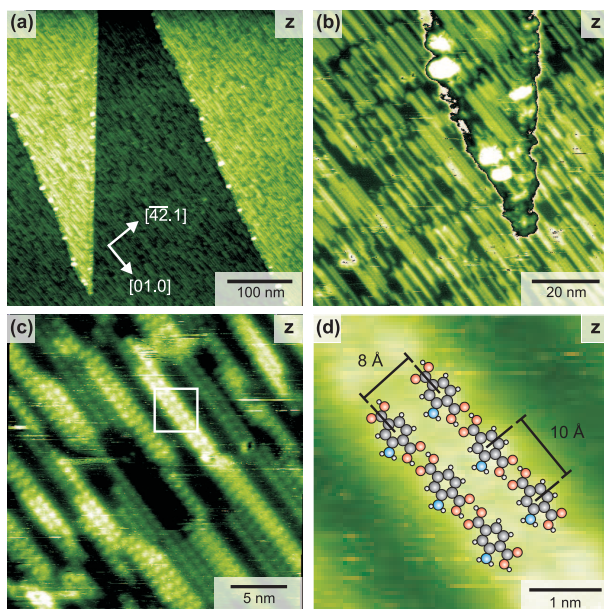


Figure 7.3: (a) Increased coverage of 2-ATPA on calcite(10.4). (b,c) Detailed images of the formed structures. (c) is corrected for linear drift. (d) Structural motif for the area marked in (c).

this direction. Given the molecules' dimensions, I assign each bright feature to a single 2-ATPA molecule (Fig. 7.3 d). Rows along [01.0] with the same repeat distance were also observed for unfunctionalized TPA where the molecular rows are formed by consecutive flat-lying TPA molecules that are linked by their respective carboxylic acid endgroups as is suggested by the TPA crystal structure.¹³⁵ This is also in good accordance with the observations made for TPA superstructures on different metal surfaces.^{136–138} Taking into account the striking similarity of TPA and 2-ATPA in repeat distance and row orientation I, therefore, conclude that the mechanism responsible for the row formation is the same for both molecules (Fig. 7.3 d).

Every two 2-ATPA rows are equally spaced with a repeat distance of $(8 \pm 1) \text{ \AA}$. This is in sharp contrast to the structure formation that has been observed for TPA. There, the molecular rows are not equally spaced but two neighboring rows each have

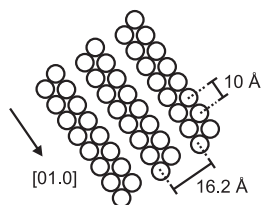


Figure 7.4: Schematic representation of the TPA ribbon structure formed on calcite(10.4). Each circle represents a single TPA molecule.

been found to be positioned closer to each other than the following row. This leads to molecular ribbons as depicted in Fig. 7.4 and resulted in an overall (2×2) superstructure.

Further increasing the coverage of 2-ATPA to > 1 ML leads to the formation of stable ad-layers on top of the first layer (Fig. 7.5 a). In contrast to the first layer, the molecular rows in this ad-layer are displaced by about 2.5 \AA along $[01.0]$ with respect to each other, leading to a zig-zag structure as shown in the high-resolution image in Fig. 7.5 b. The periodicity along $[01.0]$ remains at $(10 \pm 1) \text{ \AA}$, whereas the row separation is $(12 \pm 1) \text{ \AA}$. This leads to an overall (2×3) superstructure of the 2-ATPA ad-layer. The (2×1) structural motif of the underlying first layer is imaged simultaneously, displaying a perfectly ordered structure at monolayer coverage.

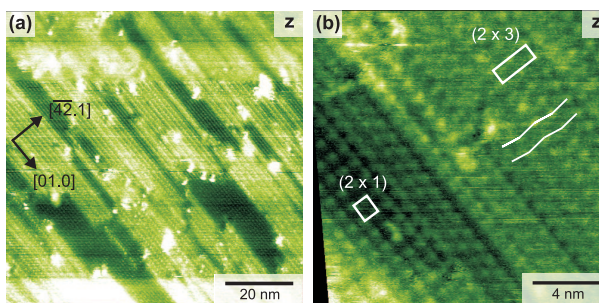


Figure 7.5: (a) 2-ATPA at coverage > 1 ML. (b) High-resolution image of (a). The unit cell of the closed monolayer and the ad-layer are indicated. Rows are displaced by 2.5 \AA along $[01.0]$ in the ad-layer (zig-zag lines). The image is corrected for thermal drift.

A striking difference between TPA and 2-ATPA self-assembly is found when observing 2-ATPA structures for several scan cycles. Fig. 7.6 shows a series of consecutive topography images of 2-ATPA islands. By comparing these images, it can be seen that the island reorganization at RT is negligibly small as only single bright spots associated with molecules are changing place. This clearly demonstrates the stability of the 2-ATPA structures on the calcite surface and is in sharp contrast to the observations made for unsubstituted TPA, where extensive reorganization of the island borders was observed under similar imaging

conditions. A stable structure for TPA could only be achieved by depositing at least one monolayer of molecules.

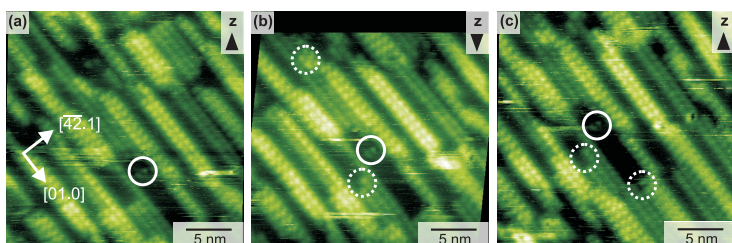


Figure 7.6: (a-c) Consecutive topography images of 2-ATPA islands. The solid circle indicates a reference point while the dashed circles illustrate changes with respect to the previous image. Nearly no reorganization of the island borders takes place, demonstrating the stability of the formed structures. Acquisition time for each image is 500 s, the images are corrected for linear drift.

As TPA and 2-ATPA share the same aromatic backbone and, upon deposition on calcite, form similar rows oriented along $[01.0]$, this change in stability has to be attributed to the additional amino group of 2-ATPA compared to TPA. This amino group offers the possibility of hydrogen bonds to the surface carbonate groups, thus anchoring the 2-ATPA molecules to the substrate.

Together with the high-resolution images in Fig. 7.3, an adsorption model for 2-ATPA on calcite(10.4) can be drawn that reproduces the observed structures (Fig. 7.7). Hydrogen bonds are formed between opposing COOH groups of two 2-ATPA molecules, leading to the aforementioned row formation. As mentioned earlier, the mechanism responsible for the row formation along the substrate $[01.0]$ direction should be the same for TPA and 2-ATPA. Additionally, the strict $[01.0]$ orientation that is observed supports the notion of a strong substrate templating effect. This is further corroborated by the measured repeat distance of 10 \AA along $[01.0]$, which is exactly two times the surface unit cell repeat distance along this direction. This periodicity allows to place the molecular rows such as that each amino group is positioned on top of a surface carbonate group. This enables the formation of additional hydrogen bonds between molecules and surface, thus further stabilizing the molecular arrangement.

In the case of unfunctionalized TPA, the substrate causes an enlargement of the hydrogen bond length in comparison to the TPA bulk structure.³⁶ Apart from that, the observed row formation is in good agreement with the crystal structure. For 2-ATPA, however, the substrate templating effect is far more pronounced. Automated electron diffraction tomography (ADT)^{139,140} investi-

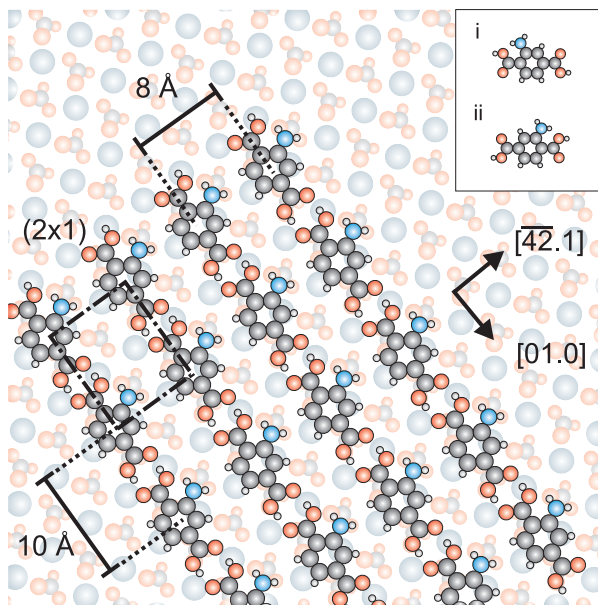


Figure 7.7: Adsorption model for 2-ATPA on calcite(10.4). The amino group serves as anchor by forming two hydrogen bonds with a surface carbonate group. Inset: Enantiomers of 2-ATPA. The model is drawn for enantiomer **i**.

gations that were performed in the course of this study showed that, for 2-ATPA, stacked layers are formed in the bulk,¹²⁷ in contrast to the chain formation in the TPA bulk structure.¹³⁵ These layers are most probably formed due to the additional linking possibilities to other 2-ATPA molecules that are provided through the amino group. Upon adsorption onto the calcite surface, however, this amino group can interact with a surface carbonate group instead of a neighboring molecule, thus leading to the formation of row structures instead of extended network or layer structures. As already discussed in chapter 2, this distinct difference between bulk and surface structure formation clearly emphasizes the strength of the substrate templating effect.

In comparison to TPA, the symmetry of 2-ATPA is reduced through the introduction of the additional amino group and the molecule becomes prochiral. This prochirality leads to two different ad-

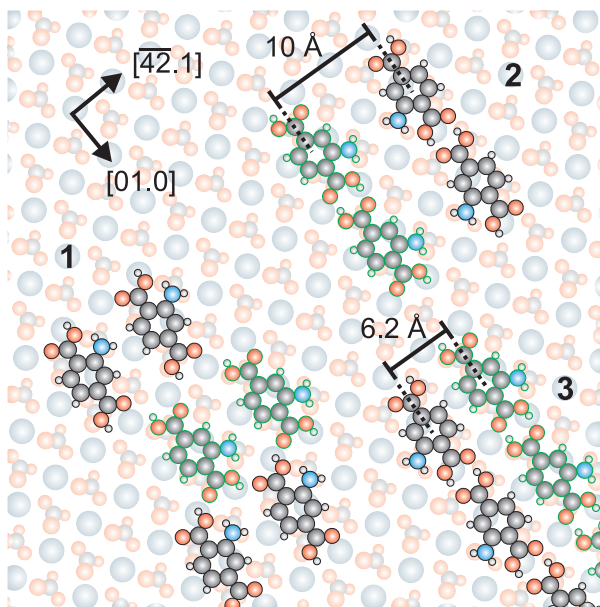


Figure 7.8: Effects of prochirality on structure formation. Enantiomer **ii** is displayed in a different color for better visibility. The construction of heterochiral rows (**1**) would lead to displacements along $[01.0]$. Additionally, the molecules are not equidistant anymore. Heterochiral islands would exhibit repeat distances along $[42.1]$ that are either bigger (**2**) or smaller (**3**) than obtained from the measurements.

sorption possibilities on the calcite(10.4) surface (enantiomers as shown in the inset of Fig. 7.7), which are, in principle, both in agreement with the observed repeat distances. Nonetheless, when keeping the same adsorption position for the amino group on the surface, heterochiral rows would inevitably lead to a displacement inside the molecular rows as shown in Fig. 7.8, **1**. Such a displacement, however, was never observed during the measurements. Thus, I assume the existence of heterochiral rows to be unlikely. The same geometrical reasoning leads to the conclusion that the 2-ATPA islands as well are purely homochiral as, for islands that are formed by homochiral rows composed of different enantiomers, the repeat distances would not fit those that are obtained from the measurements (Fig. 7.8, **2** and **3**). The prochirality of 2-ATPA, however, dictates that a racemic

mixture is deposited and, therefore, two types of homochiral islands have to be formed on the sample surface.

As an additional effect, the described adsorption mechanism would allow for shifting each 2-ATPA row by 5 \AA , thus leading to a displacement of neighboring rows. Still, this was never observed during the measurements, indicating that an additional weak interaction exists between two neighboring rows. This is further corroborated by the fact that, even at monolayer coverages, only perfectly ordered structures without displacements were observed.

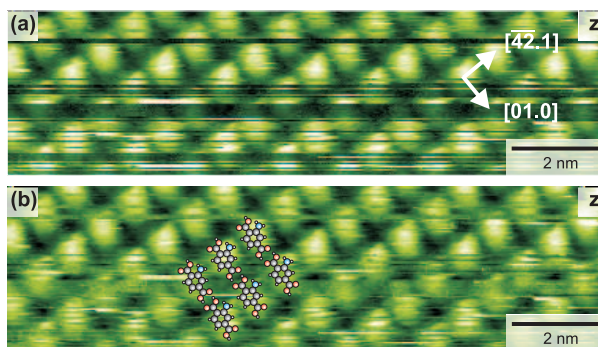


Figure 7.9: High-resolution topography image taken at monolayer coverage of 2-ATPA. The bright spots are imaged with an asymmetry pointing towards the upper border of the image. (a) Shows the raw data while in (b) a line-by-line subtraction was applied to enhance visibility.

Fig. 7.9 shows a high-resolution topography image of 2-ATPA at monolayer coverage. In this image, the bright spots are not imaged as perfectly round discs but exhibit a clear asymmetry pointing towards the upper border of the image. Superimposing the structural model from Fig. 7.7 suggests that this asymmetry can be attributed to the amino group of 2-ATPA (Fig. 7.9 b) and supports the assumption of purely homochiral islands made before. However, while an imaging artifact caused by the AFM feedback loops can be ruled out by comparing different scan directions, a tip-induced imaging artifact cannot be completely excluded. Yet, a similar asymmetry effect is observed for 2-BrTPA as will be described in the following section.

The addition of an amino group to TPA successfully stabilized the molecular arrangement on the calcite surface at sub-monolayer coverage while the strong substrate templating effect causes the formation of rows which is distinctively different from the bulk structure. In the following section, I will discuss how the self-assembly process is influenced by replacing the amino group by a bromine atom.

7.3 2-BrTPA

In the case of 2-BrTPA, hydrogen bonding to the surface carbonate groups as described for 2-ATPA is not possible anymore. Instead, the electronegative bromine should be able to interact with a surface calcium cation, similar to the electrostatic anchoring described in chapter 6.

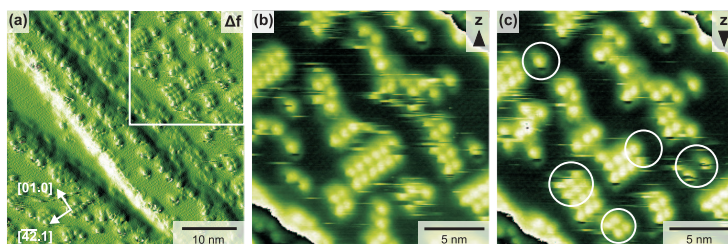


Figure 7.10: (a) Frequency shift image of 2-BrTPA on calcite(10.4). (b,c) Consecutive topography images of 2-BrTPA from the marked area in (a). Mobility of the molecules is indicated by the white circles. The black arrows give the slow scan direction.

Fig. 7.10 a shows 2-BrTPA molecules deposited on a pristine calcite(10.4) surface at RT. The molecules assemble into preferentially rectangular arrangements that are, apart from some decoration of the acute calcite step edges, distributed evenly over the sample surface. This is different from what was observed for TPA and 2-ATPA, where elongated rows along the substrate [01.0] are the favored adsorption motif. Comparison of consecutive topography images (Fig. 7.10 b,c) shows that the observed structures are frequently rearranged, indicating a higher molecular mobility of 2-BrTPA on the calcite surface than was observed for 2-ATPA under similar conditions.

High-resolution images of 2-BrTPA at sub-monolayer coverage (Fig. 7.10) reveal a repeat distance of $(10.0 \pm 0.5) \text{ \AA}$ along the

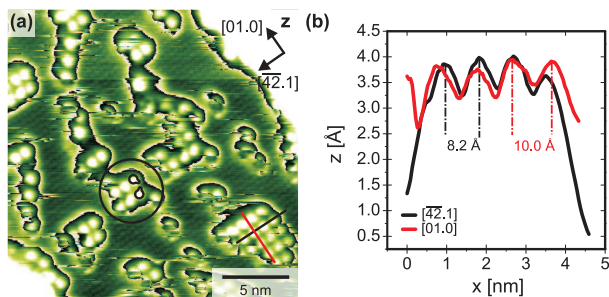


Figure 7.11: (a) High-resolution topography image of 2-BrTPA structures. A double color scale is used for better visibility. Note that the substrate is imaged simultaneously, giving an inherent lateral length scale. (b) Height profiles along the lines indicated in (a).

substrate $[01.0]$ direction and $(8.2 \pm 0.5) \text{ \AA}$ along $[\overline{42}.1]$, exactly matching the (2×1) reconstructed unit cell of the underlying calcite substrate. The height of the observed islands is determined to about 3 \AA , indicating a flat-lying adsorption position.¹³⁴ Similar to the observations made for 2-ATPA, the bright spots in the topography image are not perfectly round but exhibit a slight asymmetry that is observed in two different orientations (circled island in Fig. 7.11 a). I assume that this asymmetry can be attributed to the influence of the comparatively large bromine atom.

The arrangement of 2-BrTPA can be stabilized by depositing close to one monolayer of molecules on the surface, similar to what was observed for unfunctionalized TPA. The (2×1) superstructure is still clearly discernible. However, whereas highly ordered superstructures were observed for TPA and 2-ATPA at monolayer coverages the 2-BrTPA structures display a much greater disorder (Fig. 7.12 a). Further increasing the coverage leads to ad-layers that are only weakly bound to the underlying first layer. Molecular resolution could not be achieved on these ad-layers, instead the molecules were easily removed from the scanning area during the measurement process (Fig. 7.12 b). In contrast to the flat-lying molecules in the first layer, the ad-layer displays a height of about 6 \AA (Fig. 7.12 c), indicating a tilted adsorption geometry. The focus in this section, however, will be laid on the adsorption geometry at sub-monolayer coverage.

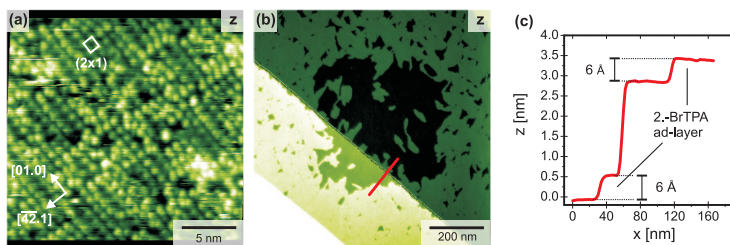


Figure 7.12: (a) 2-BrTPA at coverage of ~ 1 ML. The molecules are stabilized at this coverage. Image corrected for linear drift. (b) Situation after scanning on 2-BrTPA ad-layer. The rectangular scanning area is clearly visible. Structural resolution on the ad-layer was not possible. (c) Height profile along the line indicated in (b).

As an interesting effect, a shift of about 4 \AA along $[\overline{42.1}]$ of the molecular structures with respect to each other is observed when two rows of molecules, displaying two differently orientated asymmetries, are adsorbed next to each other. This shift is observed, *e.g.*, for the island at the lower right of Fig. 7.11 a and displayed, at higher magnification, in the topography image in Fig. 7.13.

Crystal structure data that were obtained through ADT measurements show chain formation of 2-BrTPA in the bulk, very similar to the TPA crystal structure. The bromine does not significantly influence the structure formation in the bulk, in contrast to what was observed for 2-ATPA.¹²⁷ However, upon deposition of 2-BrTPA on the calcite surface no extended chain formation along the substrate $[01.0]$ direction, as in the case of TPA and 2-ATPA, is observed. Instead, the molecules arrange into preferentially rectangular structures as described at the beginning of this section. In order to explain this structure formation, several aspects have to be considered.

The first one is the interaction mechanism between molecules and surface. In analogy to the electrostatic interaction of iodine and surface calcium cations as described in chapter 6, it is sensible to assume that the bromine as well will interact with the calcite surface, thus considerably influencing the adsorption geometry. The bromine atom should, ideally, serve as an anchor functionality here.

The second aspect derives from the molecular structure itself. Same as 2-ATPA, 2-BrTPA is prochiral as shown in the inset of Fig. 7.14, allowing for two different adsorption positions on the sample surface. Combined with the assumption of electrostatic

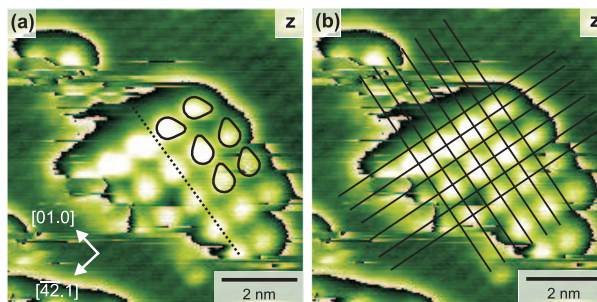


Figure 7.13: Magnification of Fig. 7.11. (a) The asymmetry is indicated by black outlines. In the upper row of the island, the direction of the asymmetry changes, leading to a displacement along $[4\bar{2}.1]$ as indicated by the dashed line. (b) By superimposing the grid of the atomically resolved substrate (solid lines) the adsorption position of 2-BrTPA is revealed.

interaction between bromine and calcium as described above, structures such as the circled island in Fig. 7.11 a, together with the observed shift along $[4\bar{2}.1]$ as shown in Fig. 7.13, can, therefore, easily be explained as transition between "domains" that are composed of different enantiomers of 2-BrTPA. Still, this does not explain why no extended chain formation along $[01.0]$ is observed. In order to explain this, a third aspect, namely the molecule's pK_a value has to be considered. In order to form extended chains through hydrogen bonds between two facing carboxyl groups, the molecules have to be protonated. The pK_a value of 2-BrTPA, however, suggests that the molecules are single-deprotonated when adsorbed on the sample,^{28,133} thus hindering the formation of extended rows along $[01.0]$ through hydrogen bonds between carboxyl groups. Yet, one proton per molecule is still available for the formation of a hydrogen bond between two 2-BrTPA molecules, thus explaining the observation of weakly bound short rows along $[01.0]$ as shown, *e.g.*, in Fig. 7.13.

Combining the considerations made above results in an adsorption model as shown in Fig. 7.14. From high-resolution images as shown in Fig. 7.13, the grid of the atomically resolved substrate could be superimposed on the molecular structures, leading to the conclusion that the center of each 2-BrTPA molecule is roughly placed above a surface carbonate group. This is in good agreement with the positioning of bromine on top of a surface

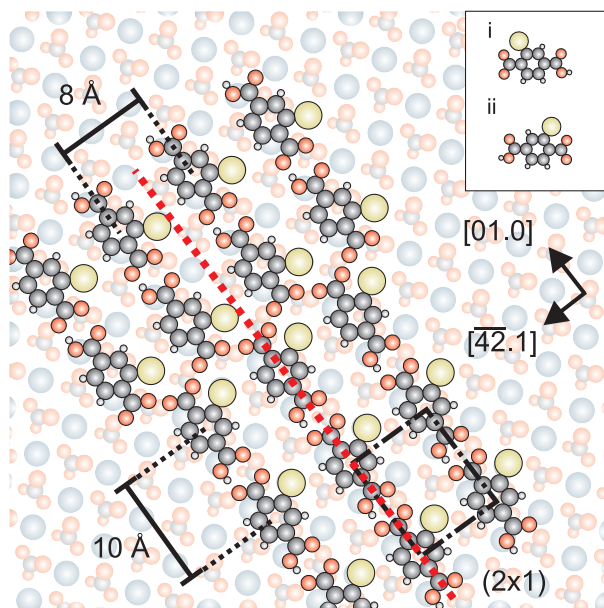


Figure 7.14: Adsorption model for 2-BrTPA. Displaced rows as indicated by the dashed line are caused by the different enantiomers (see inset). Short rows along [01.0] result from the formation of a hydrogen bond between two 2-BrTPA molecules. Competing molecule-surface interactions lead to unstable structures.

calcium cation as was proposed before for the electrostatic anchor mechanism. At the same time, however, the carboxylate is situated on top of surface carbonate group in this configuration, resulting in a repulsive interaction component between molecules and surface. The existence of these two competing interactions, therefore, readily explains the high molecular mobility that is observed for 2-BrTPA on the calcite surface.

In conclusion, the observed high molecular mobility demonstrated that introducing a single electrostatic bromine anchor functionality did not result in sufficient interaction with the surface in order to stabilize the 2-BrTPA molecules on the surface. As a result of the molecule's deprotonation, this Br/Ca interaction is additionally weakened by the competing COO/CO₃ interaction. In comparison, the two hydrogen bonds between a molecule's

amino group and a surface carbonate group in the case of 2-ATPA successfully anchored the molecules to the surface. In the next section I will, therefore, investigate the molecule 2-Br-5-PATPA that is equipped with an electrostatic bromine anchor but, at the same time, should allow for the formation of a single N-H \cdots O hydrogen bond to a surface carbonate group due to the additional phenylamine. In addition, the pK_a value of 2-Br-5-PATPA suggests that no deprotonation should occur, thus preventing competing interactions as was observed for 2-BrTPA.

7.4 2-Br-5-PATPA

Deposition of 2-Br-5-PATPA on calcite(10.4) results in even distribution of molecular structures over the sample surface as shown in Fig. 7.15 a, and no nucleation at the calcite step edges is observed. At smaller scales, rows along the substrate [01.0] direction are identified, together with mobile molecular species that appear as horizontal streaks in the image (Fig. 7.15 b). These mobile species lead to frequent contrast changes and hamper the acquisition of high-resolution images.

Imaging is slightly facilitated at higher coverages as shown in Fig. 7.15 c, where the rows agglomerate into island structures with an apparent row separation of $(16.5 \pm 1.0)\text{\AA}$, matching two times the surface unit cell repeat distance of 16.2\AA . High-resolution images (Fig. 7.15 d) reveal that each of the rows observed at larger scales is in fact composed of two rows of bright spots that are slightly shifted along [01.0] with respect to each other as indicated by the white circles in Fig. 7.15 d. The periodicity along [01.0] is $(10 \pm 1)\text{\AA}$, resulting in a (2×2) superstructure of the self-assembled 2-Br-5-PATPA molecules with respect to the substrate. Island reorganization as shown in Fig. 7.16 further corroborates the high molecular mobility at RT as was already indicated by the mobile species observed in Fig. 7.15 b.

For 2-ATPA and 2-BrTPA, the measured periodicities suggested that each bright spot in the topography images can be assigned to a single molecule. In the case of 2-Br-5-PATPA, however, the molecule is considerably larger due to the added phenylamine

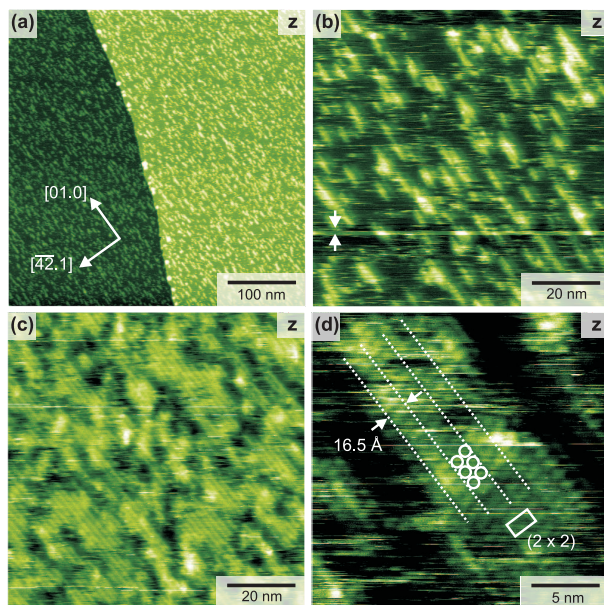


Figure 7.15: (a,b) 2-Br-5-PATPA on calcite(10.4). (b) Molecular rows along the calcite [01.0] direction are identified. Additionally, mobile species are visible as streaks in the image and can induce contrast changes as indicated by the white arrows. (c) Higher coverage of 2-Br-5-PATPA facilitates the imaging. (d) High-resolution image of sample shown in (c), displaying molecular double rows as indicated by the white circles. Dashed lines mark the row separation that was observed at larger scales. The (2×2) unit cell is drawn as well.

and the molecular dimensions do not allow the assignment of one spot to a single molecule. In fact, the molecular dimensions suggest that each 2-Br-5-PATPA molecule is imaged as two bright spots in the topography image.

An adsorption model for 2-Br-5-PATPA is given in Fig. 7.18. The formation of extended rows indicates that 2-Br-5-PATPA is still protonated as opposed to 2-BrTPA. Considering that the repeat distance and orientation along [01.0] matches exactly that of TPA and 2-ATPA, I, therefore, assume that the intermolecular interaction of the TPA backbone *via* facing -COOH groups remains the same as for those two molecules. Same as 2-ATPA

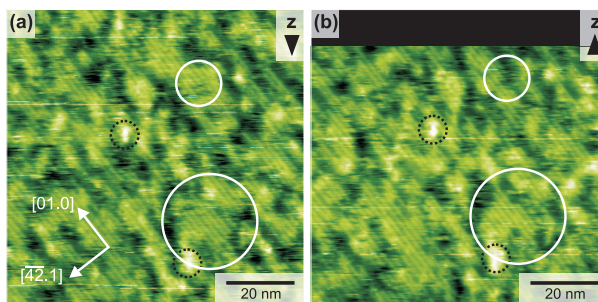


Figure 7.16: Consecutive topography images of 2-Br-5-PATPA. The white circled areas have changed significantly, indicating high molecular mobility. Dashed black circles serve as reference points. Acquisition time per image is 500 s.

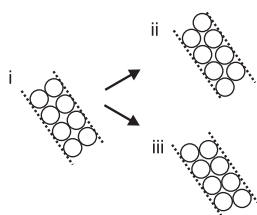


Figure 7.17: (i) Expected arrangement of bright spots in a molecular row. (ii, iii) Shift of bright spots. The direction of the shift depends on the enantiomer that composes the row.

and 2-BrTPA, 2-Br-5-PATPA is prochiral so that two different adsorption possibilities exist as shown in the inset of Fig. 7.18. For both configurations, the bromine can be positioned on top of a surface calcium cation to allow for electrostatic interaction as in the case of 2-BrTPA. Analogously to the geometrical considerations made for 2-ATPA, I assume that the 2-Br-5-PATPA islands are of homochiral composition.

In this configuration, one might assume to observe bright spots that are positioned right next to each other. During the measurements, however, a slight shift along $[01.0]$ as pictured in Fig. 7.17 is observed. This shift can most probably be attributed to the comparatively large bromine atom that leads to an asymmetric imaging of the 2-Br-5-PATPA molecule. At the same time, this shift enables the differentiation of islands with differing chirality. For two homochiral islands that are composed of different enantiomers this shift should be observed in different directions as depicted in Fig. 7.17. However, the high molecular mobility largely hindered the acquisition of high-resolution images that would enable an unambiguous identification of the different enantiomers.

In addition to the electrostatic interaction between bromine and calcium, hydrogen bonding between the molecule's nitrogen and a surface carbonate group is possible. The interaction of benzene with the calcite(10.4) surface is very weak, as was deduced from

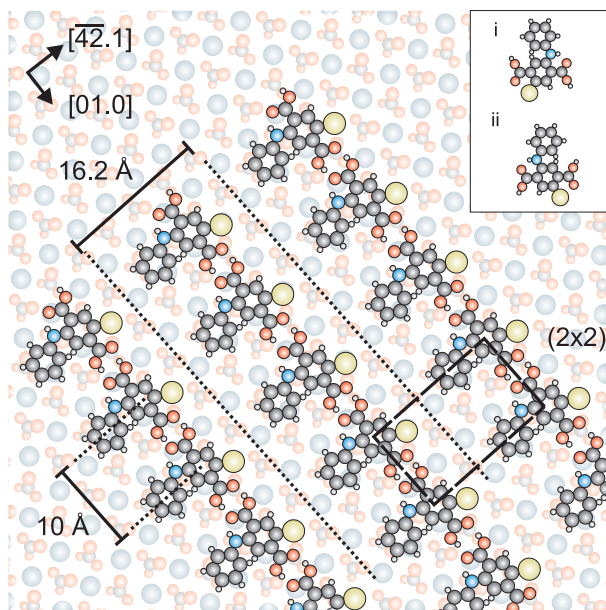


Figure 7.18: Adsorption model for 2-Br-5-PATPA on calcite(10.4). The dashed rectangle gives the unit cell of the (2×2) superstructure. In the acquired topography images, each molecule is imaged as two bright neighboring spots (Fig. 7.15 d).

experiments with hexa-*peri*-hexabenzocoronene (HBC) molecules.¹⁰⁷ The remaining benzene part of the phenylamine should, therefore, only contribute marginally to the molecule-surface interaction here.

In conclusion, a stabilization of the molecular arrangement on the surface was expected from the combination of electrostatic interaction between bromine and calcium and the formation of hydrogen bonds between nitrogen and carbonate groups. However, high molecular mobility as shown in Fig. 7.16 is observed instead, similar to what was observed for 2-BrTPA before. In combination with the results obtained for 2-ATPA and 2-BrTPA, however, this allows for a qualitative comparison of the different molecule-surface interactions. In contrast to 2-BrTPA, the 2-Br-5-PATPA molecules are still protonated so that no additional weakening of the Br/Ca *peri* interaction is expected. However, while

for 2-ATPA, the formation of two hydrogen bonds between an amino and a carbonate group was sufficient to stabilize the molecules on the surface, the combination of a single hydrogen bond anchor with the electrostatic bromine-calcium interaction does not result in significant differences in molecular mobility compared to what was observed for 2-BrTPA or TPA. Apparently, the formation of a second hydrogen bond as in the case of 2-ATPA is critical for achieving stable structure formation.

7.5 Conclusions

I present the investigation of different anchor functionalities in the self-assembly of several TPA-derivatives, namely 2-ATPA, 2-BrTPA and 2-Br-5-PATPA, and compare my results with previously performed work on unfunctionalized TPA. For the three molecules investigated here, a strong substrate templating effect was observed, resulting in structures whose repeat distances exactly match the calcite(10.4) main crystal directions $[01.0]$ and $[\overline{42}.1]$. The stability of those structures was critically influenced by the different anchor functionalities. For the proposed electrostatic anchor in 2-BrTPA and the combined anchors mechanisms encoded in 2-Br-5-PATPA, a similar mobility as for unfunctionalized TPA was observed. The added amino group of 2-ATPA, however, proved to be an efficient anchor functionality by successfully stabilizing the molecular structures on the calcite surface *via* the formation of two hydrogen bonds between the amino group and a surface carbonate group.

These findings emphasizes, once again, the importance of balancing and fine-tuning molecule-molecule and molecule-surface interactions in order to achieve stable, yet structurally flexible molecular arrangements on the sample surface.

8 Heptahelicene-2-carboxylic Acid

Contents

8.1 Introduction	94
8.2 Morphology at Room Temperature	96
8.3 Elevated Temperatures	101
8.4 Conclusions	102

IN the following chapter, I will present the investigation of enantiopure heptahelicene-2-carboxylic acid on the insulating calcite (10.4) surface as an example for the influence of chirality on the observed structure formation. I will demonstrate how distinctively different structures are formed upon deposition of the racemic mixture and the enantiopure molecules respectively.

The molecules used in this study were kindly supplied through a collaboration with the group of [REDACTED] at the Academy of Sciences of the Czech Republic in Prague.¹⁴¹

8.1 Introduction

The influence of chirality on molecular self-assembly on surfaces is of great interest within both, fundamental as well as application-oriented fields including, *e.g.*, chiral recognition and enantioselective catalysis.¹⁴² Ever since Louis Pasteur's famous experiment in 1848 on the manual separation of a racemic mixture,¹⁴³ the spontaneous segregation of a racemate into enantiopure crystallites has attracted great interest.^{104,144} When confined onto a two-dimensional surface, racemic mixtures most commonly form homochiral domains,^{145,146} but heterochiral molecular films having both enantiomers within the unit cell have also been observed.^{37,147} For tartaric acid on Cu(110), it has been shown that the formation of enantioseparated domains or racemic lattices is coverage-dependent.¹⁴⁸

Besides extended films, chiral recognition has been demonstrated to be decisive for the self-assembly of other structures, *e.g.*, molecular double rows³⁷ or dimers.¹⁴⁹ The detailed influence of chirality at the single molecular level and the substrate templating effect on the resulting mesoscopic or macroscopic expression of chirality is, however, still poorly understood.^{150,151} Moreover, the vast majority of chiral self-assembly investigations have been performed using scanning tunneling microscopy as direct imaging technique, limiting these studies to metallic surfaces.

Recently, my colleague [REDACTED] investigated the self-assembly of *racemic* heptahelicene-2-carboxylic acid ([7]HCA) molecules on the (10.4) cleavage plane of calcite using NC-AFM.¹⁵² In this work, he observed the formation of well-defined uni-directional molecular double rows upon adsorption onto the substrate held at room temperature. Based on an interplay between NC-AFM results and corresponding density-functional theory (DFT) calculations it was possible to draw a picture explaining the double row formation. In this model, hydrogen bond formation is responsible for dimerization of [7]HCA molecules while π - π interaction results in the uni-directional growth of the molecular rows. This picture is in agreement with a model of heterochiral recognition as driving force for the double row formation. However, based on the previous results and taking into account the

simplifications that had to be made for DFT calculations, an unambiguous clarification of this model has not been possible.

Here, I will therefore investigate the structure formation of one of the [7]HCA enantiomers, namely (*M*)-[7]HCA. In sharp contrast to the double rows that have been revealed before for the racemate, the *enantiopure* compound self-assembles into extended islands composed of rows directed along the [01.0] direction. This work, thus, elucidates the details of molecular double row formation and indicates that heterochiral recognition is decisive for the uni-directional double rows revealed for the racemic mixture. The results of this study have also been published in the Journal of Physical Chemistry C.³⁵

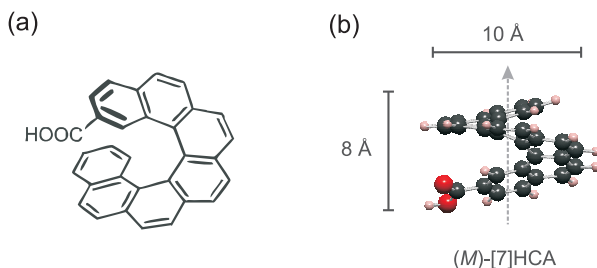


Figure 8.1: (a) Structural formula of [7]HCA. (b) Three-dimensional model of the (*M*)-[7]HCA molecule. The gray arrow marks the helical axis.

The molecule used in this work, namely the (*M*)-[7]HCA molecule, is shown in Fig. 8.1. Seven benzene rings are arranged such as to form a screw-like structure, resulting in two possible helicities of the molecule. For this study, the heptahelicene was functionalized with a carboxylic group at one end of the screw structure. The synthesis of the racemic mixture relies on the Co^{I} -mediated [2+2+2] cycloisomerization of an aromatic triyne to build the helical skeleton.¹⁴¹ Separation of the enantiomers was performed by preparative liquid chromatography on a chiral stationary phase column.¹⁴¹

8.2 Morphology at Room Temperature

First, I will discuss the structures formed after depositing the left-handed (*M*)-[7]HCA molecule onto calcite(10.4) held at RT. A representative image is given in Fig. 8.2 (a). In this image, island structures are revealed that are oriented along the [01.0] direction of the underlying substrate. The enantiopure islands are, except for their orientation, distributed randomly over the surface at a coverage of < 0.1 monolayer. Two step edges, running as straight lines from top to bottom, can be seen at the right side of the image. The islands are formed on flat terraces and the step edges do not provide nucleation centers for island growth. Even at increased coverages, no agglomeration at the step edges takes place (not shown). These results obtained for the enantiopure compound differ significantly from the structures that have been observed before for the racemic mixture of [7]HCA.¹⁵²

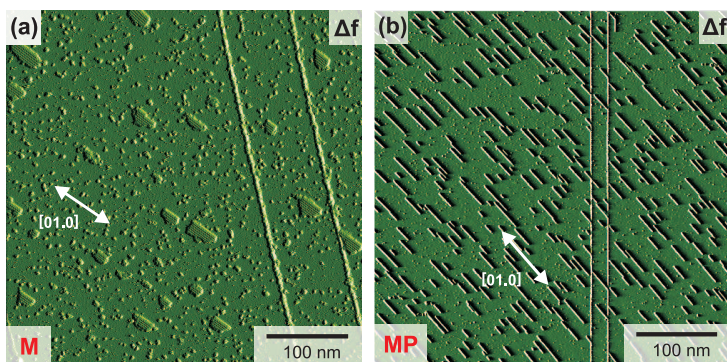


Figure 8.2: Frequency shift images of enantiopure and racemic [7]HCA on calcite(10.4). (a) Enantiopure (*M*)-[7]HCA islands. (b) Racemic [7]HCA mixture forming uni-directional double rows. Image adapted from Ref. 152. Both images show calcite step edges, visible as straight lines running from top to bottom.

A typical image showing the structures revealed after deposition of the racemate is reproduced in Fig. 8.2 (b). In the previous study using the racemate, it was shown that uni-directional rows are formed aligned along the [01.0] direction. High-resolution

NC-AFM images have revealed that these structures are composed of molecular double rows. In combination with DFT calculations a model for the double row formation was proposed, which is based on dimerization through hydrogen bond formation of the carboxylic groups, while π - π interaction leads to a binding of the molecular dimers along the row direction. Although it was already speculated that heterochiral recognition might take place in the case of the racemate, the previous results did not allow for an unambiguous identification whether the observed rows were homochiral or heterochiral.

This question can now be addressed based on the results obtained in the present study using the enantiopure compound. The fact that racemic and enantiopure [7]HCA form distinctly different structures on the same substrate is a strong indication that the previously observed molecular double rows indeed originate from heterochiral recognition. This will be further corroborated by the detailed investigation of the enantiopure islands presented in the following.

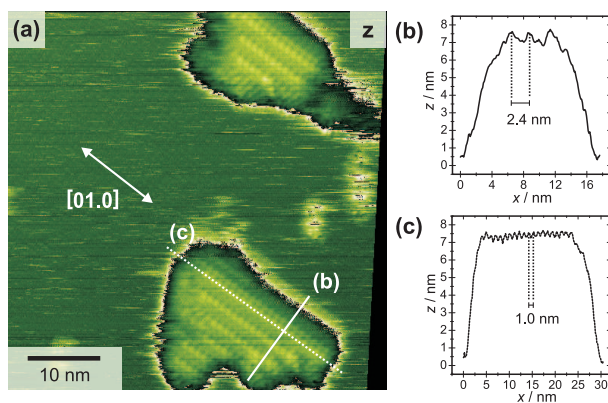


Figure 8.3: (a) High-resolution topography image of molecular islands formed by (*M*)-[7]HCA. The underlying calcite substrate is resolved simultaneously. A double color scale is used for data representation in order to enhance visibility. Additionally, the image was corrected for linear thermal drift. (b) and (c) Height profiles along the calcite [42.1] and [01.0] direction, respectively, as indicated by the drawn lines.

Fig. 8.3 (a) shows a high-resolution image of two (*M*)-[7]HCA islands. Note that the underlying calcite substrate is imaged si-

multaneously, providing an inherent lateral length calibration. The (*M*)-[7]HCA islands are imaged with an apparent height of typically 0.7 nm, as shown in the height profiles provided in Fig. 8.3 (b) and (c). Considering the van-der-Waals radius of an individual molecule, a height of about 1.15 nm would be expected for upright standing molecules (*i.e.* the helical axis being vertical to the surface plane). This discrepancy to the apparent height measured in this study can be readily explained if one assumes that the adsorbed molecules' helical axis is tilted relative to the surface plane. This interpretation is in agreement with previous studies on the racemic mixture. A tilted adsorption geometry was also observed by Ernst *et al.* for heptahelicene molecules in a saturated monolayer on Ni(100).¹⁵³

Already at the scale presented in Fig. 8.3 (a) (image size of $435 \times 435 \text{ nm}^2$), the (*M*)-[7]HCA islands clearly reveal an inner structure, consisting of parallel rows oriented along the [01.0] direction of the crystal. At sub-monolayer coverage, the islands typically consist of 4-6 of these rows. The rows exhibit a repeat distance of $(2.3 \pm 0.1) \text{ nm}$ along the $[\sqrt{2}.1]$ direction, as confirmed by the height profile given in Fig. 8.3 (b). This distance is about twice as large as the distance one would expect for two neighboring (*M*)-[7]HCA molecules, indicating that two molecules align along this direction with one molecule being imaged brighter than the other. The observed height difference between these two molecules is in the order of 0.02 nm to 0.05 nm.

Regarding these apparent height differences it is important to stress once again that the measured variable in NC-AFM is the change in the cantilever's resonance frequency due to the interaction of tip and sample. Use of a feedback loop then allows to gain topography information from this frequency shift. This means that the measured height represents a plane of equal interaction and might, for example, also be influenced by the shape of the tip or electrostatic forces as well.⁹⁵

Along the molecular rows, a clearly visible corrugation following the calcite [01.0] direction can be identified as shown in the height profile in Fig. 8.3 (c). The corrugation exhibits a periodicity of $(1.0 \pm 0.1) \text{ nm}$, which agrees with an assignment of each of these bright spots to a single (*M*)-[7]HCA molecule. Overall, a (2

$\times 3$) superstructure can be assigned for the (*M*)-[7]HCA islands, as depicted in Fig. 8.4.

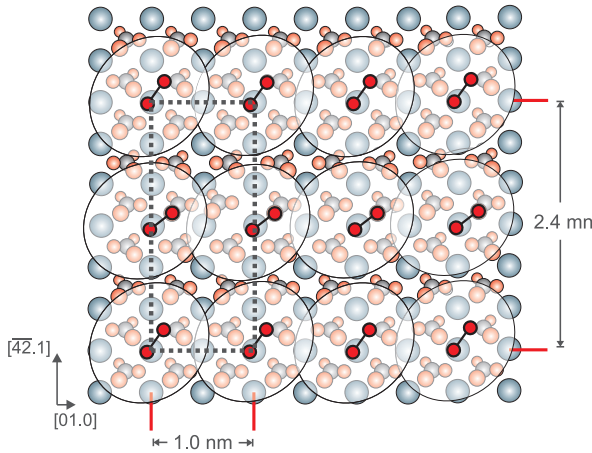


Figure 8.4: Top view of the calcite(10.4) surface with adsorbed (*M*)-[7]HCA molecules. The (*M*)-[7]HCA molecules are represented by their van-der-Waals radii (shaded ellipses) and the carboxylic groups only (linked red discs representing the oxygen atoms). The unit cell of the (2×3) superstructure is marked by the dashed rectangle.

A model suggested by the NC-AFM data for the molecules' adsorption geometry is given in Fig. 8.5. I assume that the (*M*)-[7]HCA molecules adsorb with the carboxylic acid moiety pointing towards the calcite surface, where the carbonyl oxygen is expected to bind to a surface calcium atom, whereas the hydroxyl group will bind to an oxygen atom of a carbonate group. Such a binding behavior has been studied theoretically²⁷ and agrees well with the experimental determined binding of other -COOH functionalized molecules.²⁸

As mentioned above, the two carbonate groups within the unit cell are rotated with respect to each other. This results into a different binding geometry for every second (*M*)-[7]HCA molecule along the $[4\bar{2}.1]$ direction. This fact provides a straightforward explanation for the different appearance of two molecules along this direction: The different binding geometry inevitably results in a different orientation of the molecules with respect to each other, which apparently is propagated to a height difference.

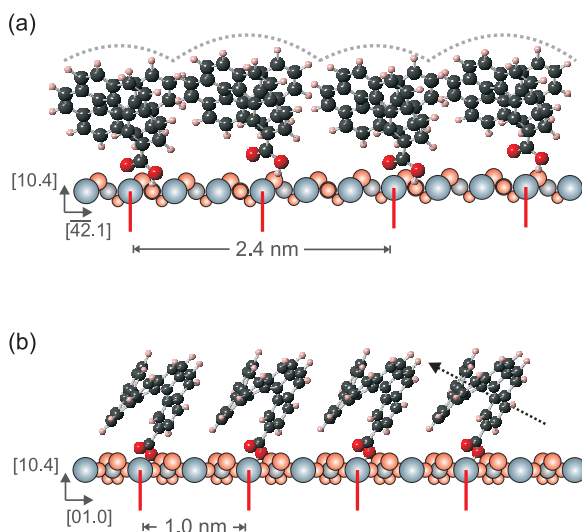


Figure 8.5: Side views of the calcite(10.4) surface with suggested adsorption geometry of (*M*)-[7]HCA molecules. (a) Along the $[42.1]$ direction, the measured repeat distance is 2.4 nm. Binding to different surface carbonate groups leads to a different orientation of the molecules. (b) Along the $[01.0]$ direction, the measured repeat distance is 1.0 nm, twice the unit cell repeat distance of calcite along this direction. The dashed arrow marks the molecules' helical axis to indicate the tilt.

I now continue this discussion by studying the morphology evolution of the formed island structures. Imaging directly after deposition of the molecules (*i.e.*, approximately one hour after deposition) already reveals the aforementioned islands, together with a high density of smaller features (not shown here). During the scanning process the density of the latter decreased, whereas the islands grew in area. I hence assume that most of these smaller features were indeed small (*M*)-[7]HCA units, diffusing freely on the surface until binding to already formed islands. This is similar to what has been revealed for the racemate, where a transient row structure has been observed in images taken approximately one hour after deposition, consisting of single rows that transform into the double rows discussed above.¹⁵²

Single rows have also been found for the enantiopure compound shortly after deposition, although their observed density is somewhat less than for the racemate. Assuming the racemic double rows to be of heterochiral composition, the single rows observed in that case are presumably formed by only one of the enantiomers. Over time, the single rows vanish and exclusively molecular double rows remain, which leads to the conclusion that the molecular double rows are energetically favored over molecular single rows. When depositing the (*M*)-[7]HCA molecules, enantiopure units have no counterpart to form heterochiral structures such as the double rows and, thus, they agglomerate into islands instead.

In order to evaluate whether a morphology evolution of the (*M*)-[7]HCA islands takes place on longer timescales than the usual scanning process, some of the samples were stored under UHV conditions after the initial molecule deposition and imaging. I waited for three days and performed additional imaging after that period. These measurements did not reveal any changes in the morphology of the islands structures, indicating that the island structures represent a rather stable configuration at this temperature.

8.3 Elevated Temperatures

To investigate the effect of higher temperatures on the formed structures, (*M*)-[7]HCA was deposited on a freshly prepared calcite sample and subsequently heated. Prior to heating, the sample was imaged to ensure that the expected island formation had taken place. Heating up to temperatures of ~360 K produced no observable change in morphology. However, when increasing the temperature further to ~400 K and annealing the sample for 1 h, I found that the number of molecular islands had decreased whereas their individual areas had increased. The average increase in island size is of the factor of 4-6. The inner island structure, however, was not changed compared to the situation before annealing, as can be seen in the image shown in Fig. 8.6. The orientation of these annealed islands remained along the calcite [01.0] direction, which emphasizes the strong templating effect

of the underlying substrate. As before, the step edges did not act as nucleation centers for the (*M*)-[7]HCA islands. Further elevating the annealing temperature to ~ 415 K caused the islands to vanish and I did not observe any other ordered structures, in particular no molecular double rows as would be expected for the aforementioned racemic mixture.

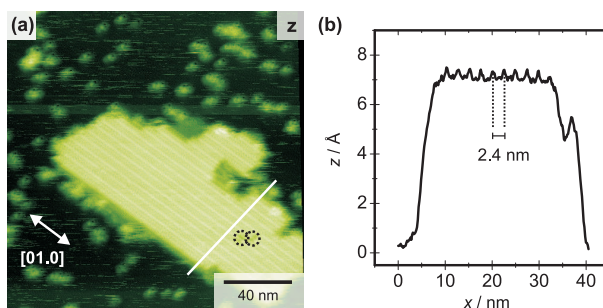


Figure 8.6: (a) (*M*)-[7]HCA island after annealing to ~ 400 K for 1 h (Image corrected for linear drift). The dashed circles show defects on the molecular rows. (b) Height profile along the indicated line. The annealed islands do not show differences in height and periodicity in comparison to the island structures observed at room temperature.

8.4 Conclusions

I report the formation of homochiral (*M*)-[7]HCA islands on the calcite(10.4) surface. The substrate has a strong templating effect on the adsorption of the molecules, which is shown by the common orientation of the islands along the [01.0] direction and the modulated height of the molecular rows along the $[\overline{42}.1]$ direction. This island formation is in sharp contrast to the formation of uni-directional double rows, which has been observed before for the deposition of racemic [7]HCA onto the same surface. My findings, thus, elucidate the influence of chirality on the double row formation and indicate that heterochiral recognition is responsible for the row formation of the racemate. Chirality, thus, proves to be another important parameter to steer the intermolecular interaction on the surface.

Being aware of this difference between the hetero- and homochiral structures of [7]HCA, a promising step would be to equip the molecule with an additional -COOH group at position 17, yielding [7]helicene-2,17-dicarboxylic acid ([7]HDCA) as shown in Fig. 8.7. Whereas one of the carboxy groups can still act as an anchor to the calcite surface here, the second one is now available for possible formation of carboxylic acid dimers. It would be intriguing to investigate, whether in this configuration the heterochiral racemate will still assemble into double rows as before, or whether it will be driven into island structures resembling those of the enantiopure molecules.

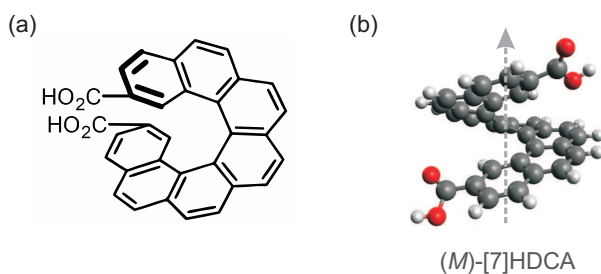


Figure 8.7: (a) Structural formula of [7]HDCA with two carboxylic acid groups. (b) Three-dimensional model.

9 Summary

IN conclusion, this thesis describes the investigation of systematically varied organic molecules for use in molecular self-assembly processes. All experiments were performed using high-resolution non-contact atomic force microscopy under UHV conditions and at room temperature. Using this technique, three different approaches for influencing intermolecular and molecule-surface interaction on the insulating calcite(10.4) surface were investigated by imaging the structure formation at the molecular scale.

In chapter 6, I demonstrated the systematic variation of molecular cohesion for a set of molecules with identical adhesion to an insulating substrate. To achieve this, the functionalization of shape-persistent oligo(*p*-benzamide)s was engineered by introducing different functional groups and investigating their effect on the structural formation on the sample surface. The molecular core was designed to provide significant electrostatic anchoring towards the surface *via* the interaction of iodine atoms with surface calcium cations, while at the same time maintaining the flexibility to fine-tune the resulting structure by adjusting the intermolecular cohesion energy.

The success of this strategy is based on a clear separation of the molecule-substrate interaction from the molecule-molecule interaction. My results show that sufficient molecule-surface anchoring can be achieved without restricting the structural flexibility that is needed for the design of complex molecular systems.

Three derivatives of terephthalic acid (TPA) were investigated in chapter 7. Here, as opposed to the oligo(*p*-benzamide)s presented before, the focus was on changing the adhesion to the calcite surface by introducing different anchor functionalities to the TPA backbone. The structural formation for aminoterephthalic acid (2-ATPA) and 2-bromo-5-phenylaminoterephthalic acid (2-Br-5-PATPA) is very similar and mainly driven by the interaction between facing carboxyl groups. For 2-bromoterephthalic acid (2-BrTPA), structure formation and interaction differ from the chain formation that is usually observed for TPA derivatives, which is attributed to deprotonation of the molecule. For all observed molecules, the strong substrate templating effect results in molecular structures that are strictly oriented along the calcite main crystal directions. This templating is especially pronounced in the case of 2-ATPA where chain formation on the calcite surface is observed in contrast to the formation of molecular layers in the bulk. At the same time, the amino group of 2-ATPA proved to be the most efficient anchor functionality among the investigated molecules, successfully stabilizing the molecular chains on the sample surface.

These findings emphasize, once again, the importance of balancing and fine-tuning molecule-molecule and molecule-surface interactions in order to achieve stable, yet structurally flexible molecular arrangements on the sample surface.

In the last chapter, I showed how the intrinsic property of molecular chirality decisively influences the structure formation in molecular self-assembly. To some extent, this was already observed for the OIB and TPA based molecules described in the chapters before. However, the effect of chirality on the self-assembly process is even more pronounced in the case of the investigated heptahelicene-2-carboxylic acid. This molecule exhibits a helical chirality, so that two enantiomers with different sense of rotation exist. Deposition of the enantiopure molecules results in the formation of homochiral islands on the sample surface. This island formation is in sharp contrast to the formation of uni-directional double rows, which has been observed before for the deposition of the racemate onto the same surface. While it remained uncertain from these previous experiments whether the double rows are composed of hetero- or homochiral molecules, I could clearly answer that question here and demonstrate

that the rows are, in fact, of heterochiral origin.

My findings elucidate the influence of chirality on the double row formation and indicate that heterochiral recognition is responsible for the row formation of the racemate. Chirality, thus, proves to be another important parameter to steer the intermolecular interaction on surfaces.

Altogether, the results of this thesis demonstrate that, in order to successfully control the structure formation in molecular self-assembly, the correct combination of molecule and surface properties is crucial. This is of special importance when working on substrates that exhibit a strong influence on the structure formation, such as the calcite(10.4) surface. Through the systematic variation of functional groups several important parameters that influence the balance between molecule-surface and molecule-molecule interaction were identified here, and the results of this thesis can, thus, act as a guideline for the rational design of molecules for use in molecular self-assembly.

Bibliography

1. T. ITO, S. OKAZAKI: Pushing the Limits of Lithography.
Nature **406**, 1027 (2000)
2. D. M. EIGLER, E. K. SCHWEIZER: Positioning Single Atoms with a Scanning Tunneling Microscope.
Nature **344**, 524 (1990)
3. A. KÜHNLE: Self-assembly of Organic Molecules at Metal Surfaces.
Current Opinion in Colloid and Interface Science **14**, 157 (2009)
4. G. M. WHITESIDES, J. P. MATHIAS, C. T. SETO: Molecular Self-assembly and Nanochemistry: A Chemical Strategy for the Synthesis of Nanostructures.
Science **254**, 1312 (1991)
5. G. M. WHITESIDES, B. GRZYBOWSKI: Self-assembly at all Scales.
Science **295**, 2418 (2002)
6. J. V. BARTH: Molecular Architectonic on Metal Surfaces.
Annual Review of Physical Chemistry **58**, 375 (2007)
7. V. OISON, M. KOUDIA, M. ABEL, L. PORTE: Influence of Stress on Hydrogen-bond Formation in a Halogenated Phthalocyanine Network.
Physical Review B **75**, 035428 (2007)
8. A. KÜHNLE, L. M. MOLINA, T. R. LINDEROTH, B. HAMMER, F. BESENBACHER: Growth of Unidirectional Molecular Rows of Cysteine on Au(110)-(1x2) Driven by

- Adsorbate-Induced Surface Rearrangements.
Physical Review Letters **93**, 086101 (2004)
9. M. BÖHRINGER, K. MORGENSTERN, W.-D. SCHNEIDER, R. BERNDT, F. MAURI, A. D. VITA, R. CAR: Two-Dimensional Self-Assembly of Supramolecular Clusters and Chains.
Physical Review Letters **83**, 324 (1999)
10. J. V. BARTH, J. WECKESSER, C. CAI, P. GÜNTER, L. BÜRGI, O. JEANDUPEUX, K. KERN: Building Supramolecular Nanostructures at Surfaces by Hydrogen Bonding.
Angewandte Chemie, International Edition **39**, 1230 (2000)
11. A. KÜHNLE, T. R. LINDEROTH, F. BESENBACHER: Self-Assembly of Monodispersed, Chiral Nanoclusters of Cysteine on the Au(110)-(1x2) Surface.
Journal of the American Chemical Society **125**, 14680 (2003)
12. G. PAWIN, K. L. WONG, K. Y. KWON, L. BARTELS: A Homomolecular Porous Network at a Cu(111) Surface.
Science **313**, 961 (2006)
13. S. STEPANOW, M. LINGENFELDER, A. DMITRIEV, H. SPILLMANN, E. DELVIGNE, N. LIN, X. DENG, C. CAI, J. V. BARTH, K. KERN: Steering Molecular Organization and Host-guest Interactions Using Two-dimensional Nanoporous Coordination Systems.
Nature Materials **3**, 229 (2004)
14. R. HOFFMANN: A Chemical and Theoretical Way to Look at Bonding on Surfaces.
Reviews of Modern Physics **60**, 601 (1988)
15. A. HAUSCHILD, K. KARKI, B. C. C. COWIE, M. ROHLFING, F. S. TAUTZ, M. SOKOLOWSKI: Molecular Distortions and Chemical Bonding of a Large p-Conjugated Molecule

- on a Metal Surface.
Physical Review Letters **94**, 036106 (2005)
16. B. SUCH, T. TREVETHAN, T. GLATZEL, S. KAWAI, L. ZIMMERLI, E. MEYER, A. L. SHLUGER, C. H. M. AMIJS, P. DE MENDOZA, A. M. ECHAVARREN: Functionalized Truxenes: Adsorption and Diffusion of Single Molecules on the KBr(001) Surface.
ACS Nano **4**, 3429 (2010)
 17. L. NONY, R. BENNEWITZ, O. PFEIFFER, E. GNECCO, A. BARATOFF, E. MEYER, T. EGUCHI, A. GOURDON, C. JOACHIM: Cu-TBPP and PTCDA Molecules on Insulating Surfaces Studied by Ultra-high-vacuum Non-contact AFM.
Nanotechnology **15**, S91 (2004)
 18. T. KUNSTMANN, A. SCHLARB, M. FENDRICH, T. WAGNER, R. MÖLLER, R. HOFFMANN: Dynamic Force Microscopy Study of 3,4,9,10-perylenetetracarboxylic Dianhydride on KBr(001).
Physical Review B **71**, 121403 (2005)
 19. E. BAUER: Phänomenologische Theorie der Kristallabscheidung an Oberflächen I.
Zeitschrift für Kristallographie **110**, 372 (1958)
 20. F. CICOIRA, C. SANTATO, F. ROSEI: Two-Dimensional Nanotemplates as Surface Cues for the Controlled Assembly of Organic Molecules.
Topics in Current Chemistry **285**, 203 (2008)
 21. L. NONY, E. GNECCO, A. BARATOFF, A. ALKAUSKAS, R. BENNEWITZ, O. PFEIFFER, S. MAIER, A. WETZEL, E. MEYER, C. GERBER: Observation of Individual Molecules Trapped on a Nanostructured Insulator.
Nano Letters **4**, 2185 (2004)
 22. L. VITOS, A. V. RUBAN, H. L. SKRIVER, J. KOLLAR: The Surface Energy of Metals.
Surface Science **411**, 186 (1998)

23. F. VAN ZEGGEREN, G. C. BENSON: Calculation of the Surface Energies of Alkali Halide Crystals. *The Journal of Chemical Physics* **26**, 1077 (1957)
24. R. KRISTENSEN, S. L. S. STIPP, K. REFSON: Modeling Steps and Kinks on the Surface of Calcite. *Journal of Chemical Physics* **121**, 8511 (2004)
25. P. RAHE, R. LINDNER, M. KITTELMANN, M. NIMMRICH, A. KÜHNLE: From Dewetting to Wetting Molecular Layers: C60 on CaCO₃(10 $\bar{1}$ 4) as a Case Study. *Physical Chemistry Chemical Physics* **14**, 6544 (2012)
26. O. H. PAKARINEN, J. M. MATIVETSKY, A. GULANS, M. J. PUSKA, A. S. FOSTER, P. GRUTTER: Role of van der Waals Forces in the Adsorption and Diffusion of Organic Molecules on an Insulating Surface. *Physical Review B* **80**, 085401 (2009)
27. D. M. DUFFY, J. H. HARDING: Modelling the Interfaces Between Calcite Crystals and Langmuir Monolayers. *Journal of Materials Chemistry* **12**, 3419 (2002)
28. M. KITTELMANN, P. RAHE, M. NIMMRICH, C. M. HAUKE, A. GOURDON, A. KÜHNLE: On-Surface Covalent Linking of Organic Building Blocks on a Bulk Insulator. *ACS Nano* **5**, 8420 (2011)
29. R. PAWLAK, L. NONY, F. BOCQUET, V. OLSON, M. SASSI, J. M. DEBIERRE, C. LOPPACHER, L. PORTE: Supramolecular Assemblies of 1,4-Benzene Diboronic Acid on KCl(001). *Journal of Physical Chemistry C* **114**, 9290 (2010)
30. M. FENDRICH, T. KUNSTMANN: Organic Molecular Nanowires: N,N'-dimethylperylene-3,4,9,10-bis(dicarboximide) on KBr(001). *Applied Physics Letters* **91**, 023101 (2007)
31. S. MAIER, L.-A. FENDT, L. ZIMMERLI, T. GLATZEL, O. PFEIFFER, F. DIEDERICH, E. MEYER: Nanoscale En-

- gineering of Molecular Porphyrin Wires on Insulating Surfaces.
Small **4**, 1115 (2008)
32. M. FENDRICH, M. LANGE, C. WEISS, T. KUNSTMANN, R. MOLLER: N,N'-dimethylperylene-3,4,9,10-bis(dicarboximide) on Alkali Halide (001) Surfaces.
Journal of Applied Physics **105**, 094311 (2009)
33. J. SCHÜTTE, R. BECHSTEIN, M. ROHLFING, M. REICHLING, A. KÜHNLE: Cooperative Mechanism for Anchoring Highly Polar Molecules at an Ionic Surface.
Physical Review B **80**, 205421 (2009)
34. A. HINAUT, A. PUJOL, F. CHAUMETON, D. MARTROU, A. GOURDON, S. GAUTHIER: An NC-AFM and KPFM Study of the Adsorption of a Triphenylene Derivative on KBr (001).
Beilstein Journal of Nanotechnology **3**, 221 (2012)
35. C. M. HAUKE, P. RAHE, M. NIMMRICH, J. SCHÜTTE, M. KITTELMANN, I. G. STARÁ, I. STARÝ, J. RYBÁČEK, A. KÜHNLE: Molecular Self-Assembly of Enantiopure Heptahelicene-2-Carboxylic Acid on Calcite (10 $\bar{1}$ 4).
The Journal of Physical Chemistry C **116**, 4637 (2012)
36. P. RAHE, M. NIMMRICH, A. KÜHNLE: Substrate Templating upon Self-Assembly of Hydrogen-Bonded Molecular Networks on an Insulating Surface.
Small **8**, 2969 (2012)
37. M. BÖHRINGER, W.-D. SCHNEIDER, R. BERNDT: Real Space Observation of a Chiral Phase Transition in a Two-Dimensional Organic Layer.
Angewandte Chemie, International Edition **39**, 792 (2000)
38. J. I. PASCUAL, J. V. BARTH, G. CEBALLOS, G. TRIMARCHI, A. DE VITA, K. KERN, H. P. RUST: Mesoscopic Chiral Reshaping of the Ag(110) Surface Induced by the Organic Molecule PVBA.
Journal of Chemical Physics **120**, 11367 (2004)

39. J. V. BARTH, J. WECKESSER, G. TRIMARCHI, M. VLADIMIROVA, A. DE VITA, C. CAI, H. BRUNE, P. GÜNTER, K. KERN: Stereochemical Effects in Supramolecular Self-Assembly at Surfaces: 1-D versus 2-D Enantiomorphic Ordering for PVBA and PEBA on Ag(111).
Journal of the American Chemical Society **124**, 7991 (2002)
40. S. STEPANOW, N. LIN, F. VIDAL, A. LANDA, M. RUBEN, J. V. BARTH, K. KERN: Programming Supramolecular Assembly and Chirality in Two-Dimensional Dicarboxylate Networks on a Cu(100) Surface.
Nano Letters **5**, 901 (2005)
41. K.-H. ERNST: Molecular Chirality at Surfaces.
Physica Status Solidi B **249**, 2057 (2012)
42. N. LIN, S. STEPANOW, F. VIDAL, K. KERN, M. S. ALAM, S. STROMSDORFER, V. DREMOV, P. MULLER, A. LANDA, M. RUBEN: Surface-assisted Coordination Chemistry and Self-assembly.
Dalton Transactions (2006)
43. G. BINNIG, C. QUATE, C. GERBER: Atomic Force Microscope.
Physical Review Letters **56**, 930 (1986)
44. G. BINNIG, H. ROHRER, C. GERBER, E. WEIBEL: Surface Studies by Scanning Tunneling Microscopy.
Physical Review Letters **49**, 57 (1982)
45. M. A. LANTZ, H. J. HUG, R. HOFFMANN, P. J. A. VAN SCHENDEL, P. KAPPENBERGER, S. MARTIN, A. BARATOFF, H. J. GÜNTHERODT: Quantitative Measurement of Short-range Chemical Bonding Forces.
Science **291**, 2580 (2001)
46. J. LÜBBE, L. TRÖGER, S. TORBRÜGGE, R. BECHSTEIN, C. RICHTER, A. KÜHNLE, M. REICHLING: Achieving High Effective Q-factors in Ultra-high Vacuum Dynamic

- Force Microscopy.
Measurement Science and Technology **21**, 125501 (2010)
47. J. E. LENNARD-JONES: Cohesion.
Proceedings of the Physical Society **43**, 461 (1931)
48. G. MIE: Zur kinetischen Theorie der einatomigen Körper.
Annalen der Physik **316**, 657 (1903)
49. F. J. GIESSIBL: A Direct Method to Calculate Tip-sample Forces from Frequency Shifts in Frequency-modulation Atomic Force Microscopy.
Applied Physics Letters **78**, 123 (2001)
50. J. E. SADER, S. P. JARVIS: Accurate Formulas for Interaction Force and Energy in Frequency Modulation Force Spectroscopy.
Applied Physics Letters **84**, 1801 (2004)
51. F. H. STILLINGER, T. A. WEBER: Computer Simulation of Local Order in Condensed Phases of Silicon.
Physical Review B **31**, 5262 (1985)
52. M. NONNENMACHER, M. P. O'BOYLE, H. K. WICKRAMASINGHE: Kelvin Probe Force Microscopy.
Applied Physics Letters **58**, 2921 (1991)
53. W. H. KEESOM: Die van der Waalsschen Kohäsionskräfte.
Physikalische Zeit **22**, 129 (1921)
54. P. J. W. DEBYE: Polar Molecules. Bd. 172. Dover New York, 1929
55. F. LONDON: Zur Theorie und Systematik der Molekularkräfte.
Zeitschrift für Physik **63**, 245 (1930)
56. J. N. ISRAELACHVILI, D. TABOR: The Measurement of Van Der Waals Dispersion Forces in the Range 1.5 to 130 nm.

- Proceedings of the Royal Society of London. A. Mathematical and Physical Sciences **331**, 19 (1972)
57. J. N. ISRAELACHVILI: Intermolecular and Surface Forces. Second Edition. Academic Press, 1985
58. F. LOSKE, P. RAHE, A. KÜHNLE: Contrast Inversion in Non-contact Atomic Force Microscopy Imaging of C60 Molecules. *Nanotechnology* **20**, 264010 (2009)
59. R. PÉREZ, M. C. PAYNE, I. ŠTICH, K. TERAURA: Contrast Mechanism in Non-contact AFM on Reactive Surfaces. *Applied Surface Science* **123/124**, 249 (1998)
60. F. OHNESORGE, G. BINNIG: True Atomic Resolution by Atomic Force Microscopy Through Repulsive and Attractive Forces. *Science* **260**, 1451 (1993)
61. P. RAHE, R. BECHSTEIN, J. SCHÜTTE, F. OSTENDORF, A. KÜHNLE: Repulsive Interaction and Contrast Inversion in Noncontact Atomic Force Microscopy Imaging of Adsorbates. *Physical Review B* **77**, 195410 (2008)
62. F. J. GIESSIBL: Forces and Frequency Shifts in Atomic-resolution Dynamic-force Microscopy. *Physical Review B: Condensed Matter* **56**, 16010 (1997)
63. S. RODE, N. OYABU, K. KOBAYASHI, H. YAMADA, A. KÜHNLE: True Atomic-Resolution Imaging of (10-14) Calcite in Aqueous Solution by Frequency Modulation Atomic Force Microscopy. *Langmuir* **25**, 2850 (2009)
64. Y. MARTIN, C. C. WILLIAMS, H. K. WICKRAMASINGHE: Atomic Force Microscope-force Mapping and Profiling on a Sub 100-Å Scale. *Journal of Applied Physics* **61**, 4723 (1987)

65. Q. ZHONG, D. INNISS, K. KJOLLER, V. ELINGS: Fractured Polymer/Silica Fiber Surface Studied by Tapping Mode Atomic Force Microscopy. *Surface Science Letters* **290**, L688 (1993)
66. T. R. ALBRECHT, P. GRÜTTER, D. HORNE, D. RUGAR: Frequency-Modulation Detection Using High-Q Cantilevers for Enhanced Force Microscope Sensitivity. *Journal of Applied Physics* **69**, 668 (1991)
67. H. HÖLSCHER, U. D. SCHWARZ, R. WIESENDANGER: Calculation of the Frequency Shift in Dynamic Force Microscopy. *Applied Surface Science* **140**, 344 (1999)
68. F. J. GIESSIBL: Atomic Resolution of the Silicon (111)-(7x7) Surface by Atomic Force Microscopy. *Science* **267**, 68 (1995)
69. F. J. GIESSIBL, H. BIELEFELDT, S. HEMBACHER, J. MANNHART: Calculation of the Optimal Imaging Parameters for Frequency Modulation Atomic Force Microscopy. *Applied Surface Science* **140**, 352 (1999)
70. H. HÖLSCHER, A. SCHWARZ, W. ALLERS, U. D. SCHWARZ, R. WIESENDANGER: Quantitative Analysis of Dynamic-force-spectroscopy Data on Graphite(0001) in the Contact and Noncontact Regimes. *Physical Review B* **61**, 12678 (2000)
71. B. KRACKE, B. DAMASCHKE: Ultrahigh Vacuum Scanning Force Microscope with Fiber-optic Deflection Sensor. *Review of Scientific Instruments* **67**, 2957 (1996)
72. N. BLANC, J. BRUGGER, N. F. DE ROOIJ, U. DÜRIG: Scanning Force Microscopy in the Dynamic Mode Using Microfabricated Capacitive Sensors. *Journal of Vacuum Science and Technology B* **14**, 901 (1996)

73. S. ALEXANDER, L. HELLEMANS, O. MARTI, J. SCHNEIR, V. ELINGS, P. K. HANSMA, M. LONGMIRE, J. GURLEY: An Atomic-resolution Atomic-force Microscope Implemented using an Optical Lever. *Journal of Applied Physics* **65**, 164 (1989)
74. G. H. SIMON, M. HEYDE, H.-P. RUST: Recipes for Cantilever Parameter Determination in Dynamic Force Spectroscopy: Spring Constant and Amplitude. *Nanotechnology* **18**, 255503 (2007)
75. P. GÜNTHER, U. C. FISCHER, K. DRANSFELD: Scanning Near-field Acoustic Microscopy. *Applied Physics B: Lasers and Optics* **48**, 89 (1989)
76. F. J. GIESSIBL: Atomic Resolution on Si(111)-(7x7) by Noncontact Atomic Force Microscopy with a Force Sensor Based on a Quartz Tuning Fork. *Applied Physics Letters* **76**, 1470 (2000)
77. F. J. GIESSIBL, S. HEMBACHER, M. HERZ, C. SCHILLER, J. MANNHART: Stability Considerations and Implementation of Cantilevers Allowing Dynamic Force Microscopy with Optimal Resolution: The qPlus Sensor. *Nanotechnology* **15**, S79 (2004)
78. F. J. GIESSIBL, M. REICHLING: Investigating Atomic Details of the CaF₂(111) Surface with a qPlus Sensor. *Nanotechnology* **16**, S118 (2005)
79. A. BETTAC, J. KOEBLE, K. WINKLER, B. UDER, M. MAIER, A. FELTZ: QPlus: Atomic Force Microscopy on Single-crystal Insulators with Small Oscillation Amplitudes at 5 K. *Nanotechnology* **20**, 264009 (2009)
80. F. J. GIESSIBL, S. HEMBACHER, H. BIELEFELDT, J. MANNHART: Subatomic Features on the Silicon (111)-(7x7) Surface Observed by Atomic Force Microscopy. *Science* **289**, 422 (2000)

81. E. WUTSCHER, F. J. GIESSIBL: Atomic Force Microscopy at Ambient and Liquid Conditions with Stiff Sensors and Small Amplitudes.
Review of Scientific Instruments **82**, 093703 (2011)
82. M. Y. ALI, W. HUNG, F. YONGQI: A Review of Focused Ion Beam Sputtering.
International Journal of Precision Engineering and Manufacturing **11**, 157 (2010)
83. L. GROSS, F. MOHN, N. MOLL, P. LILJEROTH, G. MEYER: The Chemical Structure of a Molecule Resolved by Atomic Force Microscopy.
Science **325**, 1110 (2009)
84. A. SWEETMAN, S. JARVIS, R. DANZA, J. BAMIDELE, S. GANGOPADHYAY, G. A. SHAW, L. KANTOROVICH, P. MORIARTY: Toggling Bistable Atoms via Mechanical Switching of Bond Angle.
Physical Review Letters **106**, 136101 (2011)
85. A. SWEETMAN, R. DANZA, S. GANGOPADHYAY, P. MORIARTY: Imaging and Manipulation of the Si(100) Surface by Small-amplitude NC-AFM at Zero and Very Low Applied Bias.
Journal of Physics: Condensed Matter **24**, 084009 (2012)
86. L. TRÖGER, J. SCHÜTTE, F. OSTENDORF, A. KÜHNLE, M. REICHLING: Concept for Support and Cleavage of Brittle Crystals.
Review of Scientific Instruments **80**, 063703 (2009)
87. J. WOLLBRANDT, W. LINKE, U. BRÜCKNER: Untersuchung elektrostatischer Aufladungen auf Spaltflächen von Alkalihalogenideinkristallen.
Experimentelle Technik der Physik **23**, 65 (1975)
88. C. BARTH, C. R. HENRY: Kelvin Probe Force Microscopy on Surfaces of UHV Cleaved Ionic Crystals.
Nanotechnology **17**, 155 (2006)

89. M. NIMMRICH: Atomic-scale Characterization of Diamond Surfaces and Fullerene Self-assembly, University of Mainz, PhD thesis, 2012
90. D. NEČAS, P. KLAPETEK: Gwyddion: An Open-source Software for SPM Data Analysis. *Central European Journal of Physics* **10**, 181 (2012)
91. D. W. POHL, R. MÖLLER: Tracking Tunneling Microscopy. *Review of Scientific Instruments* **59**, 840 (1988)
92. B. S. SWARTZENTRUBER: Direct Measurement of Surface Diffusion Using Atom-tracking Scanning Tunneling Microscopy. *Physical Review Letters* **76**, 459 (1996)
93. P. RAHE, J. SCHÜTTE, W. SCHNIEDERBEREND, M. REICHLING, M. ABE, Y. SUGIMOTO, A. KÜHNLE: Flexible Drift-compensation System for Precise 3D Force Mapping in Severe Drift Environments. *Review of Scientific Instruments* **82**, 063704 (2011)
94. P. RAHE, R. BECHSTEIN, A. KÜHNLE: Vertical and Lateral Drift Corrections of Scanning Probe Microscopy Images. *Journal of Vacuum Science and Technology B* **28**, C4E31 (2010)
95. S. SADEWASSER, M. C. LUX-STEINER: Correct Height Measurement in Noncontact Atomic Force Microscopy. *Physical Review Letters* **91**, 266101 (2003)
96. K.-M. YANG, J. Y. CHUNG, M. F. HSIEH, S.-S. FERNG, D.-S. LIN, T.-C. CHIANG: Systematic Variations in Apparent Topographic Height as Measured by Noncontact Atomic Force Microscopy. *Phys. Rev. B* **74**, 193313 (2006)
97. D. ZIEGLER, J. RYCHEN, N. NAUJOKS, A. STEMMER: Compensating Electrostatic Forces by Single-scan Kelvin

- Probe Force Microscopy.
Nanotechnology **18**, 225505 (2007)
98. P. W. MIRWALD: The Electrical Conductivity of Calcite Between 300 and 1200°C at a CO₂ Pressure of 40 bars.
Physics and Chemistry of Minerals **4**, 291 (1979)
99. L. ADDADI, S. WEINER: Control and Design Principles in Biological Mineralization.
Angewandte Chemie International Edition **31**, 153 (1992)
100. H. CÖLFEN: Precipitation of Carbonates: Recent Progress in Controlled Production of Complex Shapes.
Current Opinion in Colloid & Interface Science **8**, 23 (2003)
101. R. SMARTT, W. STEEL: Birefringence of Quartz and Calcite.
Journal of the Optical Society of America **49**, 710 (1959)
102. X. CHEN, Y. LUO, J. ZHANG, K. JIANG, J. B. PENDRY, S. ZHANG: Macroscopic Invisibility Cloaking of Visible Light.
Nature Communications **2**, 176 (2011)
103. M. E. TUCKER, V. P. WRIGHT: Carbonate Sedimentology.
Wiley-Blackwell, 1991
104. L. ADDADI, S. WEINER: Crystals, Asymmetry and Life.
Nature **411**, 753 (2001)
105. C. A. ORME, A. NOY, A. WIERZBICKI, M. T. MCBRIDE, M. GRANTHAM, H. H. TENG, P. M. DOVE, J. J. DEYOREO: Formation of Chiral Morphologies Through Selective Binding of Amino Acids to Calcite Surface Steps.
Nature **411**, 775 (2001)
106. D. R. BAER, D. L. BLANCHARD JR: Studies of the Calcite Cleavage Surface for Comparison with Calculation.
Applied Surface Science **72**, 295 (1993)

107. P. RAHE: The Calcite($10\bar{1}4$) Surface: A Versatile Substrate for Molecular Self-Assembly, University of Mainz, PhD thesis, 2011
108. P. RAHE, K. KITTELMANN, J. L. NEFF, M. NIMMRICH, M. REICHLING, P. MAASS, A. KÜHNLE: Tuning Self-Assembly on Bulk Insulator Surfaces by Anchoring of the Organic Building Blocks.
Physical Chemistry Chemical Physics **accepted** (2013)
109. S. L. STIPP, M. F. HOCELLA: Structure and Bonding Environments at the Calcite Surface as Observed with X-Ray Photoelectron-Spectroscopy (Xps) and Low-Energy Electron-Diffraction (Leed).
Geochimica Et Cosmochimica Acta **55**, 1723 (1991)
110. J. SCHÜTTE, P. RAHE, L. TRÖGER, S. RODE, R. BECHSTEIN, M. REICHLING, A. KÜHNLE: Clear Signature of the (2x1) Reconstruction of Calcite (10-14).
Langmuir **26**, 8295 (2010)
111. S. L. S. STIPP, C. M. EGGLESTON, B. S. NIELSEN: Calcite Surface-Structure Observed at Microtopographic and Molecular Scales with Atomic-Force Microscopy (AFM).
Geochimica Et Cosmochimica Acta **58**, 3023 (1994)
112. M. LAHAV, L. LEISEROWITZ: Comments on "Mirror Symmetry Breaking" of the Centrossymmetric CaCO_3 Crystals with Amino Acids.
Angewandte Chemie International Edition **120**, 3738 (2008)
113. P. RAHE, J. SCHÜTTE, A. KÜHNLE: NC-AFM Contrast Formation on the Calcite ($10\bar{1}4$) Surface.
Journal of Physics: Condensed Matter **24**, 084006 (2012)
114. S. KUHN, P. RAHE, M. KITTELMANN, M. ABE, Y. SUGIMOTO, A. KÜHNLE: Determining the Absolute Orientation of a Low-symmetry Insulating Surface by Microscopic and Macroscopic Means.
in preparation (2013)

115. C. M. HAUKE, R. BECHSTEIN, M. KITTELMANN, C. STORZ, A. F. M. KILBINGER, P. RAHE, A. KÜHNLE: Controlling Molecular Self-Assembly on an Insulating Surface by Rationally Designing an Efficient Anchor Functionality that Maintains Structural Flexibility. *ACS Nano* **submitted** (2013)
116. S. L. KWOLEK, P. W. MORGAN, J. R. SCHAEFGEN, L. W. GULRICH: Synthesis, Anisotropic Solutions, and Fibers of Poly(1,4-benzamide). *Macromolecules* **10**, 1390 (1977)
117. H. SEYLER, A. F. M. KILBINGER: Linear Organo-Soluble Poly(p-benzamide)s. *Macromolecules* **42**, 9141 (2009)
118. C. STORZ, M. SCHULZE, A. F. M. KILBINGER: Solubility and Aggregation Behavior of Dendronized Poly(p-benzamide)s. *Macromolecular Rapid Communications* **32**, 238 (2011)
119. M. SCHULZE, C. STORZ, A. F. M. KILBINGER: Non-aggregating Poly (p-benzamide)s. *CHIMIA International Journal for Chemistry* **66**, 258 (2012)
120. R. ABBEL, H. FREY, D. SCHOLLMAYER, A. F. M. KILBINGER: Soluble Oligoaramide Precursors - A Novel Class of Building Blocks for Rod-coil Architectures. *Chemistry - A European Journal* **11**, 2170 (2005)
121. T. W. SCHLEUSS, R. ABBEL, M. GROSS, D. SCHOLLMAYER, H. FREY, M. MASKOS, R. BERGER, A. F. KILBINGER: Hockey-Puck Micelles from Oligo (p-benzamide)-b-PEG Rod-Coil Block Copolymers. *Angewandte Chemie International Edition* **45**, 2969 (2006)
122. H. M. KÖNIG, A. F. M. KILBINGER: Learning from Nature: β -Sheet-Mimicking Copolymers Get Organized. *Angewandte Chemie International Edition* **46**, 8334 (2007)

123. C. LOPPACHER, R. BENNEWITZ, O. PFEIFFER, M. GUGGISBERG, M. BAMMERLIN, S. SCHÄR, V. BARWICH, A. BARATOFF, E. MEYER: Experimental Aspects of Dissipation Force Microscopy. *Physical Review B* **62**, 13674 (2000)
124. T. STEINER: The Hydrogen Bond in the Solid State. *Angewandte Chemie International Edition* **41**, 48 (2002)
125. L. SALEM: Attractive Forces Between Long Saturated Chains at Short Distances. *The Journal of Chemical Physics* **37**, 2100 (1962)
126. D. J. LAVRICH, S. M. WETTERER, S. L. BERNASEK, G. SCOLES: Physisorption and Chemisorption of Alkanethiols and Alkyl Sulfides on Au(111). *The Journal of Physical Chemistry B* **102**, 3456 (1998)
127. C. M. HAUKE, R. LINDNER, T. GORELIK, U. KOLB, A. KÜHNLE: Self-Assembly of TPA-Derivatives on the Bulk Insulator Calcite(10.4): A Combined NC-AFM and ADT Study. in preparation (2013)
128. C.-P. LI, J. CHEN, M. DU: Mixed-ligand Metallo-supramolecular Complexes with Brⁿ-terephthalic Acid ($n = 1$ or 4) and a Versatile Bent Dipyriddy Tecton: Structural Modulation by Substituent Effect of the Ligand and Metal Ion. *Polyhedron* **29**, 463 (2010)
129. M. EDDAOUDI, H. LI, O. M. YAGHI: Highly Porous and Stable Metal-Organic Frameworks: Structure Design and Sorption Properties. *Journal of the American Chemical Society* **122**, 1391 (2000)
130. M. EDDAOUDI, J. KIM, M. O'KEEFFE, O. M. YAGHI: Cu₂[O-Br-C₆H₃(CO₂)₂]₂(H₂O)₂·(DMF)₈(H₂O)₂: A Framework Deliberately Designed To Have the NbO Structure Type. *Journal of the American Chemical Society* **124**, 376 (2002)

131. P. M. MILADINOVA, T. N. KONSTANTINOVA: Synthesis and Properties of Some New Blue-emitting Triazine Derivatives of 2-aminoterephthalic Acid, Containing a Polymerisable Group and Stabiliser Fragment. *Coloration Technology* **125**, 242 (2009)
132. H. J. SÜSS: Leitfähigkeitsmessungen an organischen Säuren. *Monatshefte für Chemie und verwandte Teile anderer Wissenschaften* **26**, 1331 (1905)
133. R. WEGSCHEIDER: Über den Einfluss der Constitution auf die Affinitätsconstanten organischer Säuren. *Monatshefte für Chemie und verwandte Teile anderer Wissenschaften* **23**, 287 (1902)
134. V. A. RIGO, C. O. METIN, Q. P. NGUYEN, C. R. MIRANDA: Hydrocarbon Adsorption on Carbonate Mineral Surfaces: A First-Principles Study with van der Waals Interactions. *The Journal of Physical Chemistry C* **116**, 24538 (2012)
135. M. BAILEY, C. J. BROWN: Crystal Structure of Terephthalic Acid. *Acta Cryst.* **22**, 387 (1967)
136. S. CLAIR, S. PONS, A. P. SEITSONEN, H. BRUNE, K. KERN, J. V. BARTH: STM Study of Terephthalic Acid Self-Assembly on Au(111): Hydrogen-Bonded Sheets on an Inhomogeneous Substrate. *J. Phys. Chem. B* **108**, 14585 (2004)
137. M. LACKINGER, S. GRIESSL, L. KAMPSCHULTE, F. JAMITZKY, W. M. HECKL: Dynamics of Grain Boundaries in Two-dimensional Hydrogen-bonded Molecular Networks. *Small* **1**, 532 (2005)
138. M. E. CAÑAS VENTURA, F. KLAPPENBERGER, S. CLAIR, S. PONS, K. KERN, H. BRUNE, T. STRUNSKUS, C. WÖLL, R. FASEL, J. V. BARTH: Coexistence of One- and Two-dimensional Supramolecular Assemblies of Terephthalic

- Acid on Pd(111) Due to Self-limiting Deprotonation.
The Journal of Chemical Physics **125**, 184710 (2006)
139. U. KOLB, T. GORELIK, C. KÜBEL, M. T. OTTEN, D. HUBERT: Towards Automated Diffraction Tomography: Part I - Data Acquisition.
Ultramicroscopy **107**, 507 (2007)
140. U. KOLB, T. GORELIK, M. T. OTTEN: Towards Automated Diffraction Tomography. Part II - Cell Parameter Determination.
Ultramicroscopy **108**, 763 (2008)
141. J. RYBÁČEK, G. HUERTA-ANGELES, A. KOLLÁROVIČ, I. G. STARÁ, I. STARÝ, P. RAHE, M. NIMMRICH, A. KÜHNLE: Racemic and Optically Pure Heptahelicene-2-carboxylic Acid: Its Synthesis and Self-Assembly into Nanowire-Like Aggregates.
European Journal of Organic Chemistry (2011)
142. K.-H. ERNST: Supramolecular Surface Chirality.
Topics in Current Chemistry **265**, 209 (2006)
143. L. PASTEUR: Recherches sur les Relations qui Peuvent Exister Entre la Forme Crystalline et la Composition Chimique, et le Sens de la Polarisation Rotatoire.
Annales de Chimie et de Physique **24**, 442 (1848)
144. R. A. SHELDON: Chirotechnology. Marcel Dekker Inc., 1993
145. C. J. ECKHARDT, N. M. PEACHEY, D. R. SWANSON, J. M. TAKACS, M. A. KHAN, X. GONG, J.-H. KIM, J. WANG, A. UPHAUS: Separation of Chiral Phases in Monolayer Crystals of Racemic Amphiphiles.
Nature **362**, 614 (1993)
146. S. DEFEYTER, F. C. DESCHRYVER: Two-dimensional Supramolecular Self-assembly Probed by Scanning Tunneling Microscopy.
Chemical Society Reviews **32**, 139 (2003)

147. R. FASEL, M. PARSCHAU, K.-H. ERNST: Amplification of Chirality in Two-dimensional Enantiomorphous Lattices. *Nature* **439**, 449 (2006)
148. S. ROMER, B. BEHZADI, R. FASEL, K. H. ERNST: Homochiral Conglomerates and Racemic Crystals in Two Dimensions: Tartaric Acid on Cu(110). *Chemistry - A European Journal* **11**, 4149 (2005)
149. A. KÜHNLE, T. R. LINDEROTH, B. HAMMER, F. BESENBACHER: Chiral Recognition in Dimerization of Adsorbed Cysteine Observed by Scanning Tunneling Microscopy. *Nature* **415**, 891 (2002)
150. A. G. MARK, M. FORSTER, R. RAVAL: Recognition and Ordering at Surfaces: The Importance of Handedness and Footedness. *Chemical Physics Physical Chemics* **12**, 1474 (2011)
151. M. YU, N. KALASHNYK, W. XU, R. BARATTIN, Y. BENJALAL, E. LAEGSGAARD, I. STENSGAARD, M. HLIWA, X. BOUJU, A. GOURDON, C. JOACHIM, F. BESENBACHER, T. R. LINDEROTH: Supramolecular Architectures on Surfaces Formed through Hydrogen Bonding Optimized in Three Dimensions. *ACS Nano* **4**, 4097 (2010)
152. P. RAHE, M. NIMMRICH, A. GREULING, J. SCHÜTTE, I. STARÁ, J. RYBÁČEK, G. HUERTA-ANGELES, I. STARÝ, M. ROHLFING, A. KÜHNLE: Toward Molecular Nanowires Self-Assembled on an Insulating Substrate: Heptahelicene-2-carboxylic acid on Calcite (10-14). *Journal of Physical Chemistry C* **114**, 1547 (2010)
153. K.-H. ERNST, M. NEUBER, M. GRUNZE, U. ELLERBECK: NEXAFS Study on the Orientation of Chiral P-Heptahelicene on Ni(100). *Journal of the American Chemical Society* **123**, 493 (2001)

Acknowledgements

Zum Schluss möchte ich allen Personen herzlich danken, die zum Gelingen dieser Arbeit beigetragen haben.

Zunächst gilt mein besonderer Dank

- ... [REDACTED] für die hochmotivierte Betreuung und die Möglichkeit an diesem spannenden Thema zu forschen. Trotz ihres prall gefüllten Terminkalenders hatte sie immer ein offenes Ohr für Fragen und nahm sich stets die Zeit für ausführliche Diskussionen.
- ... [REDACTED] für seine Bereitschaft das Zweitgutachten zu übernehmen und seine interessierten Fragen während der MAINZ Thesis Committee Treffen.
- ... der **Graduiertenschule MAINZ** für die erhaltene Förderung als Kollegiat.
- ... [REDACTED] für seine Mentortätigkeit im Rahmen der Graduiertenschule.

Außerdem danke ich natürlich allen Mitgliedern der **Arbeitsgruppe** [REDACTED]. Die gute Zusammenarbeit und das angenehme Arbeitsklima haben dazu beigetragen, dass es auch in den stressigen Phasen der Arbeit niemals frustrierend wurde. Besonders hervorheben möchte ich dabei

- ... [REDACTED] der mich zu Beginn meiner Arbeit in die Feinheiten der UHV-Technik eingewiesen und mich beim Aufbau des neuen AFMs tatkräftig unterstützt hat.
- ... [REDACTED] und [REDACTED] für die regen Diskus-

sionen und Verbesserungsvorschläge die zwar häufig zu viel zusätzlicher Arbeit führten, aber jedesmal einen Qualitätsgewinn für meine Arbeit bedeuteten.

... [REDACTED] und [REDACTED] die durch ihren unverwechselbaren Humor und die immer passenden Simpsons-Zitate zu einer hochmotivierenden Büroatmosphäre beigetragen haben.

I am very grateful to our collaborators:

... [REDACTED] at the Academy of Sciences of the Czech Republic in Prague, for kindly supplying the helicene molecules.

... [REDACTED] aus der Arbeitsgruppe [REDACTED] an der Uni Fribourg für die Bereitstellung diverser Moleküle und die gute Zusammenarbeit, nicht nur beim Vorbereiten der Publikationen.

... [REDACTED] und [REDACTED] aus der Arbeitsgruppe [REDACTED] für die ADT- und SEM-Messungen.

Ein ganz besonderer Dank gilt

... **meinen Freunden**, insbesondere [REDACTED] [REDACTED] für Gespräche über Gott und die Welt und die gemeinsam verbrachte Zeit abseits der Arbeit.

... der Fechtgruppe [REDACTED] [REDACTED] deren Training stets eine willkommene geistige Herausforderung der anderen Art bedeutet.

Sicherlich der größte Dank gilt jedoch **meiner Familie** und meiner Freundin [REDACTED] die immer für mich da waren und mich in jeder nur erdenklichen Hinsicht unterstützt haben.

"Up and atom!"

Publications and Presentations

Publications in peer-reviewed journals

- **On-surface Covalent Linking of Organic Building Blocks on a Bulk Insulator**
M. Kittelmann, P. Rahe, M. Nimmrich, **C. M. Hauke**, A. Gourdon A. Kühnle
ACS Nano **5**, 8420 (2011)
- **Construction of a Compact ^3He Polarizing Facility**
C. Mrozik, O. Endner, **C. Hauke**, W. Heil, S. Karpuk, J. Klemmer, E. W. Otten
Journal of Physics: Conference Series **294**, 012007 (2011)
- **Molecular Self-Assembly of Enantiopure Heptahelicene-2-Carboxylic Acid on Calcite ($10\bar{1}4$)**
C. M. Hauke, P. Rahe, M. Nimmrich, J. Schütte, M. Kittelmann, I. G. Stará, I. Starý, J. Rybáček, A. Kühnle
Journal of Physical Chemistry C **116**, 4637 (2012)
- **Controlling Molecular Self-Assembly on an Insulating Surface by Rationally Designing an Efficient Anchor Functionality that Maintains Structural Flexibility**
C. M. Hauke, R. Bechstein, M. Kittelmann, C. Storz, A. F. M. Kilbinger, P. Rahe, A. Kühnle
submitted

- **One-pot Synthesis and AFM Imaging of a Triangular Aramide Macrocycle**
C. Storz, **C. M. Hauke**, A. Kühnle, A. F. M. Kilbinger
submitted
- **Self-Assembly of TPA-Derivatives on the Bulk Insulator Calcite (10.4): A Combined NC-AFM and ADT Study**
C. M. Hauke, R. Lindner, T. Gorelik, U. Kolb, A. Kühnle
in preparation

Talks

(presenting author underlined)

- **Entwicklung einer kompakten Anlage für die Polarisation von ^3He durch metastabiles optisches Pumpen**
C. M. Hauke, W. Heil, S. Karpuk, E. W. Otten
(DPG Spring Conference 2009, Hamburg, Germany)
- **Construction of a Compact ^3He Polarizing Facility for Local Usage**
C. Mrozik, O. Endner, **C. M. Hauke**, W. Heil, S. Karpuk, J. Klemmer, E. W. Otten
(DPG Spring Conference 2011, Dresden, Germany)
- **Development of a Magnetically Shielded Compact ^3He Polarizer**
O. Endner, **C. M. Hauke**, W. Heil, S. Karpuk, J. Klemmer, C. Mrozik, E. W. Otten
(DPG Spring Conference 2011, Dresden, Germany)
- **Self-assembly and Chiral Recognition of Heptahe-licene Acid on an Insulating Surface**
C. M. Hauke, P. Rahe, M. Nimmrich, J. Schütte, M. Kitzelmann, I. G. Stará, I. Starý, J. Rybáček, A. Kühnle
(European Conference on Surface Science 2011, Wrocław, Poland)

-
- **On-surface Covalent Linking on an Insulating Substrate**
M. Kittelmann, P. Rahe, M. Nimmrich, **C. M. Hauke**, A. Gourdon, A. Kühnle
(European Conference on Surface Science 2011, Wroclaw, Poland)
 - **Phase Transition of a Molecular Film and On-surface Covalent Linking**
M. Kittelmann, P. Rahe, **C. M. Hauke**, M. Nimmrich, A. Kühnle
(NC-AFM 2011, Lindau, Germany)
 - **On-surface Covalent Linking on an Insulating Substrate**
R. Lindner, M. Kittelmann, P. Rahe, M. Nimmrich, **C. M. Hauke**, A. Gourdon, A. Kühnle
(DPG Spring Conference 2012, Berlin, Germany)
 - **Lichtinduzierte Knüpfung von kovalenten Bindungen auf Isolatoren**
R. Lindner, M. Kittelmann, P. Rahe, **C. M. Hauke**, M. Nimmrich, A. Kühnle
(DPG Spring Conference 2012, Berlin, Germany)
 - **Self-Assembly of Chiral Molecules on an Insulating Surface**
C. M. Hauke, A. Kühnle
(MAINZ Summer Retreat 2012, Cambridge, United Kingdom)
 - **Chiral Wetting Layers of Oligo-Aramides on an Insulating Surface**
C. M. Hauke, P. Rahe, M. Kittelmann, C. Storz, A. F. M. Kilbinger, A. Kühnle
(European Conference on Surface Science 2012, Edinburgh, United Kingdom)

Poster Presentations

- **Chiral Recognition and Homochiral Island Formation on an Insulating Substrate**
C. M. Hauke, P. Rahe, M. Nimmrich, J. Schütte, M. Kittelmann, I. G. Stará, I. Starý, J. Rybáček, A. Kühnle
(Advanced Atomic Force Microscopy Techniques 2011, Karlsruhe, Germany)
- **Insulating Substrates as a Surface for Chiral Recognition and Homochiral Island Formation**
C. M. Hauke, P. Rahe, M. Nimmrich, J. Schütte, M. Kittelmann, I. G. Stará, I. Starý, J. Rybáček, A. Kühnle
(ISPM 2011, Munich, Germany)
- **Influence of Chirality on Molecular Structure Formation: Helicene Molecules on Calcite (10 $\bar{1}$ 4)**
C. M. Hauke, P. Rahe, M. Nimmrich, J. Schütte, M. Kittelmann, I. G. Stará, I. Starý, J. Rybáček, A. Kühnle
(NC-AFM 2011, Lindau, Germany)
- **Photopolymerisation of C60 on an Insulating Substrate**
R. Lindner, M. Kittelmann, P. Rahe, **C. M. Hauke**, M. Nimmrich, A. Kühnle
(BASF Summer School 2012, Ludwigshafen, Germany)

Curriculum vitae (educational)

Christopher Moritz Hauke
born 15.04.1984 in Mainz (Germany)



Academic Education

- 2011 - 2013 Member of the Graduate School of Excellence
Materials Science in Mainz (MAINZ)
- 2010 - 2013 Doctoral studies at the
Johannes Gutenberg Universität Mainz
(Doctoral advisor [REDACTED])
- 2009 Graduation with degree "Diplom Physiker"
- 2007 - 2008 Study of physics at the
Royal Institute of Technology Stockholm
- 2004 - 2009 Study of physics at the
Johannes Gutenberg Universität Mainz

School Education

- 1994 - 2003 Willigis Gymnasium Mainz
- 1990 - 1994 Martinus Grundschule Mainz

